DISSERTATIONES
CHIMICAE
UNIVERSITATIS
TARTUENSIS
237

MIRIAM KOPPEL

The diffusion of H_2 adsorbed in carbide-derived carbons: a quasi-elastic neutron scattering study

DISSERTATIONES CHIMICAE UNIVERSITATIS TARTUENSIS
237

DISSERTATIONES CHIMICAE UNIVERSITATIS TARTUENSIS
237

MIRIAM KOPPEL

The diffusion of H_2 adsorbed in carbide-derived carbons: a quasi-elastic neutron scattering study

UNIVERSITY OF TARTU
Press
1632

Institute of Chemistry, Faculty of Science and Technology, University of Tartu, Estonia

The dissertation is accepted for the commencement of the degree of Doctor of Philosophy in Chemistry on 10th of June, by the Council of Institute of Chemistry, University of Tartu.

Supervisors: Associate Professor Rasmus Palm, Ph.D.
University of Tartu, Estonia

Riinu Härmas, Ph.D.
Destiny Energy Estonia OÜ, Estonia

Professor Enn Lust, Ph.D.
University of Tartu, Estonia

Opponent: Alexander O'Malley, Ph.D.
University of Bath, UK

Commencement: August 26th, 2025 at 10.15, Ravila 14A-1020, Tartu (Chemicum)

This work has been partially supported by ASTRA project PER ASPERA Graduate School of Functional Materials and Technologies receiving funding from the European Regional Development Fund under project in University of Tartu, Estonia.

ISSN 1406-0299 (print)
ISBN 978-9916-27-923-6 (print)
ISSN 2806-2159 (pdf)
ISBN 978-9916-27-924-3 (pdf)

University of Tartu Press
www.tyk.ee

CONTENTS

1. LIST OF ORIGINAL PUBLICATIONS

I. **M. Koppel**, R. Palm, R. Härmas, M. Russina, V. Grzimek, J. Jagiello, M. Paalo, H. Kurig, M. Månsson, O. Oll, E. Lust, Pore wall corrugation effect on the dynamics of adsorbed H_2 studied by *in situ* quasi-elastic neutron scattering: Observation of two timescaled diffusion, Carbon. 2022, 197, 359–367.

II. **M. Koppel**, R. Palm, R. Härmas, M. T. F. Telling, M. D. Le, T. Guidi, K. Tuul, M. Paalo, E. Lust, Restricted dynamics and para-ortho conversion of H_2 adsorbed in micro- and mesoporous carbide-derived carbon: a quasi- and inelastic neutron scattering study, Journal of Physical Chemistry C. 2025, 129, 4789−4799.

III. **M. Koppel**, R. Palm, R. Härmas, M. T. F. Telling, M. D. Le, T. Guidi, K. Tuul, M. Paalo, L. Kalder, J. Jagiello, T. Romann, J. Aruväli, M. Månsson, E. Lust, Disentangling the self-diffusional dynamics of H_2 adsorbed in micro- and mesoporous carbide-derived carbon by wide temporal range quasi-elastic neutron scattering, Carbon. 2024, 219, 118799.

IV. **M. Koppel**, R. Palm, R. Härmas, M. Russina, N. Matsubara, M. Månsson, V. Grzimek, M. Paalo, J. Aruväli, T. Romann, O. Oll, E. Lust (2021). In Situ Observation of Pressure Modulated Reversible Structural Changes in the Graphitic Domains of Carbide-Derived Carbons. Carbon. 174, 190−200.

Author's contribution:

Paper I: Measured gas adsorption data, participated in the quasi-elastic neutron scattering measurement of two samples out of three, analysed the data of all three of the quasi-elastic neutron scattering measurements, and prepared the manuscript.

Paper II: Measured gas adsorption data, prepared the proposals for the two neutron scattering measurements, participated in the two neutron scattering measurements, analysed the data of the neutron scattering measurements, and prepared the manuscript.

Paper III: Measured gas adsorption data, prepared the proposals for the two neutron scattering measurements, participated in the neutron scattering measurements (same measurements as for paper II), analysed the quasi-elastic neutron scattering data, and prepared the manuscript.

Paper IV: Measured the H_2 adsorption data, participated in the quasi-elastic neutron scattering measurement of the two samples (same measurements as for paper I), analysed the data of all three neutron scattering measurements, and participated in the preparation of the manuscript.

2. ACRONYMS AND SYMBOLS

$\langle N \rangle$ – average number of graphenic layers in a single stack

2D-NLDFT-HS – Two-Dimensional Non-Local Density Functional Theory for Heterogeneous Surfaces

$A_{0,2site}(Q)$ – model function for rotational jumps between two sites with distance d

$A_{0,sph}(Q)$ – model function for continuous rotational diffusion on the surface of a sphere with a diameter d

$A_{0,vol}(Q)$ – model function for continuous rotational diffusion within the volume of a sphere with a diameter d

a_3 – average interlayer spacing

CDC – Carbide-Derived Carbon

D – diffusion coefficient

D_0 – diffusion coefficient at infinite temperature

$\delta(E)$ – Dirac delta function

DFT – Density Functional Theory

E – energy transfer

E_a – activation energy

EISF or A_0 – Elastic Incoherent Structure Factor

FWHM – Full Width of a peak at Half Maximum

$\Gamma_{HR}(Q)$ – model function for half width at half maximum of the quasi-elastic component of the signal at a given Q value, HR denotes the Hall-Ross model

$\Gamma_{SS}(Q)$ – model function for half width at half maximum of the quasi-elastic component of the signal at a given Q value, SS denotes the Singwi-Sjölander model

HWHM or Γ – Half Width of a peak at Half Maximum

IUPAC – International Union of Pure and Applied Chemistry

j_0 – zero-order spherical Bessel function of the first kind

j_1 – first-order spherical Bessel function of the first kind

$L(Q,E)$ – Lorentzian function

L_a – average graphenic layer extent

L_c – average stack size of graphenic layers

n_{H2} – amount of adsorbed H_2 per mass of adsorbent

NLDFT – Non-Local Density Functional Theory

p – absolute pressure

p/p_0 – relative pressure

p_0 – saturation pressure

$p_{H2,load}$ – H_2 loading pressure

Q – scattering vector magnitude

QENS – Quasi-Elastic Neutron Scattering

R – universal gas constant (8.314 J mol^{-1} K^{-1})

$R(Q,E)$ – resolution function

SAIEUS – stable numerical Solution of the Adsorption Integral Equation Using Splines

$S(Q,E)$ – dynamic structure factor

$S_{H2}(Q,E)$ – incoherent dynamic structure factor of H_2

$S_{fun}(Q,E)$ – functional form of the dynamic structure factor

S_{DFT} – surface area calculated by applying the 2D-NLDFT model on the gas adsorption data

STP – Standard Temperature and Pressure (0 °C and 1 bar)

T – temperature

V_{DFT} – pore volume calculated by applying the 2D-NLDFT model on the gas adsorption data

V_{meso} – mesopore volume

V_{smp} – supermicropore volume

V_{ump} – ultramicropore volume

w – pore width

WAXS – Wide-Angle X-ray Scattering

XRD – X-Ray Diffraction

3. INTRODUCTION

The diffusion* of H_2 is of great interest for many applications, such as H_2 storage via physical adsorption, H_2 and D_2 (deuterium) separation, and heterogeneous catalysis [1–7]. In all these applications, the diffusion of adsorbed H_2 takes place, and different applications have different requirements for the porous adsorbent materials. For H_2 storage, pores with widths (w) 6–7 Å are important as these pores enable to store 30% more H_2 at 100 bar and at 77 K compared to a cryo-compression system without the adsorbent at similar experimental conditions [8]. For H_2:D_2 separation, pores with w from 3–7 Å are required because in such narrow pores, quantum effects influence diffusion and adsorption of H_2 and D_2 at cryogenic temperatures, enabling selective isotope separation [5–7]. Pores with $w \leq 20$ Å (micropores) are important in catalyst support materials for polymer electrolyte fuel cells and electrolysers since they provide active sites and pores with w 20–500 Å (mesopores) and > 500 Å (macropores) ensure fast mass transport of H_2 (and O_2) [9,10]. To develop better materials for these applications, it is important to understand the diffusion of H_2 adsorbed in carbon materials with varying structures.

Quasi-elastic neutron scattering is an advantageous method to study the diffusion of H_2 [6,7,11–18]. H_2 has a large incoherent neutron scattering cross-section and therefore, neutrons are sensitive towards H_2. The energy of neutrons used in the scattering experiments (0.2–330 meV) is suitable for studying diffusion kinetics. Neutrons have a large penetration depth in most materials, enabling the use of complex sample environments such as sample cells tolerant to low temperatures and high pressures and also for conducting *in situ* measurements [19–21].

Carbide-derived carbons (CDCs) are well-suited adsorbents to study the diffusion of H_2 with neutrons because the synthesized carbon materials are relatively free of additives [22]. The structure of a CDC can be controlled by the choice of precursor carbide and synthesis conditions [23]. For example, the porous structure of the CDC can vary from very microporous to mainly meso- and macroporous and the graphenic structure can range from disordered (graphene-like layers randomly ordered) to ordered (graphite-like) [22,24]. CDCs have been used in different applications such as electrode materials in supercapacitors, batteries, catalyst supports in polymer electrolyte membrane fuel cells, and as adsorbents for H_2 and other gas adsorption applications [3,22,25,26]. CDCs' tunable structure makes them good model materials for studying the H_2 diffusion processes.

To improve materials for various applications requiring different porous and graphenic structures, it is crucial to understand the diffusion properties of H_2 adsorbed in carbon materials with these varying structures. Therefore, this thesis aims to

* For consistency, the terms „diffusion“ and „self-diffusion“ are used for all mass transport phenomena throughout this thesis.

- determine the porous and graphenic structure of model CDC materials using well-established and comprehensive physical characterization methods such as multiple gas adsorption and wide-angle X-ray scattering,
- determine the diffusion mechanisms of H_2 adsorbed in CDCs using quasi-elastic neutron scattering at various H_2 loading and temperature conditions,
- investigate the influence of the porous and graphenic structure of CDCs on the diffusive properties of adsorbed H_2.

4. LITERATURE OVERVIEW

4.1. Carbide-derived carbons

Carbide-derived carbons (CDCs) are a group of carbon materials produced by selectively removing metal or metalloid atoms from carbide precursors such as binary carbides (e.g., SiC, TiC) or ternary carbides (e.g., Mo_2AlC, V_2AlC) [27]. The CDC materials have a diverse graphenic and porous structure (Figure 1a) [22].

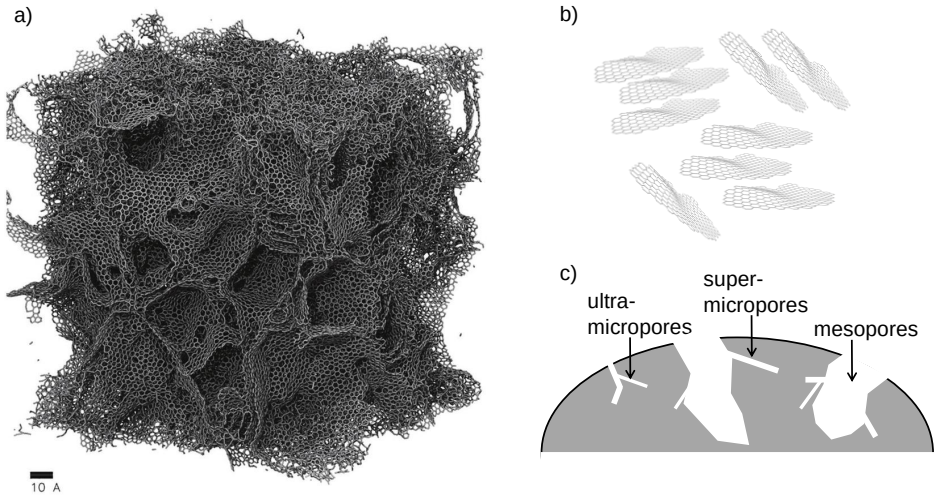

Figure 1. a) Model of a CDC generated with quenched molecular dynamics with a ReaxFF force field [28] (available under a CC-BY 4.0 license. Copyright 2017 Cheng Zhan. Published by WILEY-VCH Verlag GmbH & Co. KGaA, Weinheim); a simplified visualisation of the b) graphenic structure and c) porous structure with ultramicropores (pore width $w < 7$ Å), supermicropores (7 Å $< w <$ 20 Å) and mesopores (20 Å $< w <$ 500 Å) of a material.

The graphene-like layers of a CDC material can be corrugated, i.e., can have concaves and convexes, and exhibit varying extents and levels of stacking of the graphene-like layers/domains (Figure 1a,b) [29]. These graphene-like layers resemble sheet- or flake-like structures and they can have defects in them. Therefore, the CDCs can exhibit a very diverse level of orderliness – they can form relatively well-ordered stacks of graphenic layers in the short range, but these relatively well-ordered stacks might not be ordered with respect to each other and therefore, the structure can be relatively disordered in the long range (Figure 1b) [30,31]. The graphenic structure of a CDC depends on the synthesis temperature. When the synthesis temperature of the CDC is increased, the level of graphitization in the CDC also increases [22,24,32,33]. Between these stacks of graphene-like layers with varying orderliness as well as concaves, convexes and defects in the graphene-like layers, porosity can form [30].

The porous structure of a CDC (and a porous carbon more generally) can also vary and is described with the specific surface area and pore size distribution, which shows the pore volume by pore width (w). The International Union of Pure and Applied Chemistry (IUPAC) classifies pores in porous materials based on w into three main categories – micropores (ultra- and supermicropores), mesopores (Figure 1c), and macropores [34]. Micropores are pores with $w < 20$ Å. These pores are further subdivided into ultramicropores ($w < 7$ Å) and supermicropores (7 Å $< w <$ 20 Å). Mesopores are pores with w between 20 Å and 500 Å and macropores are pores with $w > 500$ Å [34]. The porous structure of the CDC materials derived even from the same precursor carbide can be very diverse and depend on the synthesis conditions. For example, CDC synthesized from Mo_2C at 700 °C is highly microporous, whereas CDC synthesized from Mo_2C at 1200 °C is mainly mesoporous [24].

Due to the versatile graphenic and porous structure of CDCs, they have been used in applications that have different requirements for the structure of carbon materials [4,35–38]. For example, for H_2 storage, ultramicropores are the most effective as they are able to confine adsorbed H_2 the strongest and form a high-density H_2 phase [13,39–43]. For catalyst support materials, a combination of micro-, meso-, and macropores are needed. Namely, micropores are needed for the active sites, meso- and macropores are needed to ensure that the diffusion of reactants and products proceeds at a sufficient rate [9,10]. The structure of CDCs is influenced by the chemical composition and structure of the precursor carbide as well as by the synthesis conditions, such as temperature [22,24,29,31,33,44–46].

4.1.1. Synthesis of CDCs

Carbide-derived carbons (CDCs) are synthesized from inorganic precursor carbides [22]. The precursor carbide (e.g., Mo_2C, TiC, SiC) can be purchased or synthesized in-house with, for example, the sol-gel method [24,44,45,47,48].

The sol-gel process is a versatile method that can be used to synthesize compounds such as nitrides, carbides, and fluorides. During the sol-gel process, a colloidal suspension (sol) is generated and is thereafter converted to a viscous gel. This method allows for better control over the particle size and particle size distribution, often resulting in a more uniform and fine-grained structure compared to commercial methods used traditionally for the synthesis of solid materials. Using specific thermal treatment steps, the gel can be converted to different materials such as powders, fibers, and xerogels [49,50].

The CDCs can be synthesized from carbides by halogenation. This can be done by reacting the precursor carbide with chlorine gas at temperatures typically above 200 °C. The synthesis temperature higher than 200 °C is important to ensure that the metal chlorides are removed and to shift the reaction equilibrium towards the CDC formation [22]. For reacting Mo_2C and TiC with Cl_2, the chemical reactions 1 or 2 are followed.

$$Mo_2C\,(s) + 5Cl_2\,(g) \rightarrow C\,(s) + 2MoCl_5\,(g) \quad (1)$$

$$TiC\ (s) + 2Cl_2\ (g) \rightarrow C\ (s) + TiCl_4\ (g) \quad (2)$$

The volatile product can be removed in the excess gas flow. The residual chlorine, chlorides, oxygen-containing functional groups etc. from the surface of the CDCs are typically reduced in H_2 gas flow applied at high temperatures, for example, at 900 °C.

4.1.2. Characterisation of carbons with gas adsorption method

Gas adsorption method is widely used to characterize porous materials. Most commonly, this method is used to estimate the specific surface area, pore volume and pore size distributions of micro- and mesoporous materials. During the measurement of a gas adsorption isotherm, the excess adsorption is measured in relation to the equilibrium pressure of the adsorbate (gas) at a constant temperature. At pressures lower than 1 bar, the total and excess adsorbed amounts can be considered equal [34].

The way the pressure is expressed depends on the temperature at which the adsorption is measured. At an adsorption temperature below the critical point, equilibrium pressure is usually expressed as relative pressure p/p_0, where p is the equilibrium pressure and p_0 is the saturation pressure at the adsorption temperature (e.g., N_2, Ar, and CO_2). At an adsorption temperature above the critical point, where there is no condensation and no p_0 exists, the equilibrium pressure p is used (e.g., for H_2) [34].

Table 1. Gas adsorption analysis conditions for N_2, Ar, CO_2 and H_2.

Adsorbate	N_2	Ar	CO_2	H_2
T / K	77	87	273	77
p_0 / mbar	1019	1003	34853	–*
p/p_0 / unitless	$\sim 10^{-7}$	$\sim 10^{-6}$	$\sim 10^{-4}$	10^{-2} mbar*
D at STP / $cm^2\ s^{-1}$	0.172	0.158	0.09	1.24

T – measurement temperature, p_0 – saturation pressure, p/p_0 – relative pressure from which adsorption is measured, D – diffusion coefficient, * – 77 K is above the critical temperature of H_2 (33 K) and therefore, no p_0 exists and p/p_0 cannot be calculated. Instead of p/p_0, the equilibrium pressure (in mbar) from which H_2 adsorption is measured is shown.

Gas adsorption measurements using gases such as N_2, Ar, CO_2, and H_2 provide different information about the adsorbent because the isotherms obtained with these gases are measured at different analysis conditions (Table 1) [34,51]. The pore width ranges that can be characterized by N_2, Ar, CO_2, and H_2 at the conditions written in Table 1 are visualised in Figure 2.

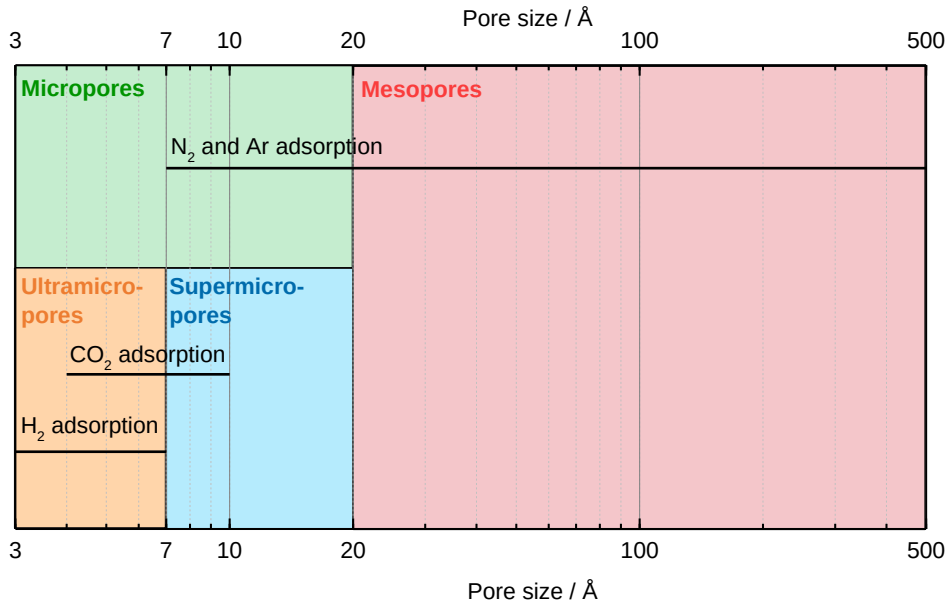

Figure 2. Pore size ranges characterized by N_2, Ar, CO_2, and H_2 adsorption (reproduced from Ref [52]).

N_2 and Ar adsorption isotherms characterize both the micro- and mesopore volumes and surface areas of the material, as the maximum p/p_0 value in these isotherms approaches one (Table 1, Figure 2). At this point in the experiment, the adsorbate is liquefied, filling all the pores with adsorbate. N_2 and Ar adsorption in micropores starts at low p/p_0 values, as these isotherms are measured at low temperatures (at the liquefaction temperatures of N_2 and Ar at 1 bar, respectively). However, at these conditions, the diffusion rate of N_2 and Ar into narrow ultramicropores is slow, which can lead to time-consuming measurements or data points that do not reflect a true adsorption equilibrium [34,53].

CO_2 is more suitable for analyzing the adsorption isotherms of predominantly microporous materials because it is less time-consuming and yields more reliable data at low relative pressure values (Figure 2). This is due to the fact that CO_2 adsorption reaches equilibrium more quickly, as it is measured at a higher temperature (273 K) and begins at a higher pressure compared to N_2 or Ar adsorption (Table 1). In addition to analysis with CO_2, analysis with H_2 is also suitable for the characterization of micropores. Moreover, ultramicropores, and even pores "closed" for other gases can be investigated with H_2 adsorption (Figure 2). That is because H_2 has a higher self-diffusion coefficient than other gases and can access pores that are inaccessible to other gases [34,51,54]. H_2 adsorption is explained in more detail in section 4.2.

N_2 and CO_2 are diatomic and triatomic molecules, respectively, with a quadrupole moment, meaning that the orientation of these molecules can depend on the surface chemistry of the adsorbent. Ar, on the other hand, does not exhibit a

quadrupole moment and, thus, may provide more accurate results when there are specific functional groups on the surface of the adsorbent. When adsorption isotherms measured with N_2 and Ar are equivalent, then the surface of the adsorbent can be considered chemically inert against the gases used for analysis [34,51].

There are different methods to analyse the adsorption isotherms of microporous adsorbents. Traditionally, gas adsorption isotherms are analysed with macroscopic methods and procedures based on, for example, Dubinin's pore-volume-filling theory and Brunauer-Emmett-Teller theory [55,56]. However, these methods have their specific limitations. For example, micropore size and shape of adsorbate molecular packing are not considered. Nevertheless, this approach is still useful for routine work and overall comparison of materials [34]. Nowadays, methods based on statistical mechanics, for example, molecular simulation or density functional theory (DFT) are more common [57,58].

DFT and molecular simulation, which can describe the configuration of the adsorbed phase at the molecular level, are considered to provide a more reliable approach to pore size analysis over the complete nanopore range. DFT-based computational methods provide a reasonably reliable assessment of the pore size distribution for both meso- and micropores, considering that the nanopore structure of the adsorbent is compatible with the chosen DFT kernel. A kernel is a collection of ideal adsorption isotherms used to fit experimental adsorption data [34,57,58].

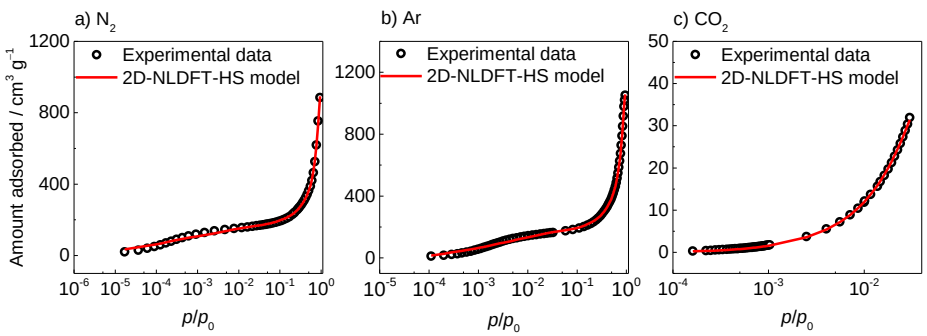

Figure 3. Example a) N_2, b) Ar, and c) CO_2 adsorption isotherms of a micro-mesoporous carbon material (carbon derived from Mo_2C-CDC at 1000 °C) fitted simultaneously with 2D-NLDFT-HS model in SAIEUS software (data is fitted for this thesis).

Traditional DFT methods often use a local density approximation, which assumes that the specific free energy at a point depends only on the local density at that point, neglecting the strong density gradients near the pore walls. Non-local DFT (NLDFT) evaluates the excess Helmholtz free energy using a non-local density approximation, which accounts for strong oscillations in the density profile near the pore walls [58,59]. The drawback of the conventional NLDFT model is that a smooth and homogenous carbon surface is assumed. It has been shown that porous carbon materials, such as CDCs, can have surface heterogeneity and pore wall corrugation [29]. This drawback in NLDFT models has been addressed by the introduction of two-dimensional DFT approaches (2D-NLDFT) [34]. 2D-NLDFT models include both energetic and geometric heterogeneities by adding periodic functions into the pore wall potential and the model accounts for variations in pore wall thickness, edge effects, etc [60,61]. 2D-NLDFT methods are included in commercial software such as SAIEUS (Figure 3) [62]. SAIEUS software has the capability to simultaneously apply the 2D-NLDFT for heterogeneous surface (2D-NLDFT-HS) model to multiple adsorption isotherms measured with different gases, such as N_2 (Figure 3a), Ar (Figure 3b), and CO_2 (Figure 3c), to calculate the pore size distribution.

4.1.3. Characterisation of carbons with wide-angle X-ray scattering method

X-ray diffraction (XRD) is a common experimental technique for investigating the atomic structure of crystalline solids. XRD is based on the interference of X-ray waves elastically scattered from a series of atoms oriented along a particular direction in a crystal. The maxima in the XRD pattern are the result of constructive interference between the scattered X-ray waves, which at the diffraction angle is given by the Bragg's law (Equation 3) [63].

$$n\lambda = 2d\,\sin\theta \tag{3}$$

Here, n is an integer, λ is the incident X-ray wavelength, d is the distance between lattice planes and θ is the diffraction angle. Onward, instead of θ, scattering angle Q calculated as $Q = 4\,\pi\,\sin\theta\,/\,\lambda$ is presented.

As said before, XRD refers to the constructive interference of scattered X-rays from crystalline domains. However, when the investigated materials do not have any long-range order or crystalline domains, such as CDCs, wide-angle X-ray scattering (WAXS) is a more appropriate term to be used for this method.

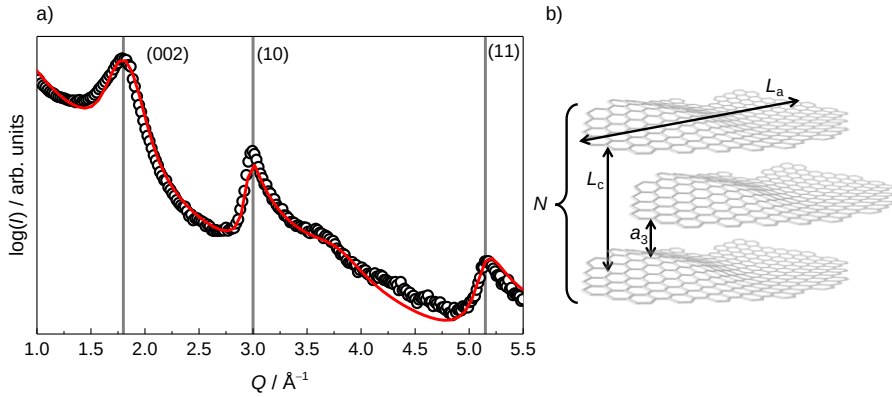

Figure 4. a) Example of a WAXS pattern of non-graphitic carbon material (carbon derived from Mo_2C-CDC at 1000 °C) fitted with an algorithm derived by Ruland and Smarsly (published in Ref [31]). The gray vertical lines denote the positions of reflections that typically appear in the WAXS pattern of a non-graphitic carbon. b) Visualisation of some of the parameters, such as L_a, L_c, $\langle N \rangle$ and a_3 that are possible to be calculated with the CarbX software [64,65].

A typical WAXS curve of non-graphitic carbon contains broad and partially overlapping reflections corresponding to the (00*l*) and (*hk*) planes (Figure 4a). The absence of reflections from (*hkl*) indicates that the carbon lacks long-range 3D order that is characteristic of graphite. The (00*l*) reflection in non-graphitic carbon describes the stacking of graphenic layers, where the parallel stacked layers may be randomly rotated relative to each other, known as turbostratic stacking. The (*hk*) reflection describes the in-plane order within a single graphenic layer [65].

To characterize the WAXS pattern, Ruland and Smarsly have derived an algorithm that can fit the whole scattering pattern of carbonaceous materials and made it available through the CarbX software (Figure 4a) [64,66]. The possibility to fit the whole scattering pattern is a particularly useful feature since it allows for a more comprehensive analysis of the interference maxima, considering that their broadening can result not only from the limited size of graphene domains but also from various other factors such as surface defects, curvature, and strain in the carbon structure [67]. It is important to note that the algorithm assumes the carbon material is homogeneous and that the graphene layers are flat [64,66]. However, it is known that disordered carbons primarily consist of curved graphene layers [22,30,65].

By applying the algorithm, in theory, up to 18 parameters can be obtained. Some of the most useful ones for carbon materials, such as the average graphene layer extent (L_a), the average stacking size (L_c), the average interlayer spacing (a_3), and the average number of layers in a stack ($\langle N \rangle$) are visualised in Figure 4b. The algorithm by Ruland and Smarsly calculates the L_c and a_3 parameters from the shape of the (002) reflection and the L_a parameter from the shape of the (10) reflection. $\langle N \rangle$ is calculated as $\langle N \rangle = \frac{L_c}{a_3(1+\kappa_c)}$, where κ_c is the polydispersity of the stack height [65].

4.2. H_2 adsorption in different pores

During H_2 physical adsorption, H_2 molecule adsorbs on the surface of the material via weak van der Waals forces. The combination of short-range repulsive forces from overlapping electron clouds and long-range attractive forces between the H_2 molecule and the carbon atom results in a characteristic shape of the interaction potential. The interaction potential between H_2 and carbon can be described with the Lennard-Jones potential, which depends on ε (the potential energy minimum) and σ (the distance where the potential between the H_2 molecule and the carbon atom is zero) (Figure 5a). At the potential energy minimum, the sum of attractive and repulsive forces (the negative derivative of the potential) is zero, meaning the H_2 is at an equilibrium distance from the carbon where adsorption is energetically most favorable (Figure 5a) [68].

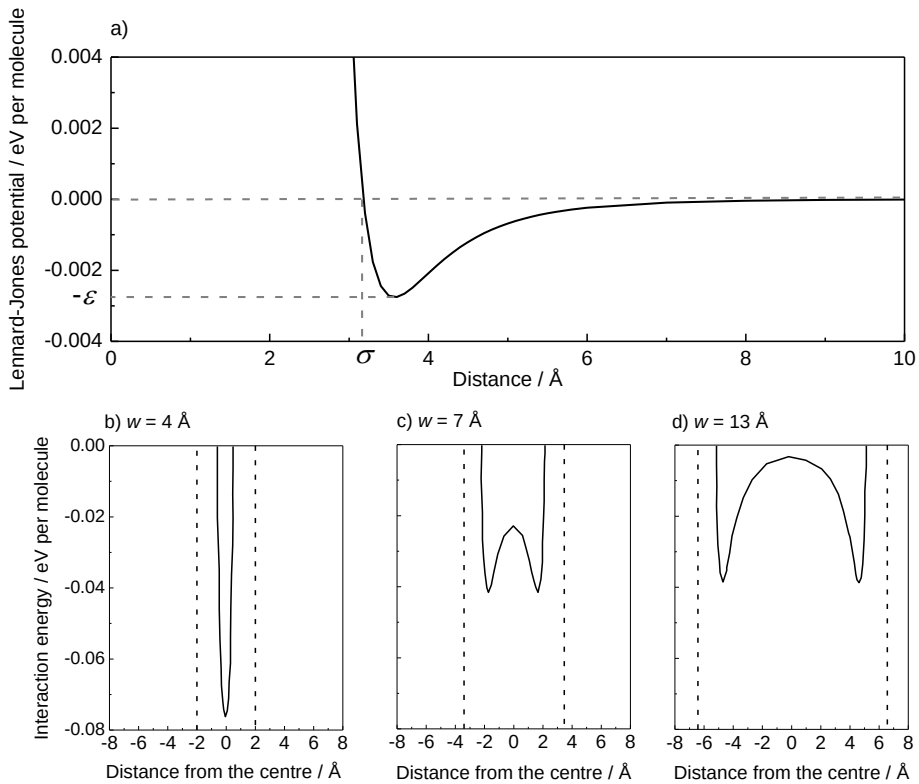

Figure 5. a) Potential energy curve (represented by Lennard-Jones potential) for H_2 molecule and carbon atom interaction as a function of distance, where ε is the potential energy minimum ($-\varepsilon = 0.00276$ eV per molecule) and σ is the distance at which the potential between the H_2 and carbon is zero ($\sigma = 3.18$ Å) (reproduced from Refs.[69,70]). Interaction energy of H_2 inside carbon slit pores with w of b) 4 Å, c) 7 Å, and d) 13 Å plotted against the distance from the centre of the pore (reproduced from Ref [40]), where dashed vertical lines represent the pore walls (physical width).

When H_2 molecule adsorbs in micropores, the interaction energy is the sum of potentials from all nearby carbon atoms forming the pore walls (not just a single atom as in Figure 5a) and H_2 molecule, resulting in a more complex interaction energy curve compared to the H_2 molecule and carbon atom interaction (Figure 5). The interaction energy between the H_2 molecule and the pore wall of a porous carbon material depends on the pore *w* (and shape) (Figure 5b–d). The lowest accessible pore *w* is defined by the kinetic diameter of the H_2 molecule (2.9 Å). That is because the repulsion between the pore surface and the H_2 molecule starts to impede entry of the H_2 molecule for pores just slightly larger than the H_2 molecule (e.g., *w* ~3 Å) [71]. In pores with *w* < ~4 Å, the repulsive contributions of the opposite walls still interfere, leading to reduced attraction between the H_2 molecule and the pore surface [40].

In pores with *w* from ~4 Å to ~6 Å, the H_2 molecule and carbon material interactions are very strong due to the overlapping potentials of opposing pore walls and a single and relatively deep energy minimum located at the center of the pore forms (Figure 5b) [40,72,73]. In pores with *w* of 7 Å, the opposing pore walls still strongly influence the H_2 molecules, but two shallow minima in the interaction energy curve form and the energy minima are not so deep anymore (Figure 5c). As the pore *w* increases to 20 Å, the Lennard-Jones interactions between H_2 and the opposite pore walls decrease, and the opposing pore walls can be regarded as two independent surfaces for the H_2 molecule and the interactions at the center of the pore become negligible (Figure 5d) [40,72,73]. In such pores, multiple H_2 layers can form [73,74]. H_2 adsorption and diffusion in such pores have been thoroughly studied for high-density H_2 storage and effective H_2:D_2 isotope separation [7,40,71–75].

In addition to the average pore *w*, the effect of pore shape on the H_2 diffusion has been studied. It has been shown that pores with a *w* of 7 Å lead to significant H_2 densification compared to bulk H_2 under the same conditions, with only subtle differences in H_2 density due to geometric constraints [76]. Thus, it was concluded that while pore geometry may play some part in influencing the diffusion and density of H_2, pore *w* remains the critical factor. On the other hand, another study found that the spherically shaped pores are better at confining H_2 than slit-shaped pores when the pore *w* is comparable [77]. Nevertheless, it has been shown with experimental and computational methods to a large extent that in pores with *w* of 6–7 Å, H_2 self-diffusion is very restricted and the highest H_2 storage density can be achieved that are required for H_2 storage and H_2:D_2 separation materials [13,39–43].

In even larger pores, i.e., mesopores, additional H_2 layers on top of the H_2 monolayer can be present inside the pore when the amount of H_2 is high enough [74,75]. These additional layers are not in direct contact with the pore wall and can have markedly different densities and self-diffusive properties compared to the H_2 in the monolayer [78,79]. Mesopores (and also macropores) are important in catalyst support materials for polymer electrolyte fuel cells and electrolysers since they ensure fast mass transport of H_2 (and O_2) from the surface layer to the active sites [9,10].

4.3. Neutron scattering method

4.3.1. Neutron properties and scattering process

Neutron has a mass of m = $1.675 \cdot 10^{-27}$ kg, a magnetic dipole moment of $\mu_n = -9.662 \cdot 10^{-27}$ J·T^{-1} and the total charge is zero. A neutron as a free particle has a lifetime of ~15 min. After that, it decays into a proton, an electron and an anti-neutrino (β-decay) [80].

Neutrons interact with atomic nuclei via the short-range strong force or with the magnetic moments of unpaired electrons via spin. The penetration depth of neutrons in most materials is relatively long, typically in the order of a couple of cm, making it possible to study the microscopic properties of bulk samples and use complex sample environments without significant neutron flux attenuation [80]. Also, neutron scattering methods are non-destructive (neutrons with a wavelength of 1.5 Å have an energy of 0.036 eV, whereas X-ray with a wavelength of 1.5 Å has an energy of 8.265 keV), meaning archeological and biological samples can be studied using neutrons [19]. Neutron scattering cross-sections do not depend directly on the number of electrons per atom (as opposed to X-rays). Thus, atoms with few electrons (e.g., H, Li, C, and O) can be studied and even isotopes (e.g., H and D) can be distinguished [19,80,81].

The wavelength of neutrons used in neutron scattering experiments is from 0.5 Å to 20 Å, which is comparable to atomic sizes and inter-distance spacings of atoms in materials. The energy of neutrons used in neutron scattering experiments is from 0.2 meV to 330 meV, which is comparable to the normal energy modes in materials. Therefore, with neutron scattering, the structural properties of materials at the atomic to nanometer scale and dynamics, such as diffusion, lattice vibration, and phonon characteristics can be studied [19,81,82].

A neutron is characterised by its wave vector $\boldsymbol{k}$. When a neutron scatters from a nucleus, it can transfer its energy and momentum to the particle in the sample. The change in the energy and momentum of the neutron is expressed with Equations 4 and 5, respectively.

$$E = E_\mathrm{i} - E_\mathrm{f} = \frac{\hbar}{2m}\left(k_\mathrm{i}^2 - k_\mathrm{f}^2\right) \tag{4}$$

$$\boldsymbol{Q} = \boldsymbol{k}_\mathbf{f} - \boldsymbol{k}_\mathbf{i} \tag{5}$$

Here, E is energy transfer of the neutron, E_i and E_f are the energies of incident and final neutron, respectively, $\hbar$ is angular Planck constant, m is the mass of the neutron, $\boldsymbol{Q}$ is momentum transfer vector (scattering vector), and $\boldsymbol{k}_\mathbf{i}$ and $\boldsymbol{k}_\mathbf{f}$ are the wave vectors of the incident and final neutron, respectively, and their magnitudes are $|\boldsymbol{k}_{\mathbf{i,f}}| = k_{\mathrm{i,f}} = 2\,\pi / \lambda$.

The quantity measured during a neutron scattering experiment is the number of neutrons detected in a solid angle $\delta\Omega$ with energy transfer δE. This quantity is called the double differential scattering cross-section (Equation 6).

$$\frac{\delta^2\sigma}{\delta E \delta\Omega} \propto \frac{k_\mathrm{f}}{k_\mathrm{i}}\left[b_\mathrm{coh}^2 S_\mathrm{coh}(Q,E) + b_\mathrm{inc}^2 S_\mathrm{inc}(Q,E)\right] \quad (6)$$

Here, σ is the scattering cross-section, S is the dynamic structure factor and b is the scattering length (coh and inc denote coherent and incoherent contribution, respectively). Onward, Q is the magnitude of the scattering vector (Q-vector).

Scattering of a neutron from a particle can be coherent or incoherent. In the case of coherent neutron scattering, the neutron wave interacts with the whole sample as a unit and the scattered waves from different nuclei interfere with each other. This type of scattering depends on the relative distances between the constituent atoms and, thus, gives information about the structure of the material [81]. In the case of incoherent neutron scattering, a neutron wave interacts independently with each nucleus in the sample so that the scattered waves from different nuclei do not interfere. This type of scattering can be due to the interaction of a neutron wave with the same atom but at different positions and times. Thus, dynamics associated with incoherent scattering are related to uncorrelated self-motion, such as diffusion [19,81].

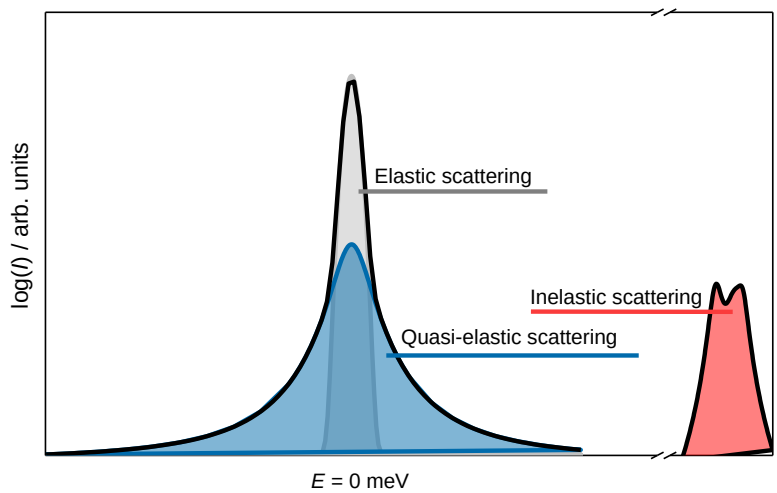

Figure 6. The energy range of elastic ($E \approx 0$ meV), quasi-elastic (-2 meV $\leq E \leq 2$ meV) and inelastic neutron scattering ($E > 2$ meV or $E < -2$ meV).

If the incident neutron scatters from a particle that is effectively immobile (at least in the investigated experimental timescale), the scattering process is elastic and $E_\mathrm{f} = E_\mathrm{i}$ (Figure 6). When the particle from which the incident neutron scatters is moving in a similar timescale to the experimental timescale, the change in the energy of the neutron is small (-2 meV $\leq E \leq 2$ meV), and the peak maximum is at $E \approx 0$, then the neutron scattering process is quasi-elastic [19,81]. Quasi-elastic neutron scattering can be used to investigate the diffusion of adsorbed H_2 [11–13].

When $E > 2$ meV or $E < -2$ meV, the scattering process is inelastic. Inelastic scattering is associated with phenomena occurring with well-defined energies like phonons and vibrations (Figure 6) [19,81]. In case of the diffusion of adsorbed H_2, inelastic neutron scattering can occur when the unrestricted diffusion of the H_2 molecule is hindered by the strong H_2-adsorbent interaction. In that case, the energy exchange between the neutron and the H_2 molecule does not appear in the quasi-elastic region as is the case with H_2 diffusion. Instead, the strongly adsorbed H_2 molecule can exhibit a transition at a well-defined rotational energy level of 14.7 meV (para- to ortho-H_2 transition), which is detected in the inelastic region (Figure 6) [13,76,83–85].

4.3.2. Quasi-elastic neutron scattering method

Normal H_2 gas consists of two H_2 isomers with different nuclear spin alignments – ortho-H_2 (o-H_2) and para-H_2 (p-H_2). The neutron scattering cross-section of o-H_2 ($80 \cdot 10^{-28}$ m^2) is considerably larger than for p-H_2 ($< 0.9 \cdot 10^{-28}$ m^2) at 2 meV [11]. Therefore, the quasi-elastic broadening originating only from o-H_2 can be detected and analyzed with QENS in this energy range. When the neutron scatters from H_2, coherent contribution can be considered negligible and only the incoherent contribution is accounted for because H_2 has a large incoherent scattering cross-section ($80 \cdot 10^{-28}$ m^2) and a small coherent scattering cross-section ($2 \cdot 10^{-28}$ m^2) [86]. Thus, Equation 6 is written as Equation 7.

$$\frac{\delta^2\sigma}{\delta E \delta \Omega} \propto \frac{|k_\mathrm{f}|}{|k_\mathrm{i}|} b_\mathrm{inc}^2 S_\mathrm{inc}(Q,E) \tag{7}$$

$S_\mathrm{inc}(Q,E)$ cannot be measured directly and, instead, the experimental dynamic structure factor denoted as $S(Q,E)$, which is proportional to the convolution of the incoherent dynamic structure factor of H_2 $S_{H2}(Q,E)$ with the resolution function $R(Q,E)$ of the spectrometer is measured (Equation 8).

$$S(Q,E) = S_{H2}(Q,E) \otimes R(Q,E) \tag{8}$$

Here, symbol $\otimes$ denotes the convolution product.

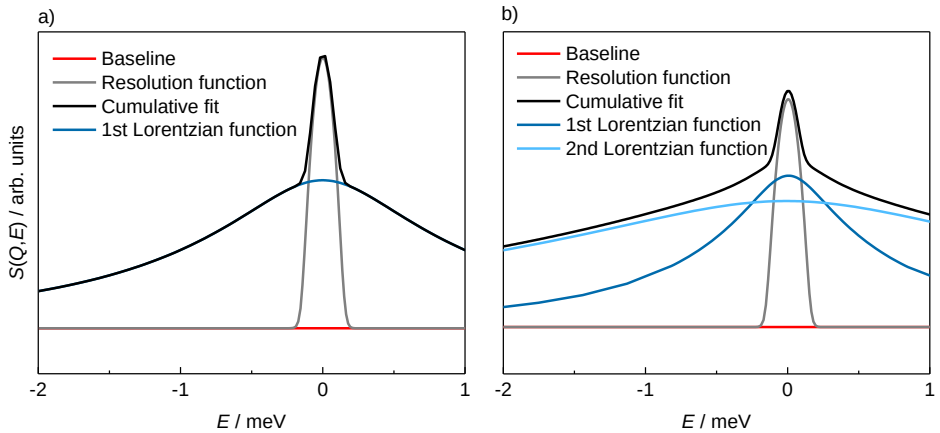

Figure 7. Deconvolution of the dynamic structure factor into an elastic component (resolution function) and a) one quasi-elastic component (Lorentzian function) and b) two quasi-elastic components (two Lorentzian functions).

$S(Q,E)$ can be composed of elastic and quasi-elastic (Lorentzian function) components (Figure 7a). The elastic component denotes scattering from H_2 which motion is too slow to be observable within the experimental resolution. Quasi-elastic component, described with Lorentzian function, arises from the motions of H_2 that take place within the experimental time window of the instrument. When resolved H_2 motions take place in multiple timescales, the quasi-elastic component can consist of multiple components of quasi-elastic scattering (multiple Lorentzian functions) (Figure 7b). Motions of H_2 that are faster than the experimental time window contribute to the flat background. With a QENS instrument, the lower limit of the timescale studied is set by the width of the instrument energy resolution.

To deconvolve the different spectral contributions to each measured neutron scattering spectrum, the data are fitted with a functional form, $S_{\mathrm{fun}}(Q,E)$, comprised of elastic and quasi-elastic components, an instrumental resolution function, and a constant baseline (Equation 9).

$$S_{\mathrm{fun}}(Q,E) = \left[A_0\delta(E) + \sum_{\mathrm{i}}^{\mathrm{n}} A_{\mathrm{i}}(Q)L(E,\Gamma_{\mathrm{i}})\right] \otimes R(Q,E) + y_0 \qquad (9)$$

Here, $S_{\mathrm{fun}}(Q,E)$ is the functional form of dynamic structure factor, Q is the scattering vector value, E is the energy transfer, $\delta(E)$ is the Dirac delta function describing the elastic scattering, $A_0(Q)$ and $A_{\mathrm{i}}(Q)$ are the fractions of elastic and quasi-elastic scattering signals, n is the number of quasi-elastic components, $L(E,\Gamma_{\mathrm{i}})$ is the Lorentzian function which describes mathematically the quasi-elastic component, Γ is the half-width at half maximum (HWHM) of the quasi-elastic component, $R(Q,E)$ in the instrumental resolution function, and y_0 is the baseline.

The presence of two quasi-elastic components can be interpreted as H_2 diffusion over multiple timescales [79]. As a rule of thumb, the two different quasi-elastic components should have HWHM values that are markedly, usually ten times different [19]. Plotting the HWHM values of the quasi-elastic component can give information about the diffusion process, e.g., the type of diffusion process (translational or rotational) and the diffusion coefficient.

4.3.3. Diffusion dynamics established with QENS

The diffusion that is measured under the influence of a concentration gradient (or chemical potential gradient), i.e., under non-equilibrium conditions, where particles migrate down the concentration (or chemical potential) gradient is usually called transport diffusion. On the other hand, the diffusion that is measured under thermodynamic equilibrium is usually called self-diffusion or tracer diffusion and it describes the movement of individual particles. Another example of self-diffusion is the diffusion of two different isotopes of the same gas, e.g., H_2 and D_2 [87].

When the diffusion process is translational, continuous, and the diffusing particles are unconstrained, considering the spatial range probed by the neutrons, then the diffusion process is described by Fick's law. In this case, the HWHM of the quasi-elastic broadening is linearly related to the Q^2 value (Equation 10) [21].

$$\Gamma = DQ^2 \tag{10}$$

Here, Γ is HWHM of the quasi-elastic broadening, Q is the scattering vector value, and D is the diffusion coefficient.

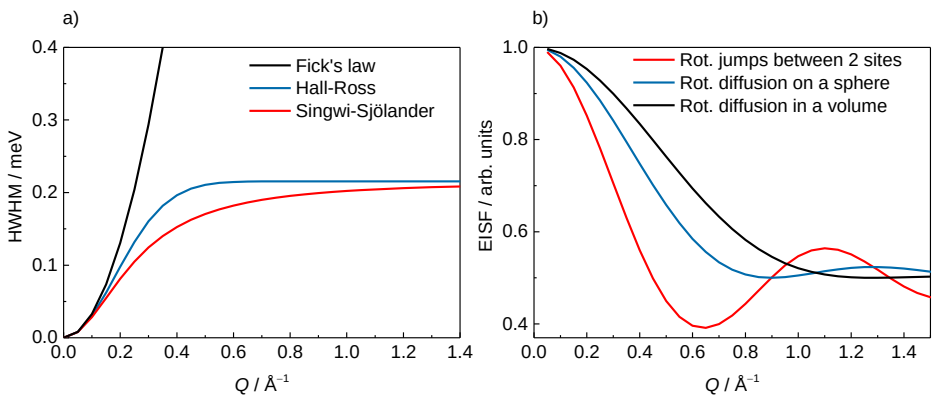

Figure 8. a) Fick's law, Hall-Ross and Singwi-Sjölander models for analysing translational motions and b) three different models (noted on the graph) for analysing localised rotational motions.

Some systems, such as porous structures, can hinder continuous diffusion, resulting in a jump-like motion with a period of residence time between jumps. In such case, the diffusion process is still described by Fick's law at low Q values (i.e., long length scales in real space), but at large Q values (i.e., short length scales in real space), systematic deviations from Fick's law are observed (Figure 8a). The models that consider the deviations from a continuous diffusion process are called translational jump diffusion models [20,21].

The translational jump diffusion dynamics of H_2 can be described by modeling the obtained Γ vs Q dependence with models proposed by Hall-Ross (Equation 11) and Singwi-Sjölander (Equation 12) [88,89]. These models consider deviations from continuous diffusion described by Fick's law at larger Q values through limiting values of jump lengths, which is caused, for example, by the porous structure of the adsorbent. Hall-Ross model assumes that the jump lengths follow a Gaussian distribution which describes jump diffusion in a restricted volume, e.g., in narrow pores. The model proposed by Singwi and Sjölander, originally developed for liquid water, assumes an exponential jump length distribution and characterizes diffusion which alternates between oscillatory and directed motions.

$$\Gamma_{\mathrm{HR}}(Q) = \frac{\hbar}{\tau}\left(1 - \exp(-Q^2\tau D)\right) \tag{11}$$

$$\Gamma_{\mathrm{SS}}(Q) = \frac{\hbar D Q^2}{1 + DQ^2\tau} \tag{12}$$

Here, $\Gamma(Q)$ is the HWHM of the quasi-elastic component at a given Q value, HR denotes the Hall-Ross model and SS denotes Singwi-Sjölander model, $\hbar$ is the reduced Planck constant, τ is the residence time, D is the diffusion coefficient, the mean jump length $\langle l \rangle$ is calculated as $\langle l \rangle = \sqrt{6tD}$.

An Arrhenius-type equation can be used to describe the temperature dependency of diffusion coefficients (Equation 13). By applying this relation, the activation energy of the diffusion process, E_a, and the extrapolated diffusion coefficient at infinite temperature, D_0, can be calculated from the slope and intercept of the graph, respectively [90].

$$D = D_0 \exp\left(-\frac{E_a}{RT}\right) \tag{13}$$

Here, D is the diffusion coefficient, D_0 is the diffusion coefficient at infinite temperature, R is the universal gas constant (8.314 J mol^{-1} K^{-1}), and T is the temperature.

When the diffusion process is not translational, but is rotational, then the HWHM values of the quasi-elastic broadening are independent of the Q value. To get information about the geometry of the motion and the percentage of mobile

particles contributing to the QENS signal, the elastic incoherent structure factor (EISF), A_0, is calculated (Equation 14).

$$\text{EISF} = A_0(Q) = \frac{I_{el}(Q)}{I_{el}(Q) + I_{qe}(Q)} \tag{14}$$

Here, I_{el} and I_{qe} denote the integrated intensity of the elastic and quasi-elastic components, respectively.

The mobile fraction of species can depend on temperature. As a result, an effective EISF, $A_0'(Q)$, is obtained experimentally instead of the theoretical EISF, $A_0(Q)$. The effective EISF can be calculated from the theoretical EISF as $A_0'(Q) = p_s + p_m \cdot A_0(Q)$, where p_s and p_m are the relative fractions of static (over the experimental timescale) and mobile particles, respectively, and which sum up to unity [19].

The geometry of the motions is investigated by fitting experimentally determined EISF with theoretical models (Figure 8b). Some examples of these models are:

1) rotational jumps between two sites with distance d [20];

$$A_{0,2site}(Q) = 0.5\big(1 + j_0(Qd)\big) \tag{15}$$

Here, j_0 is the zero-order spherical Bessel function of the first kind.

2) continuous rotational diffusion on the surface of a sphere with a diameter d [20];

$$A_{0,\text{sph}}(Q) = j_0^2(0.5Qd) \tag{16}$$

3) continuous rotational diffusion within the volume of a sphere with a diameter d [20].

$$A_{0,\text{vol}}(Q) = \left[\frac{3\,j_1(0.5Qd)}{0.5Qd}\right]^2 \tag{17}$$

Here, j_1 is the first-order spherical Bessel function of the first kind.

5. EXPERIMENTAL

In this work, the porous carbons have been derived from commercial Mo_2C at synthesis temperatures of 700 °C, 800 °C, and 900 °C and from TiC synthesized using the sol-gel process. The denotation of the CDCs is presented in Table 2.

Table 2. Synthesis conditions and denotations of the investigated CDCs.

Carbide	Origin of the carbide	Chlorination temperature of the carbide	H_2 reduction temperature	Denotation	Ref
Mo_2C	Commercial	700 °C	900 °C	Mo_2C-CDC 700	24
		800 °C		Mo_2C-CDC 800	
		900 °C		Mo_2C-CDC 900	
TiC	Synthesized in-house using the sol-gel process	950 °C		Sol-gel TiC-CDC	45

5.1. Gas adsorption data

Gas adsorption isotherms of all the samples were measured with ASAP2020 (Micromeritics, USA). The isotherms were measured with N_2, Ar, CO_2, and H_2 at 77 K, 87 K, 273 K, and 77 K, respectively. Before the adsorption measurements, the samples were outgassed at 300 °C and at a vacuum of at least 13 μbar for 12 h.

The pore size distributions were calculated by applying the two-dimensional non-local density functional theory model for carbon materials with heterogeneous surfaces (2D-NLDFT-HS), using the SAIEUS (Micromeritics, USA) software [62]. For Mo_2C-CDC 700, Mo_2C-CDC 800, and Mo_2C-CDC 900, the pore size distributions were calculated by applying the 2D-NLDFT-HS models simultaneously to N_2, Ar, CO_2, and H_2 isotherms (developmental version of SAIEUS). For sol-gel TiC-CDC, the pore size distribution was calculated by applying the 2D-NLDFT-HS models simultaneously to N_2, CO_2, and H_2 isotherms (developmental version of SAIEUS). 2D-NLDFT-HS model-based specific surface area, S_{DFT}, and volume of pores, V_{DFT}, were calculated. The volume of the ultramicropores (3 Å < w < 7 Å), V_{ump}, the volume of the supermicropores (7 Å < w < 20 Å), V_{smp}, and the volume of the mesopores (20 Å < w < 500 Å), V_{meso}, were calculated from the cumulative pore volume.

5.2. Wide-angle X-ray scattering data

A wide-angle X-ray scattering (WAXS) pattern of the CDC samples were obtained using a D8 Advance (Bruker, Germany) diffractometer and Cu Kα radiation of wavelength 1.5406 Å was used. The scattering pattern was measured in the 2θ range from 13° to 80° with a counting time of 166 s per step and a step size of 0.0128° using a LynxEye detector.

Fitting of the diffractograms was performed across the full measured 2θ range with CarbX software, resulting in 14 inter- and intralayer parameters [64,66]. In this thesis, the average graphene-like platelet size, L_a, the average stacking size, L_c, the average interlayer spacing, a_3, and the average number of graphene-like layers per stack, $\langle N \rangle$ calculated as $\langle N \rangle = \frac{L_c}{a_3(1+\kappa_c)}$, where κ_c is the polydispersity of the stack height) are of main interest for the characterization of the level of ordering of the graphenic domains in the CDC materials.

5.3. Quasi-elastic neutron scattering data

To investigate H_2 self-diffusion in CDCs, quasi-elastic neutron scattering (QENS) experiments were performed. The QENS measurements for Mo_2C-CDC 700, Mo_2C-CDC 800, and Mo_2C-CDC 900 were performed using the time-of-flight spectrometer NEAT′ 2016 at the neutron source BER II in Helmholtz Zentrum Berlin (HZB), Germany [91]. This data can be accessed at Ref [92]. The QENS measurement for sol-gel TiC-CDC was performed using spectrometers IRIS and MARI at ISIS neutron and muon source, UK [93,94]. The data for IRIS and MARI measurements can be accessed at Ref. [95] and Ref. [96], respectively.

The sample handling process was identical for all of the samples. Before all the QENS measurements, the CDCs were outgassed for >17 h at >250 °C to remove air moisture and other adsorbed species. After the outgassing process, the CDCs were transferred into a double-walled annular cylindrical aluminium sample can. The sample thickness of 0.2 cm was chosen so that the multiple scattering effects could be considered negligible. All sample handling and preparation were performed in a glovebox filled with inert gas.

The QENS experiments with the CDCs were identical in principle and conducted as follows:

1. The signal from outgassed Mo_2C-CDCs was measured at fixed temperatures from 50 K to 100 K with a step of 10 K. For outgassed sol-gel TiC-CDC, the signal was measured from 20 K to 100 K with a step of 20 K and additionally at 70 K.

2. The samples were cooled down to 77 K using a He cryostat and H_2 was dosed in the sample holder until the pressure reached the $p_{H2,load}$ value in Table 3, which resulted in the total amount of H_2 of n_{H2} in the sample holder.

Table 3. H_2 loading pressures ($p_{H2,load}$) at 77 K and the corresponding total amount of H_2 per 1 g of CDC (n_{H2}) in the closed sample cell.

	Lowest H_2 loading		Moderate H_2 loading		Highest H_2 loading	
	$p_{H2,load}$ / mbar	n_{H2} / mmol g^{-1}	$p_{H2,load}$ / mbar	n_{H2} / mmol g^{-1}	$p_{H2,load}$ / mbar	n_{H2} / mmol g^{-1}
Mo_2C-CDC 700	68	4	1047	21	10 028	125
Mo_2C-CDC 800	86	3	1056	21	9972	138
Mo_2C-CDC 900	86	3	1017	18	10 193	121
Sol-gel TiC-CDC	14	1.7	225	10	969	31

3. The sample holder was disconnected from the gas dosing apparatus and the CDCs containing H_2 were measured at fixed temperatures ranging from 10 K to 100 K. The fixed temperature values at which the neutron scattering signal is measured and analysed in this thesis can be seen in Table 4. After each temperature change, the system was let to reach an equilibrium during approximately 40 min before the start of the QENS measurement. After each increase of H_2 loading, the system was equilibrated for approximately 1 h.

Table 4. The fixed temperature values at which the neutron scattering signal is measured and analysed.

H_2 loading	Sample	10 K	30 K	50 K	60 K	70 K	80 K	90 K	100 K
Lowest	Mo_2C-CDC 700			x	x	x	x	x	x
	Mo_2C-CDC 800			x	x	x	x	x	x
	Mo_2C-CDC 900			x	x	x	x	x	x
	Sol-gel TiC-CDC	x	x	x			x		
Mode-rate	Mo_2C-CDC 700			x	x	x	x	x	x
	Mo_2C-CDC 800			x	x	x	x	x	x
	Mo_2C-CDC 900			x	x	x	x	x	x
	Sol-gel TiC-CDC			x			x		x
Highest	Mo_2C-CDC 700			x	x	x	x	x	x
	Mo_2C-CDC 800			x	x	x	x	x	x
	Mo_2C-CDC 900			x	x	x	x	x	x
	Sol-gel TiC-CDC			x			x		x

Steps 2.–3. were repeated at moderate and highest H_2 loading values for temperatures noted in Table 4. The H_2 pressure in the sample cell was monitored at all times and used to calculate the sample surface coverages and pore volume occupancies at all conditions throughout all experiments.

For detector normalization and background subtraction, the signal from the vanadium cells and the empty sample holders was measured for all systems and QENS experiments. For the Mo_2C-CDC materials, the signal from vanadium was used as the resolution function during subsequent data analysis. For sol-gel TiC-CDC, the neutron scattering data obtained at the lowest temperature (10 K for IRIS and 20 K for MARI) at the lowest H_2 loading were used for instrument calibration and resolution purposes. At these lowest T and n_{H2} conditions applied, the H_2 adsorbed in the sol-gel TiC-CDC could be presumed static, e.g., frozen solid in the pores, at least on the experimental timescales afforded by the used neutron instrumental set-up.

The energy resolution, momentum transfer, and upper experimental observation time and spatial range configurations used for NEAT, IRIS, and MARI spectrometers are summarized in Table 5.

Table 5. The characteristics of the NEAT'2016, IRIS and MARI instruments and configurations used.

	Energy resolution / meV	Upper experimental observation time[a] / ps	Q-range / Å^{-1}	Spatial range[b] / Å	Ref
NEAT'2016	0.1	80	0.3–2.5	3–20	[91]
IRIS (PG002)	0.0175	150	0.42–1.85	3–15	[93]
MARI	0.43	10	0.4–6	1–16	[94]

[a] – Determined from the point where the Fourier transformed resolution function of the instrument goes to zero
[b] – Calculated as $2\pi / Q$

For NEAT'2016 spectrometer [91], the neutrons were detected from −2 meV to 2 meV at the lowest H_2 loading and from −3 meV to 2 meV at the moderate and highest H_2 loading. Negative energy transfer means that neutrons gained energy during the scattering process and positive energy transfer means that neutrons lost energy during the scattering process. The reduced data were collated in three different Q ranges: from 0.2 Å^{-1} to 2.45 Å^{-1}, from 0.25 Å^{-1} to 2.5 Å^{-1}, and from 0.3 Å^{-1} to 2.4 Å^{-1}, with a step size of 0.15 Å^{-1}.

For IRIS spectrometer [93], the neutron scattering data were collected with the spectrometer configured to energy analyze the scattered neutron beam using the 002 graphite (PG002) analyzer reflection. On IRIS, the scattered neutrons were detected in the energy transfer range from –0.3 meV to 1.2 meV. The reduced data were collated in the Q range from 0.42 Å^{-1} to 1.8 Å^{-1} into five distinct Q groups/values at the lowest H_2 loading and nine Q groups at moderate and highest H_2 loading.

For MARI spectrometer [94], the neutrons were detected in the energy transfer range from −20 meV to 20 meV. The reduced data were collated in the Q range

from 0.4 Å^{-1} to 1.8 Å^{-1} into nine Q groups at moderate and highest H_2 loading to match the Q grouping of the scattering data from IRIS.

During the analysis, the Q ranges are truncated because of the coherent scattering occurring due to the graphitic carbon (002) Bragg peak above ~1.8 Å^{-1} (also in Figure 4a). The data reduction and analysis for all experiments were carried out using Mantid [97] and OriginLab 2016 (OriginLab Corporation) software.

5.3.1. Deconvolution method of the dynamic structure factor

For the Mo_2C-CDC materials measured with NEAT'2016 spectrometer, at the lowest H_2 loading, the QENS data are fitted with a model containing one quasi-elastic component (Equation 9, where $n = 1$) described with one Lorentzian function (Figure 7a). At the moderate and highest H_2 loading, the data are fitted with a model containing two quasi-elastic components (Equation 9, where $n = 2$) to confirm and investigate H_2 diffusion in two distinguishable timescales (Figure 7b). However, at moderate H_2 loading and at $T = 50$ K, the narrower of the two quasi-elastic components could not be reliably deconvoluted and, thus, is fitted with a model containing one Lorentzian function (Equation 9, where $n = 1$). The $S(Q,E)$ measured at the highest H_2 loading are fitted with a model containing two Lorentzian functions (Equation 9, where $n = 2$) throughout the entire T range.

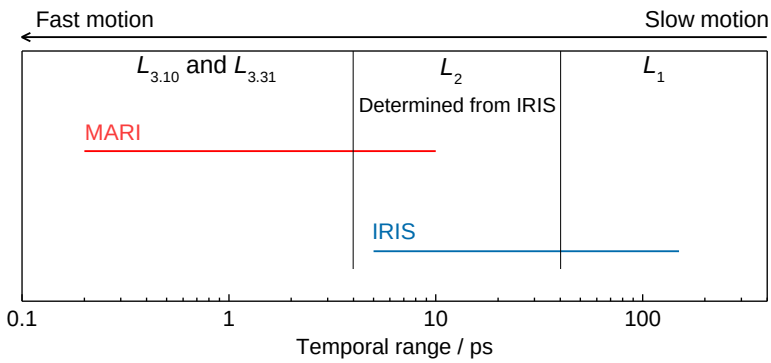

Figure 9. Schematics of H_2 components analyzable in the temporal ranges of MARI and IRIS spectrometers.

For sol-gel TiC-CDC measured with IRIS and MARI spectrometers, a different fitting protocol is applied with the aim of reliably determining more types of H_2 motions. In total, four self-diffusional dynamics, denoted with L_1, L_2, $L_{3.10}$ and $L_{3.31}$ are distinguished and analyzed (Figure 9). The subscripts 10 and 31 in $L_{3.10}$ and $L_{3.31}$, respectively, denote the values of the total amount of H_2 per 1 g of sol-gel TiC-CDC in the closed sample cell in mmol g^{-1} at which the width of the quasi-elastic component is determined.

The $S(Q,E)$-s obtained on IRIS at $n_{H2} = 1.7$ mmol g^{-1} are fitted with a model containing one Lorentzian function (Equation 9, where $n = 1$) – L_1. The $S(Q,E)$-s obtained on IRIS at $n_{H2} = 10$ mmol g^{-1} are fitted with a model containing two

Lorentzian functions (Equation 9, $n = 2$) – L_1 predetermined at $n_{H2} = 1.7$ mmol g^{-1} and freely fitted L_2. The $S(Q,E)$-s obtained on MARI at $n_{H2} \geq 10$ mmol g^{-1} are fitted with a model containing two Lorentzian functions accounting for two quasi-elastic broadenings (Equation 9, $n = 2$) – L_2 predetermined at $n_{H2} = 10$ mmol g^{-1} obtained from data measured on IRIS $S(Q,E)$-s and freely fitted $L_{3.10}$ (at $n_{H2} = 31$ mmol g^{-1}, freely fitted $L_{3.31}$).

MARI and IRIS spectrometers have an overlap in the temporal range where H_2 motions described with L_2 take place (Figure 9). Thus, the L_2 component is fixed based on the results obtained at $n_{H2} = 10$ mmol g^{-1} from the data obtained on the IRIS spectrometer to account for the slower motions probed with MARI, revealing a more reliable broader Lorentzian function (L_3). The motions of H_2 component described with L_3 have a clear difference in linewidths at $n_{H2} = 10$ mmol g^{-1} and at $n_{H2} = 31$ mmol g^{-1} and are denoted with $L_{3.10}$ at $n_{H2} = 10$ mmol g^{-1} and $L_{3.31}$ at $n_{H2} = 31$ mmol g^{-1}, respectively. Linewidths of the L_2 component are kept constant at $n_{H2} \geq 10$ mmol g^{-1} as they are equal within the uncertainty margins at $n_{H2} \geq 10$ mmol g^{-1}.

6. RESULTS AND DISCUSSION

6.1. Physical characterisation of CDCs

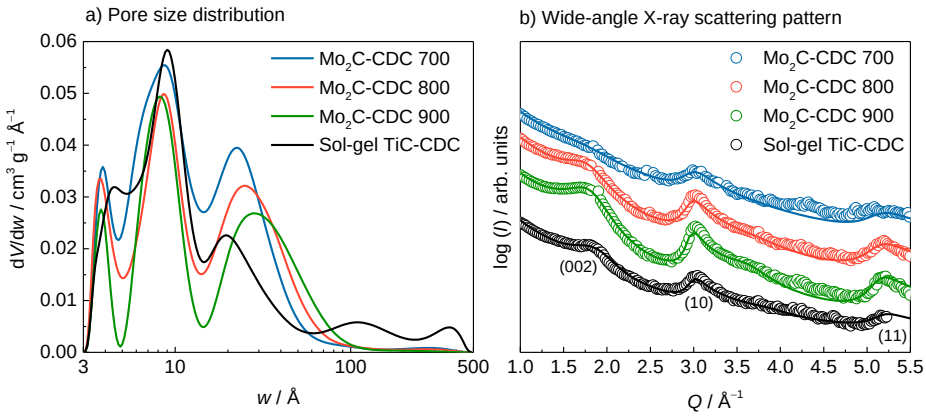

Figure 10. a) Pore size distributions of Mo_2C-CDC 700, Mo_2C-CDC 800, and Mo_2C-CDC 900 calculated by simultaneously applying 2D-NLDFT-HS model to the N_2, Ar, CO_2, and H_2 adsorption data and the pore size distribution of sol-gel TiC-CDC by simultaneously applying 2D-NLDFT-HS model to the N_2, CO_2, and H_2 adsorption data and b) WAXS pattern of Mo_2C-CDC 700, Mo_2C-CDC 800, Mo_2C-CDC 900, and sol-gel TiC-CDC (circles) and fit curve (solid line).

The pore size distributions have been previously calculated for the same Mo_2C-CDC materials on three different occasions by applying the 2D-NLDFT-HS model simultaneously to the N_2 and CO_2 adsorption data, to the Ar and CO_2 adsorption data and only to the N_2 adsorption data [24,29,77]. The pore size distribution of sol-gel TiC-CDC has also been previously calculated by applying the 2D-NLDFT-HS model simultaneously to the N_2 and CO_2 adsorption data [45]. The pore size distributions modelled in Refs. [24,29,77] are bimodal, with the first maximum corresponding to pores with $w < 20$ Å (micropores) and the second maximum corresponding to pores with 20 Å $< w <$ 500 Å (mesopores). Including the H_2 adsorption data and applying the 2D-NLDFT-HS model simultaneously to N_2, Ar, CO_2, and H_2 adsorption data extends the lower analysis limit of the obtained pore size distribution down to the ultramicropore range and gives a more precise picture of the porous structure. Thus, trimodal pore size distributions are obtained (Figure 10a), where the first maximum corresponds to pores in the ultramicropore range and where the contribution of ultramicro- and supermicropores to the pore volume is higher than previously determined.

Table 6. Pore structure characteristics obtained from the global fitting of multiple gas adsorption isotherms data with 2D-NLDFT-HS models using SAIEUS software and the main parameters obtained from fitting of WAXS patterns using CarbX software [62,64].

	Mo_2C-CDC 700	Mo_2C-CDC 800	Mo_2C-CDC 900	Sol-gel TiC-CDC
S_{DFT} / $m^2\ g^{-1}$	1810	1500	1290	1560
V_{DFT} / $cm^3\ g^{-1}$	1.61	1.52	1.42	2.40
V_{ump} / $cm^3\ g^{-1}$	0.12 (8%)	0.08 (5%)	0.07 (5%)	0.11 (5%)
V_{smp} / $cm^3\ g^{-1}$	0.49 (30%)	0.36 (24%)	0.26 (18%)	0.41 (17%)
V_{meso} / $cm^3\ g^{-1}$	1.00 (62%)	1.08 (71%)	1.09 (77%)	1.88 (78%)
L_a / Å	22±6[a]	38±11	63±19	50±15
L_c / Å	6.2±1.1[a]	12.8±2.3	7.7±1.4	12.5±2.3
a_3 / Å	3.6±0.2[a]	3.6±0.2	3.5±0.2	3.4±0.2
$\langle N \rangle$ / unitless	0.51±0.02[a]	1.05±0.02	0.79±0.02	2.76±0.55

[a] Previously unpublished data. Data are fitted for this thesis by Laura Kalder using the same fitting protocol used for fitting other CDCs published in Ref. [31].
S_{DFT} – specific surface area; V_{DFT} – pore volume; V_{ump} – ultramicropore volume; V_{smp} – supermicropore volume; V_{meso} – mesopore volume; L_a – average graphene-like platelet size; L_c – average stacking size; a_3 – average interlayer spacing; $\langle N \rangle$ – the average number of graphene-like layers per stack

All of the studied CDCs exhibit pores in ultramicro-, supermicro-, and mesopore range. As the chlorination temperature of the Mo_2C-CDC materials is increased, the specific surface area, S_{DFT}, and pore volume, V_{DFT}, decrease (Table 6). Sol-gel TiC-CDC has an S_{DFT} value of 1560 $m^2\ g^{-1}$, which is in a similar range to the rest of the studied CDCs (Table 6). However, the V_{DFT} value of sol-gel TiC-CDC (2.40 $cm^3\ g^{-1}$) is considerably higher than the V_{DFT} value for the Mo_2C-CDC materials. Therefore, although all the investigated CDCs exhibit pores in the same pore width range, the main difference between the Mo_2C-CDC materials and the sol-gel TiC-CDC is the volume of mesopores. Namely, sol-gel TiC-CDC exhibits the largest volume of mesopores of 1.88 $cm^3\ g^{-1}$, which accounts for 78% of pores with 3 Å < w < 500 Å.

Ultramicro- and supermicropores can be interpreted as the measure of corrugation/roughness of the pore walls. Thus, a larger volume of ultra- and supermicropores in Mo_2C-CDC 700 and Mo_2C-CDC 800 than in Mo_2C-CDC 900 indicates that the mesopores of Mo_2C-CDC 700 and Mo_2C-CDC 800 exhibit a higher degree of pore wall corrugation than Mo_2C-CDC 900. This corroborates with the contrast-matched small-angle neutron scattering study on the same materials in Ref. [29], which revealed that with the increase in synthesis temperature, the surface roughness/corrugation of pore walls decreases.

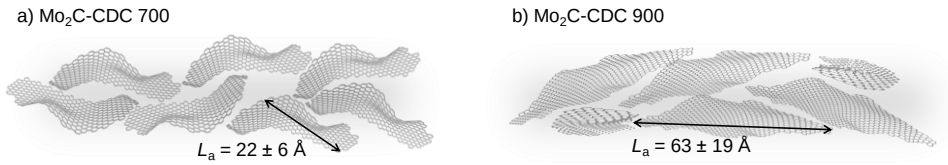

Figure 11. Illustrative representation of the pore wall corrugation of a) Mo_2C-CDC 700 and b) Mo_2C-CDC 900, where L_a is the average graphene-like platelet size from WAXS analysis.

The WAXS patterns of the investigated CDCs have broad and overlapping reflexes and are missing (*hkl*) reflexes (Figure 10b). This is typical of a non-graphitic carbon, indicating that these materials do not have any long-range order, but exhibit short-range order, which is present in the graphenic domains (Figure 4a and section 4.1.3). The average graphene-like platelet size, L_a, of the investigated CDCs, visualized in Figures 11a and 11b, slightly increases as the synthesis temperature of the Mo_2C-CDC materials increases, also considering the uncertainties (Table 6). An increase in the graphene-like domain sizes of the CDCs with the synthesis temperature is also supported by the Raman analysis presented in Ref [31]. The L_a value of the sol-gel TiC-CDC materials is in a similar range as for the Mo_2C-CDC materials (Table 6).

The main difference between the Mo_2C-CDC materials and sol-gel TiC-CDC is the stacking of graphenic layers (Table 6). The sol-gel TiC-CDC has on average 2.76 graphenic layers per stack, while Mo_2C-CDC materials have on average ≤ 1 layer per stack. Therefore, on average, the graphene-like layers are not stacked and do not form ordered domains with each other in the Mo_2C-CDC materials. This also correlates with the porous structure analysis of the CDCs. Namely, the microporosity in CDCs forms between imperfectly stacked graphene-like layers and between the stacks themselves. When the stacking of graphene-like layers becomes more ordered, some of the microporosity is lost.

To summarize, sol-gel TiC-CDC has a relatively high stacking of graphene-like layers compared to the Mo_2C-CDC materials. Overall, the studied Mo_2C-CDC materials have a relatively large volume and high ratio of ultramicro- and micropores, and it decreases as the chlorination temperature increases from 700 °C to 900 °C. The sol-gel TiC-CDC, on the other hand, stands out with a large volume of mesopores.

6.2. H_2 diffusion in porous CDCs

To investigate H_2 diffusion in the micro- and mesopores of CDCs, QENS experiments were performed. H_2 pressure in the sample cell was monitored at all temperatures and at all H_2 loading values to calculate the pore occupancy at all experimental conditions. All calculation steps and used parameters can be seen in the supplementary information of Refs. [98,99]. As a summary of these calculations, the pore occupancy values can be seen in Table 7.

Table 7. Occupancy of Mo_2C-CDC materials and sol-gel TiC-CDC pores with H_2 in % out of V_{DFT} based on the consideration that the density of adsorbed H_2 is equal to the density of liquid H_2 (70.85 kg m^{-3}).

H_2 loading	Sample	30 K	50 K	60 K	70 K	80 K	90 K	100 K
Lowest	Mo_2C-CDC 700	–	6	6	6	5	4	3
	Mo_2C-CDC 800	–	7	7	7	6	5	4
	Mo_2C-CDC 900	–	6	6	6	5	4	4
	Sol-gel TiC-CDC	1	1	–	–	1	–	–
Moderate	Mo_2C-CDC 700	–	32	29	25	21	18	15
	Mo_2C-CDC 800	–	35	31	27	23	19	16
	Mo_2C-CDC 900	–	35	31	27	23	19	16
	Sol-gel TiC-CDC	–	12	–	–	8	–	3
Highest	Mo_2C-CDC 700	–	100	100	96	93	90	87
	Mo_2C-CDC 800	–	100	100	100	100	100	100
	Mo_2C-CDC 900	–	100	100	100	100	–[a]	–[a]
	Sol-gel TiC-CDC	–	19	–	–	–[a]	–	–[a]

[a] These values can not be calculated precisely because during the experiments, the pressure transducer was changed to a high-pressure one for which the volumes were not known.

It must be noted that the diffusion of H_2 adsorbed in sol-gel TiC-CDC was measured with two spectrometers – MARI and IRIS – and, thus, in principle, two different pore occupancy values are calculated for the same experimental condition depending, for example, on the gas handling systems installed on both instruments and on the sample mass. However, the H_2 loading values for both measurements performed on MARI and IRIS were chosen intentionally to achieve as similar pore occupancy values as possible – the value presented in Table 7. The pore occupancy values separately for both experiments on MARI and IRIS instruments can be seen in Table S8 in the supplementary information of Ref[99].

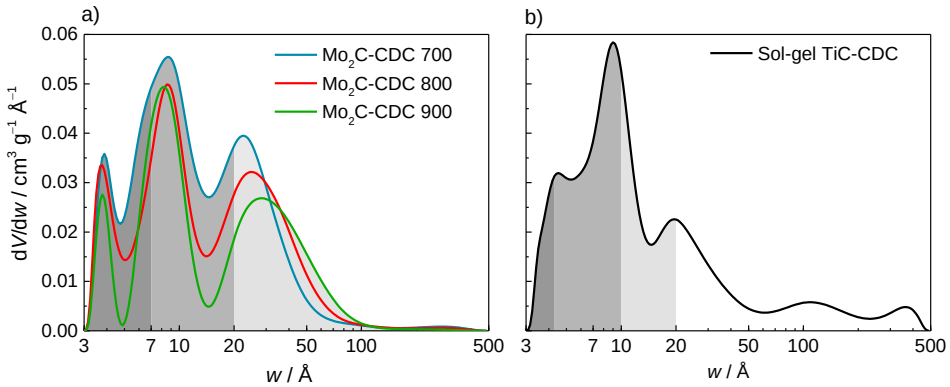

Figure 12. Visualisation of pore occupancy of a) Mo_2C-CDC 700, Mo_2C-CDC 800, Mo_2C-CDC 900 and b) sol-gel TiC-CDC at different H_2 loading conditions and at 50 K, where dark, medium and light gray denote the lowest, moderate, and the highest H_2 loading, respectively.

At the lowest H_2 loading and at 50 K, ~6% of the total pore volume of the Mo_2C-CDC materials is occupied by H_2. As ultramicropores make up 5–8% of the total pore volume of Mo_2C-CDC materials depending on the CDC (Table 6) and smaller pores are filled first, H_2 occupies mostly ultramicropores of Mo_2C-CDC materials (Figure 12a). At the lowest H_2 loading and at 30 K, ~1% of the total pore volume of the sol-gel TiC-CDC is occupied by H_2. As ultramicropores make up ~5% of the total pore volume of sol-gel TiC-CDC, then at these conditions, H_2 does not occupy all ultramicropores, but only the active adsorption sites present in the ultramicropores of sol-gel TiC-CDC (Figure 12b).

At the moderate H_2 loading and at 50 K, 32–35% of the total pore volume of the Mo_2C-CDC materials is occupied by H_2, depending on the CDC. As micropores make up 22–38% of the total pore volume of the Mo_2C-CDC materials depending on the CDC (Table 6) and smaller pores are filled first, H_2 occupies mostly micropores of the Mo_2C-CDC materials (Figure 12a). At the highest H_2 loading and at 50 K, H_2 occupies in addition to micropores also the mesopores of the Mo_2C-CDC materials indicated by the pore occupancy value > 100% (Figure 12a). A pore occupancy value > 100% also shows that the micro- and mesoporous structure of the Mo_2C-CDCs is saturated with H_2.

Thus, for dosing sol-gel TiC-CDC with H_2, lower H_2 loading values have been chosen. At 50 K and at moderate and highest H_2 loading, ~12% and ~19% of the total pore volume is occupied with H_2, respectively. Micropores make up ~22% of the total pore volume (Table 6), meaning that at moderate H_2 loading, H_2 occupies most of the micropores (Figure 12b). At the highest H_2 loading, H_2 occupies almost all of the micropores of the sol-gel TiC-CDC and is very likely already adsorbed in some of the mesopores (Figure 12b).

6.2.1. Restricted H_2 self-diffusion in CDCs

In this section, only the QENS spectra at the lowest H_2 loading pressures are analysed. At the lowest H_2 loading and at 50 K, H_2 is adsorbed in ~6% of the available pore volume of the Mo_2C-CDC materials, while ultramicropores make up 5–8% of the Mo_2C-CDCs of the pore volume depending on the CDC (Figure 12a). For sol-gel TiC-CDC, at the lowest H_2 loading and at 30 K, H_2 is adsorbed in ~1% of the available pore volume, while ultramicropores make up 5% of the pore volume (Figure 12b). Thus, at these conditions, H_2 is adsorbed in the smallest accessible adsorption sites.

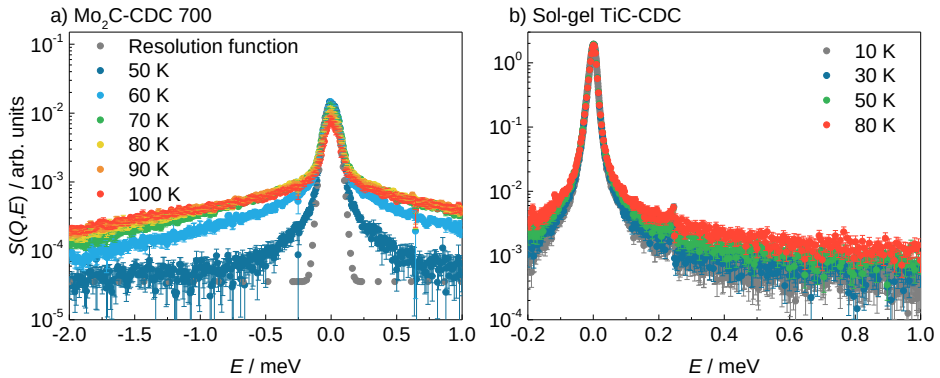

Figure 13. The $S(Q,E)$ of H_2 adsorbed at the lowest n_{H2} value in a) Mo_2C-CDC 700 (summed over Q from 0.8 $Å^{-1}$ to 0.95 $Å^{-1}$) measured on NEAT and b) sol-gel TiC-CDC (summed over Q from 0.42 $Å^{-1}$ to 1.8 $Å^{-1}$) measured on IRIS, where signal at 10 K was used as the resolution function.

At the lowest H_2 loading when H_2 is occupying the smallest accessible adsorption sites, the QENS spectra of H_2 adsorbed in the CDCs exhibit a quasi-elastic broadening (Figure 13a,b). This quasi-elastic broadening indicates that the increase in temperature provides enough additional kinetic energy to the adsorbed H_2 for self-diffusion processes to be noted at 50 K for the Mo_2C-CDC materials and at a T as low as 30 K for sol-gel TiC-CDC.

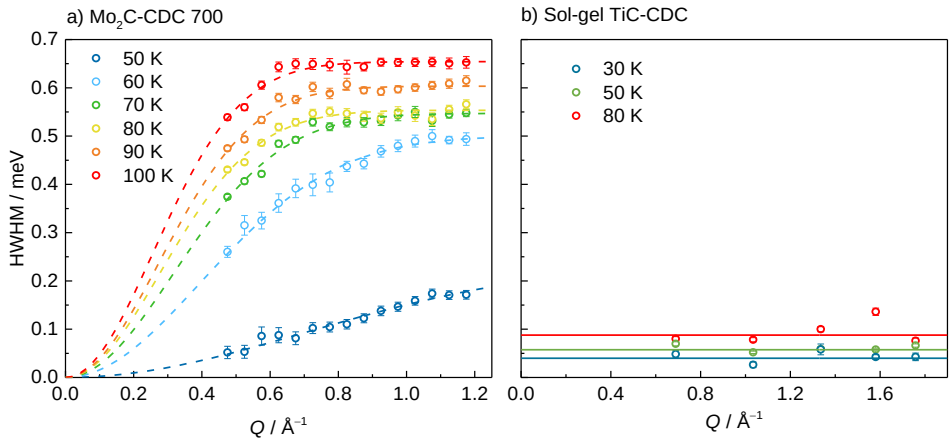

Figure 14. Half widths at half maxima (HWHM) of Lorentzian functions fitted to the quasi-elastic component describing the self-diffusion of H_2 adsorbed in a) Mo_2C-CDC 700 (fitted with Hall-Ross model and denoted with dashed lines) and b) sol-gel TiC-CDC (fitted with linear function with slope set to 0 and denoted with solid lines) at the lowest n_{H2} value and at various temperatures noted on the graphs.

The shape of the Γ vs Q graphs indicates that the self-diffusion process of H_2 adsorbed in the Mo_2C-CDC materials is translational (Figure 14a). For sol-gel TiC-CDC, on the other hand, the shape of the Γ vs Q graph is Q-independent, which is indicative of rotational and constrained self-diffusion (Figure 14b). The difference in the self-diffusion of H_2 adsorbed in these CDCs could be caused by different aspects.

Firstly, in sol-gel TiC-CDC, H_2 occupies only ~1% of the total pore volume, i.e., H_2 is adsorbed in the smallest ultramicropores, while in Mo_2C-CDC materials, H_2 occupies ~6% of the total pore volume and is likely adsorbed in all available ultramicropores and already in some supermicropores. In supermicropores with $w > 7$ Å, two energetically favored adsorption sites fit between the pore walls (i.e., adsorption in two layers is favored), whereas ultramicropores with w from 4 Å to ~6 Å have only one energy minimum, referring to one layer of adsorbed H_2 between pore walls (Figure 5b, c). The constrained rotational self-diffusion of H_2 in the ultramicropores of sol-gel TiC-CDC could be caused by either the single energy minimum or by the two energy minima at these adsorption sites. These energy landscapes restrict the translational motion of adsorbed H_2 molecules that were observed in Mo_2C-CDC materials.

Secondly, the observation of constrained rotational self-diffusion of H_2 adsorbed in sol-gel TiC-CDC can be due to the shifted upper experimental observation time of the IRIS spectrometer compared to the NEAT'2016 spectrometer, which is used to investigate the self-diffusion of H_2 adsorbed in the Mo_2C-CDCs. Namely, IRIS affords the upper experimental observation time up to 150 ps, while NEAT'2016 offers the upper experimental observation time up to 80 ps (Table 5). Thus, with IRIS it is possible to probe slower dynamics than with NEAT'2016. Therefore, it is possible that if the self-diffusion of H_2 adsorbed in

Mo_2C-CDCs is investigated using an instrument with the same energy resolution as IRIS, rotational self-diffusion might also be observed.

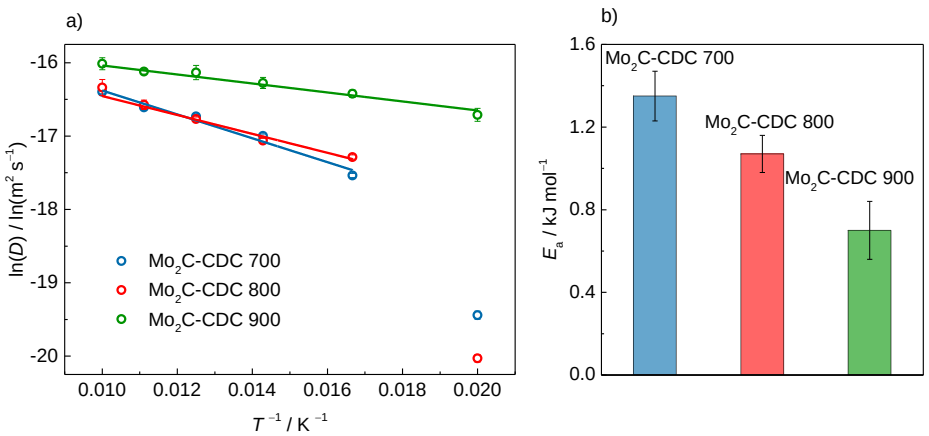

Figure 15. a) Arrhenius plots of diffusion coefficients of H_2 adsorbed in Mo_2C-CDC 700, Mo_2C-CDC 800 and Mo_2C-CDC 900 at the lowest n_{H2} value fitted with Arrhenius relation (solid lines) and b) the calculated activation energy values (E_a).

The translational self-diffusion of H_2 adsorbed in the Mo_2C-CDC materials has a clear dependency on the synthesis temperature of the CDCs (Figure 15a). Namely, the translational self-diffusion coefficients are lower and the activation energy of H_2 adsorbed in Mo_2C-CDC 700 is higher than for Mo_2C-CDC 900 (Figure 15b). Therefore, the porous and graphenic structure of Mo_2C-CDC 700 has a more enhanced capability to confine adsorbed H_2 than Mo_2C-CDC 900. This is caused by the larger volume and ratio of ultramicropores (higher pore wall corrugation) present in Mo_2C-CDC 700 than in Mo_2C-CDC 900 (Table 6).

The self-diffusion of H_2 adsorbed in Mo_2C-CDC 700 and Mo_2C-CDC 800 at 50 K is strongly confined by the ultramicropores as the D value at 50 K is even lower than the D value of liquid H_2 at 15 K [100]. This phenomenon was investigated and analysed in Ref [101]. The majority of mobile H_2 at 50 K is strongly confined inside the ultramicropores of the Mo_2C-CDC 700 and Mo_2C-CDC 800 due to diffusional limitations in ultramicropores and/or curved non-ideal graphenic domains. This mobile H_2 is not able to desorb from the ultramicropores and causes a pressure increase inside the ultramicroporous graphenic structure, compressing the graphenic layers into a laterally ordered structure with Bragg peaks emerging in the elastic neutron scattering pattern, and some layers pressed closer than in graphite at near-ambient conditions (Figure 2 in Ref [101]). With the increase to 60 K, the mobility of H_2 increases further, causing additional H_2 pressure inside the pores and inducing the formation of additional graphenic domains during the initial 20 min. After the initial 20 min at 60 K, the overpressurized H_2 pushes the closed porosity open and H_2 desorbs from the pores of Mo_2C-CDC 700 and Mo_2C-CDC 800, causing the disappearance of graphenic domains and complete

restoration of the original CDC structure after 50 min. This phenomenon was not seen for H_2 adsorbed in Mo_2C-CDC 900 likely because this material has a lower ultramicropore volume (Table 6) and smoother pore walls than Mo_2C-CDC 700 and Mo_2C-CDC 800 (Figure 11).

In case of H_2 adsorbed in sol-gel TiC-CDC, the rotational self-diffusion was observed. The residence times between two rotational jumps of the H_2 molecule decrease from ~9 ps to ~3 ps (considering that 1 meV = 1.52 · 10^{12} rad s^{-1}) with the increase in T from 30 K to 80 K. This indicates a temperature-induced increase in the rotational self-diffusion of adsorbed H_2. For comparison, the characteristic rotational self-diffusion times of H_2 adsorbed in mesoporous carbon and exfoliated graphite are in the range of ~0.1–2 ps in the T range from 22 K to 80 K [12]. Since the residence times between rotational jumps of H_2 adsorbed in the CDC studied here are longer, the ultramicropores of sol-gel TiC-CDC can more effectively confine adsorbed H_2.

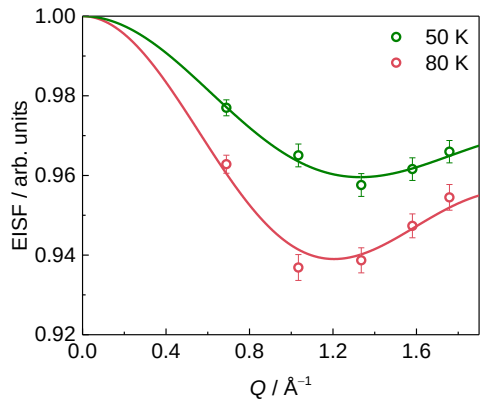

Figure 16. The elastic incoherent structure factor (EISF) response at 50 K and 80 K at n_{H2} = 1.7 mmol g^{-1} fitted with the model assuming jumps between two sites (solid line).

The Q-dependence of the elastic incoherent structure factor (EISF) at n_{H2} = 1.7 mmol g^{-1} indicates that the rotational motions of self-diffusive H_2 are geometrically constrained (Figure 16). To determine the geometry of the rotational motions, the EISF response shown is fitted using three models: (1) H_2 performing rotational jumps between two equidistant sites (Equation 15), (2) continuous rotational diffusion of H_2 on the surface of a sphere (Equation 16), and 3) continuous rotational diffusion of H_2 within the volume of a sphere (Equation 17). The diameter of the confining volume or distance between two sites (d) is determined from the first minimum of the EISF vs Q graph (Figure 16), which is reliably observed in the available Q-range. However, to determine the exact geometry of motion, more data points at higher Q-values would be needed as the differences between the applied rotational diffusion models are subtle.

The best fit is achieved with the model assuming jumps between two sites (Equation 17, Figure 16). The d value is 3.4±0.1 Å and 3.7±0.1 Å at 50 K and

80 K, respectively. Two mechanisms for the restricted jumps of adsorbed H_2 are possible: (1) jumps between opposing pore walls and/or (2) jumps along the pore walls.

In the first case, H_2 molecules exhibit oscillatory motions – H_2 molecules jump between the potential energy minima created by the pore walls. H_2 jumps with distances of 3.4 Å and 3.7 Å can take place in pores with a w of approximately 7 Å, i.e., in large ultramicropores or small supermicropores (Figure 5c). In addition to the spatial limitation of the opposing ultramicropore walls, the neighboring adsorbed H_2 molecules provide a steric barrier as, according to the pressure calculation, 21% and 13% of the monolayer is occupied by H_2 at 50 K and 80 K, respectively.

In the second case, H_2 molecules diffuse along the pore walls, jumping between adsorption sites located on the graphene-like surface. According to Refs. [13,102], these adsorption sites are separated by distances ranging between 3 Å to 5 Å – a range that overlaps with the 3.4 Å and 3.7 Å H_2 jumps determined from EISF analysis. Thus, the H_2 jumps along the pore walls would be between adsorption sites on the graphene-like surface.

The restricted H_2 jumps – both between opposing ultramicropore walls and along the pore walls – show the confining effect of specific adsorption sites in carbon materials, e.g., in ultramicropores. Such a strong H_2 confinement in the ultramicropores at low temperatures lays the foundation for the formation of a high-density adsorbed H_2 phase needed for H_2 storage. However, high-density H_2 phase can form inside mesoporous materials as well. For example, a monolayer adsorption density of 202 kg m^{-3} was observed on mesoporous silica at 20 K and 0.6 bar [103]. At room temperature and higher pressures, slightly larger pores than ultramicropores can also adsorb H_2 as a high-density phase [104]. For example, it has been calculated that an adsorbent containing 1 cm^3 g^{-1} of pores with w = 9 Å would be able to store 8.13 wt% of H_2 at room temperature and 207 bar, which approaches the U.S. Department of Energy system-based target [105].

6.2.2. H_2 self-diffusion over multiple timescales

At the moderate H_2 loading and at 50 K, H_2 is adsorbed in 32–35% of the available pore volume of the Mo_2C-CDC materials, while micropores make up 22–38% of the pore volume of Mo_2C-CDCs depending on the CDC (Figure 12a). For the sol-gel TiC-CDC at moderate and the highest H_2 loading and at 50 K, H_2 occupied ~12% and ~19% of the available pore volume, respectively, while micropores make up 22% of the pore volume of sol-gel TiC-CDC (Figure 12b). Therefore, at these conditions, H_2 is mostly adsorbed in the micropores of the CDCs.

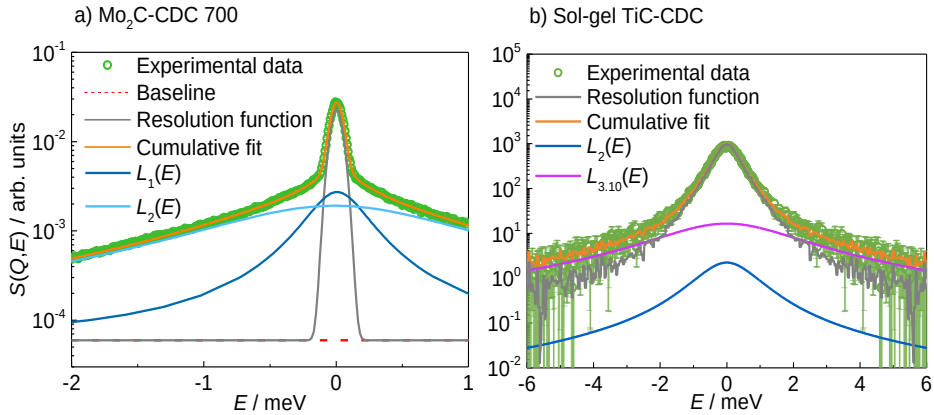

Figure 17. $S(Q,E)$ of H_2 adsorbed in a) Mo_2C-CDC 700 measured on NEAT at $T = 80$ K, $n_{H2} = 21$ mmol g^{-1}, $Q = 0.875$ Å^{-1} and b) sol-gel TiC-CDC measured on MARI at $T = 50$ K, $n_{H2} = 10$ mmol g^{-1}, $Q = 1.3$ Å^{-1} fitted with Equation 12 where $n = 2$.

The neutron scattering spectra of H_2 adsorbed in the micropores of the CDCs exhibit a quasi-elastic broadening as is evident from Figure 17 and as is the case for the lowest H_2 loading, when H_2 is adsorbed predominantly in the ultramicropores. However, the main difference compared to the lowest H_2 loading is that when H_2 loading is increased to moderate H_2 loading, and H_2 is adsorbed in micropores, the self-diffusion of H_2 takes place over multiple timescales, expressed as multiple distinct quasi-elastic broadenings denoted with L_1 and L_2 in Figure 17a and with L_2 and $L_{3.10}$ in Figure 17b.

The optimal number of quasi-elastic broadening for the spectra measured from H_2 adsorbed in the Mo_2C-CDC materials is confirmed with the analysis of reduced chi-squared values, which is presented in the supplementary information of Ref. [98]. For sol-gel TiC-CDC, a different methodology is applied with the aim of distinguishing more quasi-elastic components. For that, the quasi-elastic components are deconvoluted across a wide temporal range by combining QENS data from different experimental conditions and different spectrometers – MARI and IRIS (section 5.3.1).

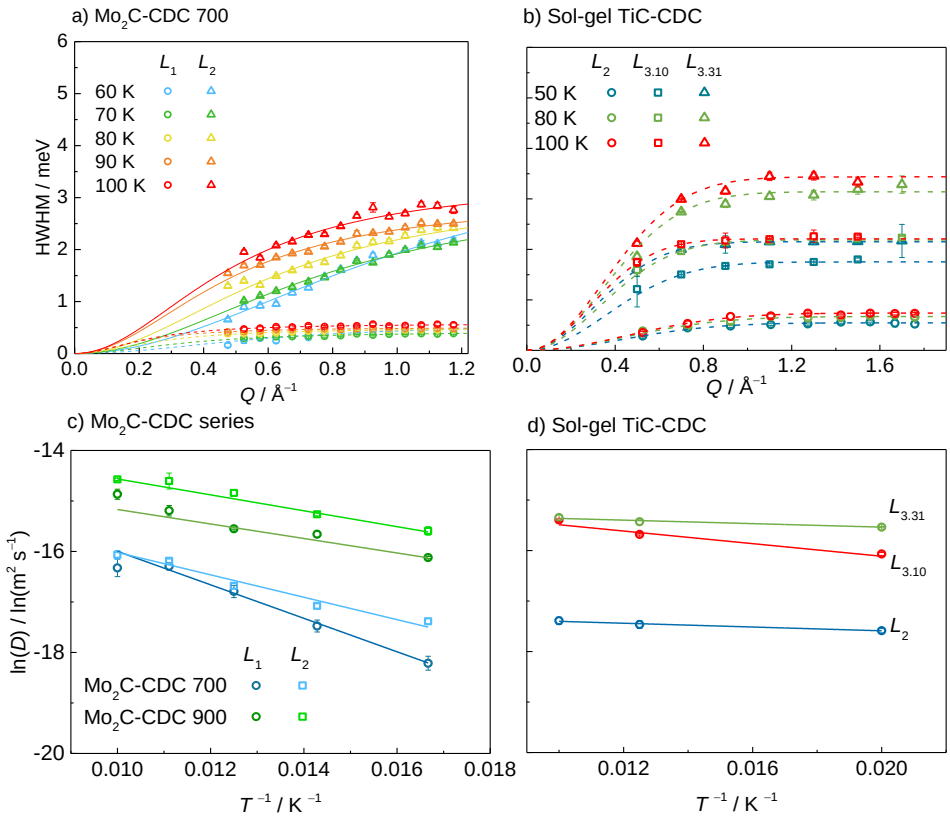

Figure 18. Half width at half maximum (HWHM) of the Lorentzian functions fitted to the quasi-elastic component describing the self-diffusion of H_2 adsorbed in a) Mo_2C-CDC 700, where narrower Lorentzian (L_1) is fitted with Hall-Ross model (dashed line) and broader Lorentzian (L_2) is fitted with Singwi-Sjölander model (solid line) at moderate n_{H2} and in b) sol gel TiC-CDC, where the HWHM-s of L_2, $L_{3.10}$ and $L_{3.31}$ are fitted with Hall-Ross model (dashed line) at moderate and high n_{H2}. Arrhenius plots of the diffusion coefficients of H_2 adsorbed in c) Mo_2C-CDC 700 at moderate n_{H2} and d) sol-gel TiC-CDC at moderate and high n_{H2} fitted with Arrhenius relation (solid line).

The H_2 adsorbed in the Mo_2C-CDC materials and in sol-gel TiC-CDC is self-diffusing over multiple timescales, as indicated by the multiple quasi-elastic components (L_1 and L_2 for Mo_2C-CDC materials and L_2, $L_{3.10}$ and $L_{3.31}$ for sol-gel TiC-CDC) (Figure 18a,b). The self-diffusion over multiple timescales is interpreted as the separable self-diffusion of H_2 adsorbed closer to the pore wall and H_2 adsorbed in multilayers, i.e., in the middle region of the pore. All self-diffusing components adsorbed in the Mo_2C-CDC materials and in sol-gel TiC-CDC follow a translational jump-like diffusion mode. This is evident from the similar and distinctive shape of the HWHM vs Q plots (Figure 18a,b). In addition, the self-diffusion processes of H_2 adsorbed in Mo_2C-CDC materials as well as sol-gel TiC-CDC have an activation barrier, indicated by the D values which follow an

Arrhenius-type relation (Figure 18c,d). Therefore, similar self-diffusional processes, where the self-diffusion has an activation barrier, the adsorbed H_2 molecules are self-diffusing translationally and are restricted by the pore walls of the adsorbents and/or adjacent H_2 molecules, are taking place in the investigated CDCs.

Because a different deconvolution procedure is applied in the case of H_2 adsorbed in sol-gel TiC-CDC, additional self-diffusing components can be distinguished compared to Mo_2C-CDC materials. Such multi-component analysis across a wide temporal range is possible by combining data from different measurement setups and instruments.

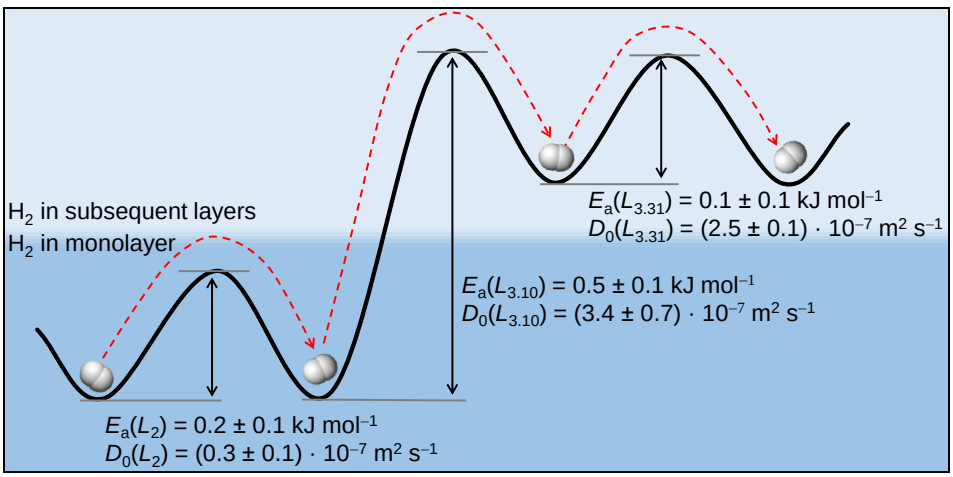

Figure 19. The proposed mechanism for the diffusion of adsorbed H_2 components (L_2, $L_{3.10}$, and $L_{3.31}$) between different adsorption sites in the monolayer and subsequent layers in sol-gel TiC-CDC described with activation energy values (E_a) and maximum diffusion coefficients (D_0).

At these conditions, three different self-diffusing components of H_2 adsorbed in the pores of sol-gel TiC-CDC can be distinguished – L_2, $L_{3.10}$, and $L_{3.31}$. In Figure 19, the proposed mechanism for the diffusion of adsorbed H_2 between different adsorption sites in the monolayer and subsequent layers of sol-gel TiC-CDC is visualised. The relatively low $E_a(L_2)$ indicates that H_2 adsorbed in the monolayer of sol-gel TiC-CDC can jump between the adsorption sites with almost no restriction. The differences in binding energies of H_2 adsorbed in the adsorption sites can be small and, thus, there could be many equally preferred adsorption sites [15,102]. As indicated by the low $D_0(L_2)$ value, the monolayer H_2 is strongly confined to the pore wall and is not able to diffuse towards the middle region of the pore. The strong confinement of the H_2 molecules adsorbed in the monolayer is explained by the type of interactions they experience. As explained in section 4.2, H_2 molecules adsorbed in the monolayer and in pores with $w < 10$ Å are strongly influenced by the adjacent pore walls. Also, the H_2 molecule interacts with

neighboring and subsequent H_2 molecules, therefore experiencing confinement from every direction [40,106]. H_2 can be strongly confined in mesopores in the monolayer as well. In the mesoporous silica KIT-6, the bulk-liquid and bulk-solid density of H_2 could be exceeded by a factor of almost 3 [103]. The formation of such a high-density adsorbed H_2 monolayer was proposed to be possible only on smooth adsorbent surfaces and at temperatures close to that of liquid H_2 (i.e., near 20 K) [103].

The H_2 component adsorbed in subsequent layers ($L_{3.10}$) is interpreted as the H_2 diffusing from a strongly confined monolayer to subsequent layers (Figure 19). Thus, that H_2 fraction has a slightly higher $E_a(L_{3.10})$ value. When this slightly higher activation barrier is exceeded, this H_2 component is relatively mobile as indicated by the relatively higher $D_0(L_{3.10})$ value. The H_2 adsorbed in subsequent layers does not experience as strong an interaction with the pore wall as in the monolayer because they are further separated. This means that the confinement arises mainly from steric hindrance and, therefore, the H_2 is more mobile than in the monolayer [106].

The H_2 component adsorbed in subsequent layers ($L_{3.31}$) is able to self-diffuse within the adsorbed H_2 regions with almost no restriction, as indicated by the low $E_a(L_{3.31})$ and high $D_0(L_{3.31})$ value (Figure 19). This can be explained by the differences in densities of different regions – the density of H_2 in subsequent adsorption layers is lower than in the primary monolayer closest to the pore wall, i.e., fewer intermolecular interactions are involved [107].

The observation of H_2 self-diffusion over multiple timescales, both in the case of Mo_2C-CDC materials and sol-gel TiC-CDC, could be important for designing catalyst support materials for polymer electrolyte membrane fuel cells and electrolysers, and adsorbent materials for H_2 storage. For example, the significant difference in densities and self-diffusivities and overly strong confinement of adsorbed H_2 could be disadvantageous for catalyst support materials as it can lead to slower transport of H_2 to and from active sites, limiting the rate of catalytic reactions [9,10,108]. For H_2 storage materials, the inhomogeneity in the adsorbed H_2 phase, particularly the strongly confined H_2, shows the formation of a high-density adsorbed H_2 phase, which is important for efficient H_2 storage [105].

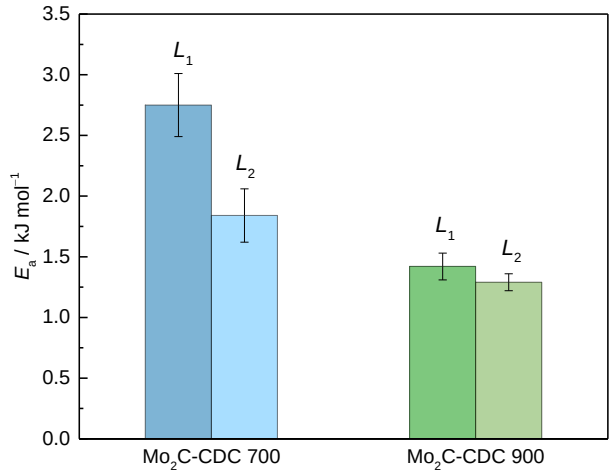

Figure 20. Activation energy values (E_a) of the two different self-diffusing components of H_2 (denoted as L_1 and L_2) adsorbed in Mo_2C-CDC 700 and Mo_2C-CDC 900 at moderate n_{H2} value.

The differences between the self-diffusion properties of adsorbed H_2 arising from the structure of the CDC become evident when comparing the E_a values under common experimental conditions in Mo_2C-CDC materials (Figure 20). When H_2 is adsorbed in Mo_2C-CDC 900 at moderate H_2 loading, the smoother pore walls (indicated by the lower volume and ratio of ultramicropores) have less effect on the diffusion hindrance of different components of adsorbed H_2 indicated by the similar E_a values of components L_1 and L_2 (Figure 20). Thus, although the self-diffusion of H_2 still occurs clearly in two different timescales in Mo_2C-CDC 900, the calculated E_a-s for these diffusion modes are nevertheless similar (Figure 20). The layering of adsorbed H_2 in the more corrugated pores of Mo_2C-CDC 700 is disrupted – some fraction of H_2 is adsorbed at an equivalent distance from the pore wall but with varying density profiles [107]. These regions of different H_2 densities cause different E_a values for H_2 self-diffusion components (L_1 and L_2) since E_a will be higher if the molecules restrict each other's movement in the regions with higher density. Overall, higher pore corrugation leads to a larger difference in the density of H_2 in different regions of the pore, which in turn leads to a larger difference in the E_a values of self-diffusing H_2 components. Thus, at moderate H_2 loading, the E_a of the slower and faster self-diffusion of H_2 in Mo_2C-CDC 700 are markedly more different from each other than the E_a of the slower and faster self-diffusion of H_2 in Mo_2C-CDC 900.

To compare the self-diffusion characteristic of H_2 adsorbed in the Mo_2C-CDC materials with sol-gel TiC-CDC, pore occupancy values need to be considered. Therefore, only the results for H_2 adsorbed at $n_{H2} = 31$ mmol g^{-1} are presented and analysed for sol-gel TiC-CDC (the results of the full series of the materials are analysed in Ref. [99]).

Table 8. Residence times (τ) of H_2 adsorbed in the monolayer in ps calculated for the Mo_2C-CDC materials with Singwi-Sjölander model and for the sol-gel TiC-CDC with Hall-Ross model.

T / K	Mo_2C-CDC 700	Mo_2C-CDC 800	Mo_2C-CDC 900	Sol-gel TiC-CDC
50	2.22±0.13[a]	2.55±0.16[a]	1.42±0.10[a]	1.21±0.02
80	2.71±0.05	3.41±0.07	1.66±0.02	0.98±0.02
100	2.29±0.04	2.05±0.02	1.76±0.02	0.89±0.01

[a] At these conditions, H_2 self-diffusion was observed in only one timescale. Thus, the results are not directly comparable with the rest of the results in the table.

The residence times (τ) are effectively dependent on the height of the plateau observed from $\Gamma(Q)$ vs Q when fitted with the Hall-Ross or Singwi-Sjölander model. Since the diffusion of H_2 adsorbed in the Mo_2C-CDC materials and sol-gel TiC-CDC are fitted with different translational jump-diffusion models, the differences in self-diffusivities are analysed based on the τ value.

The τ values of H_2 adsorbed in the monolayer in Mo_2C-CDCs are longer than in sol-gel TiC-CDC (Table 8). This indicates that Mo_2C-CDCs can confine the H_2 adsorbed in monolayer to a larger extent than sol-gel TiC-CDC. This could be related to a higher degree of graphenization, i.e., stacking of graphene-like layers, that was 2.76 graphenic layers per stack for sol-gel TiC-CDC and a larger mesopores volume in sol-gel TiC-CDC (V_{meso} = 1.88 $cm^3\ g^{-1}$) compared to the rest of the CDCs. The interlayer distance in graphenic non-graphitic carbon materials (3.3–3.7 Å) is too narrow for H_2 intercalation and, therefore, if the graphene-like layers are ordered in stacks of more than one layer, e.g., on average 2–3 graphene-like layers stacked in sol-gel TiC-CDC, important sites for H_2 adsorption are lost. In addition, the larger volume of mesopores in sol-gel TiC-CDC compared to Mo_2C-CDC promotes the faster self-diffusion of H_2 adsorbed in the monolayer and, therefore, shorter τ values of adsorbed H_2 compared to Mo_2C-CDCs.

6.2.3. H_2 self-diffusion at the highest applied pressure

At the highest H_2 loading and at 50 K, H_2 occupies in addition to micropores also the mesopores of the Mo_2C-CDC materials indicated by the pore occupancy value > 100%. The QENS of sol-gel TiC-CDC is not measured at a comparable H_2 loading, and thus, the QENS of H_2 adsorbed only in the Mo_2C-CDC materials is analysed further.

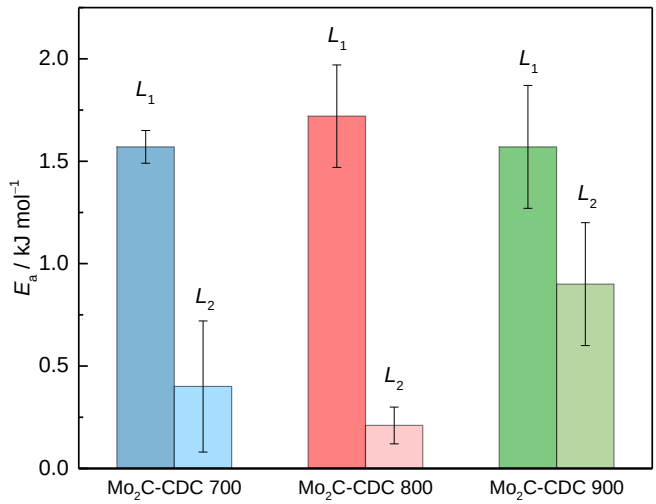

Figure 21. Activation energy (E_a) values of the two different self-diffusing components of H_2 (L_1 for the more restricted H_2 component and L_2 for the more mobile H_2 component) adsorbed in Mo_2C-CDC 700, Mo_2C-CDC 800, and Mo_2C-CDC 900 at the highest n_{H2}.

Even at the highest applied H_2 loading, there is still an adsorbed H_2 component for which motions are restricted, indicated by the relatively high E_a values of the H_2 component denoted with L_1 (Figure 21). Thus, even at the highest H_2 loading, there is a fraction of adsorbed H_2 for which self-diffusion is highly hindered. The fraction of H_2 with highly restricted self-diffusion is most likely the H_2 component adsorbed and confined in the supermicropores and in the concaves of the supermicropores, i.e., in ultramicropores.

The amplified confining effect on H_2 of the more corrugated pores, present in the case of Mo_2C-CDC 700, is not evident at the highest H_2 loading. This is indicated by the E_a values of the slower H_2 components (L_1), which are similar for all investigated CDCs (Figure 21). However, the E_a values of the faster moving component (L_2) show that at the highest H_2 loading, a considerable amount of H_2 is weakly interacting with the adsorbent and the adsorbed H_2 layers and, thus, H_2 is self-diffusing with virtually no restrictions at all. Therefore, the capability to analyse the faster H_2 component at increased H_2 loading pressure with the NEAT instrument set to the specific measurement parameters is limited. However, the very high mobility of some of the H_2 molecules is nevertheless evident from the considerably higher D values at the highest H_2 loading (Figure S9 in Ref. [98]).

6.3. Conclusions

The porous and graphenic structure of carbides derived from Mo_2C at 700 °C, 800 °C, and 900 °C (denoted as Mo_2C-CDC materials) and TiC, synthesized with sol-gel method (sol-gel TiC-CDC), at 950 °C is characterized with N_2, CO_2, H_2 (and Ar) adsorption analysis and with wide-angle X-ray scattering method,

respectively. The quasi-elastic neutron scattering (QENS) measurements were carried out at various H_2 loadings, i.e., various pore occupancy conditions. The Mo_2C-CDC materials and sol-gel TiC-CDC were measured with QENS instruments accessing different but overlapping timescales. This difference should be considered when comparing the self-diffusive properties of adsorbed H_2 molecules. The most important conclusions are summarized in Table 9.

Table 9. Overview of the main differences in the structure of Mo_2C-CDC materials and sol-gel TiC-CDC, the diffusion mechanisms and the influence of ultramicro-, micro-, and mesopores.

	Mo_2C-CDC materials	**Sol-gel TiC-CDC**
Porous structure	Mainly microporous. As synthesis temperature decreases, pore wall corrugation (microporosity) increases	Mainly mesoporous
Graphenic structure	Graphenic layers on average not in ordered stacks	Graphenic layers on average in stacks of ~2.76 layers
	H_2 self-diffusion in ultramicropores	
Mechanism	Translational	Rotational
Influence of structure	As pore wall corrugation increases, self-diffusion becomes more restricted	Very restricted – self-diffusion takes place between the opposing ultramicro-pore walls and/or between adsorption sites along the pore surface
	H_2 self-diffusion in micropores	
Mechanism	Translational self-diffusion over multiple timescales	
	The self-diffusion of H_2 is distinguished into **two** types – H_2 self-diffusing in the monolayer and self-diffusing in the middle region of the pore distinguished	The self-diffusion of H_2 is distinguished into **three** types – H_2 self-diffusing in the monolayer, diffusing to subsequent layers and self-diffusing in the middle region of the pore distinguished
Influence of structure	Higher pore wall corrugation results in a larger difference in the self-diffusive properties of H_2 compared to pores with smoother walls	Diffusion less restricted – if the graphene-like layers are ordered in stacks of more than one layer, important sites for H_2 adsorption are lost
	H_2 self-diffusion in micro- and mesopores	
Mechanism	Translational self-diffusion over multiple timescales	–
Influence of structure	A fraction of H_2 adsorbed with restricted self-diffusion (most likely in micropores). The amplified confining effect of the more corrugated pores not evident	

7. SUMMARY

The self-diffusion of H_2 adsorbed in carbide-derived carbons (CDCs) was investigated with quasi-elastic neutron scattering (QENS) method at different H_2 loading conditions and at temperatures from 30–100 K. The porous structure of the CDCs was characterised with N_2, CO_2, H_2 (and Ar) adsorption analysis and the graphenic structure with wide-angle X-ray scattering method. The CDCs derived from Mo_2C at the chlorination temperature of 700 °C, 800 °C, and 900 °C (denoted as Mo_2C-CDC 700, Mo_2C-CDC 800, and Mo_2C-CDC 900) had a relatively large micropores volume and high ratio of micropores. The micropore volume, i.e., the pore wall corrugation decreased as the chlorination temperature increased from 700 °C to 900 °C. The CDC derived from sol-gel TiC (sol-gel TiC-CDC) had a large mesopore volume, especially compared to the Mo_2C-CDC materials and a high stacking of graphene-like layers for a CDC material.

To investigate the influence of micro- and mesopores on the self-diffusive properties of adsorbed H_2, the QENS measurements were carried out at different H_2 loading conditions and at different fixed temperatures. That ensured varying levels of pore occupancy. At the lowest H_2 loading conditions in sol-gel TiC-CDC, H_2 was adsorbed in the smallest ultramicropores, while in Mo_2C-CDC materials, H_2 was likely adsorbed in all available ultramicropores and in some of the supermicropores. H_2 self-diffusion mechanism in sol-gel TiC-CDC was rotational, while in the Mo_2C-CDC materials it was translational. More corrugated pores (larger volume of ultramicropores) in Mo_2C-CDC 700 were able to confine adsorbed H_2 to a larger extent than pores with smoother walls in Mo_2C-CDC 900.

The H_2 adsorbed in the smallest ultramicropores in sol-gel TiC-CDC was very restricted and two self-diffusion mechanisms were possible: jumps between opposing pore walls and/or jumps along the pore walls. Such a strong H_2 confinement in the ultramicropores lays the foundation for the formation of a high-density adsorbed H_2 phase needed for H_2 storage. This could also be advantageous for H_2:D_2 separation. In contrast, the H_2 adsorbed in the larger ultramicropores of the Mo_2C-CDC materials was less restricted.

When H_2 was adsorbed in the micropores of the CDC materials, the self-diffusion of adsorbed H_2 occurred over multiple timescales. It is interpreted as the separable self-diffusion of the more restricted H_2 adsorbed closer to the pore wall in monolayer and the more mobile H_2 adsorbed in multilayers, i.e., in the middle region of the pore. The significant difference in self-diffusivities and very strong confinement of adsorbed H_2 could be disadvantageous for catalyst support materials as it can lead to slower transport of H_2 to active sites and away from the surface and thus, hinder catalytic performance. The differences in the self-diffusivities of adsorbed H_2 arise from the porous and graphenic structure of the CDC. Namely, Mo_2C-CDCs can confine the H_2 adsorbed in monolayer to a larger extent than sol-gel TiC-CDC. This is related to a higher level of graphene-like layer stacking, and larger volume of mesopores in sol-gel TiC-CDC compared to other CDCs.

The self-diffusion of H_2 adsorbed in Mo_2C-CDC materials was also investigated at the highest H_2 loading condition, where H_2 was adsorbed in all available micro- and mesopores. At these conditions, there was still a fraction of adsorbed H_2 for which the self-diffusion was restricted. That was most likely the H_2 component adsorbed and confined in the micropores. However, a considerable amount of H_2 was weakly interacting with the adsorbent and was self-diffusing with virtually no restrictions.

8. REFERENCES

(1) M. Mahmoud, L. A.; L. Rowlandson, J.; J. Fermin, D.; P. Ting, V.; Nayak, S. Porous Carbons: A Class of Nanomaterials for Efficient Adsorption-Based Hydrogen Storage. *RSC Applied Interfaces* **2025**, *2* (1), 25–55. https://doi.org/10.1039/D4LF00215F.

(2) Dastbaz, A.; Karimi-Sabet, J.; Amini, Y.; Moosavian, M. A. A Comprehensive Study on the Kinetics and Isotherms of D2/H2 Adsorptive Separation Using Pure and Composite Cu-BDC-NH2 MOFs at 77 K. *International Journal of Hydrogen Energy* **2024**, *61*, 893–900. https://doi.org/10.1016/j.ijhydene.2024.02.366.

(3) Jäger, R.; Kasatkin, P. E.; Härk, E.; Lust, E. Oxygen Reduction on Molybdenum Carbide Derived Micromesoporous Carbon Electrode in Alkaline Solution. *Electrochem. Commun.* **2013**, *35*, 97–99. https://doi.org/10.1016/j.elecom.2013.08.001.

(4) Naheed, L.; Koppel, M.; Paalo, M.; Alsabawi, K.; Lamb, K. E.; MacA. Gray, E.; Jänes, A.; Webb, C. J. Hydrogen Adsorption Properties of Carbide-Derived Carbons at Ambient Temperature and High Pressure. *International Journal of Hydrogen Energy* **2021**, *46* (29), 15761–15772. https://doi.org/10.1016/j.ijhydene.2021.02.109.

(5) Krkljus, I.; Steriotis, T.; Charalambopoulou, G.; Gotzias, A.; Hirscher, M. H2/D2 Adsorption and Desorption Studies on Carbon Molecular Sieves with Different Pore Structures. *Carbon* **2013**, *57*, 239–247. https://doi.org/10.1016/j.carbon.2013.01.069.

(6) Yang, D.; Rochat, S.; Krzystyniak, M.; Kulak, A.; Olivier, J.; Ting, V. P.; Tian, M. Investigation of the Dynamic Behaviour of H2 and D2 in a Kinetic Quantum Sieving System. *ACS Appl. Mater. Interfaces* **2024**, *16* (10), 12467–12478. https://doi.org/10.1021/acsami.3c17965.

(7) Contescu, C. I.; Zhang, H.; Olsen, R. J.; Mamontov, E.; Morris, J. R.; Gallego, N. C. Isotope Effect on Adsorbed Quantum Phases: Diffusion of H2 and D2 in Nanoporous Carbon. *Phys. Rev. Lett.* **2013**, *110* (23), 236102. https://doi.org/10.1103/PhysRevLett.110.236102.

(8) Petitpas, G.; Bénard, P.; Klebanoff, L. E.; Xiao, J.; Aceves, S. A Comparative Analysis of the Cryo-Compression and Cryo-Adsorption Hydrogen Storage Methods. *International Journal of Hydrogen Energy* **2014**, *39* (20), 10564–10584. https://doi.org/10.1016/j.ijhydene.2014.04.200.

(9) Li, J.; Ghoshal, S.; Liang, W.; Sougrati, M.-T.; Jaouen, F.; Halevi, B.; McKinney, S.; McCool, G.; Ma, C.; Yuan, X.; Ma, Z.-F.; Mukerjee, S.; Jia, Q. Structural and Mechanistic Basis for the High Activity of Fe–N–C Catalysts toward Oxygen Reduction. *Energy Environ. Sci.* **2016**, *9* (7), 2418–2432. https://doi.org/10.1039/C6EE01160H.

(10) Chenitz, R.; Kramm, U. I.; Lefèvre, M.; Glibin, V.; Zhang, G.; Sun, S.; Dodelet, J.-P. A Specific Demetalation of Fe–N4 Catalytic Sites in the Micropores of NC_Ar + NH3 Is at the Origin of the Initial Activity Loss of the Highly Active Fe/N/C Catalyst Used for the Reduction of Oxygen in PEM Fuel Cells. *Energy Environ. Sci.* **2018**, *11* (2), 365–382. https://doi.org/10.1039/C7EE02302B.

(11) Bahn, E.; Czakkel, O.; Nagy, B.; László, K.; Villar-Rodil, S.; Tascón, J. M. D.; Demmel, F.; Telling, M. T. F.; Fouquet, P. Diffusion of Molecular Hydrogen in Carbon Aerogel. *Carbon* **2016**, *98*, 572–581. https://doi.org/10.1016/j.carbon.2015.11.034.

(12) Bahn, E.; Hoyos Giraldo, L. A.; Kuznetsov, V.; Calvo-Almazán, I.; Zbiri, M.; Koza, M. M.; Hansen, T. C.; Henry, P. F.; Lapp, A.; Pouget, S.; Mesa, M.; Fouquet, P. Ultra-Fast Diffusion of Hydrogen in a Novel Mesoporous N-Doped Carbon. *Carbon* **2020**, *166*, 307–315. https://doi.org/10.1016/j.carbon.2020.05.004.

(13) Contescu, C. I.; Saha, D.; Gallego, N. C.; Mamontov, E.; Kolesnikov, A. I.; Bhat, V. V. Restricted Dynamics of Molecular Hydrogen Confined in Activated Carbon Nanopores. *Carbon* **2012**, *50* (3), 1071–1082. https://doi.org/10.1016/j.carbon.2011.10.016.
(14) Jung, M.; Park, J.; Muhammad, R.; Kim, J. Y.; Grzimek, V.; Russina, M.; Moon, H. R.; Park, J. T.; Oh, H. Elucidation of Diffusivity of Hydrogen Isotopes in Flexible MOFs by Quasi-Elastic Neutron Scattering. *Advanced Materials* **2021**, *33* (20), 2007412. https://doi.org/10.1002/adma.202007412.
(15) Haas, O.-E.; Simon, J. M.; Kjelstrup, S.; Ramstad, A. L.; Fouquet, P. Quasi-Elastic Neutron Scattering Investigation of the Hydrogen Surface Self-Diffusion on Polymer Electrolyte Membrane Fuel Cell Catalyst Support. *J. Phys. Chem. C* **2008**, *112* (8), 3121–3125. https://doi.org/10.1021/jp077715+.
(16) Pollock, R. A.; Her, J.-H.; Brown, C. M.; Liu, Y.; Dailly, A. Kinetic Trapping of D2 in MIL-53(Al) Observed Using Neutron Scattering. *J. Phys. Chem. C* **2014**, *118* (31), 18197–18206. https://doi.org/10.1021/jp504870n.
(17) Haas, O.-E.; Simon, J. M.; Kjelstrup, S. Surface Self-Diffusion and Mean Displacement of Hydrogen on Graphite and a PEM Fuel Cell Catalyst Support. *J. Phys. Chem. C* **2009**, *113* (47), 20281–20289. https://doi.org/10.1021/jp902491s.
(18) Kuznetsov, V.; Lohstroh, W.; Rogalla, D.; Becker, H.-W.; Strunskus, T.; Nefedov, A.; Kovacevic, E.; Traeger, F.; Fouquet, P. Neutron Spectroscopy Study of the Diffusivity of Hydrogen in MoS2. *Phys. Chem. Chem. Phys.* **2021**, *23* (13), 7961–7973. https://doi.org/10.1039/D0CP05136E.
(19) Telling, M. T. F. *A Practical Guide to Quasi-Elastic Neutron Scattering*; 2020.
(20) Hempelmann, R.; Hempelmann, R. *Quasielastic Neutron Scattering and Solid State Diffusion*; Oxford Series on Neutron Scattering in Condensed Matter; Oxford University Press: Oxford, New York, 2000.
(21) Bée, M. *Quasielastic Neutron Scattering: Principles and Applications in Solid State Chemistry, Biology, and Materials Science*; Adam Hilger: Bristol, England, 1988.
(22) Presser, V.; Heon, M.; Gogotsi, Y. Carbide-Derived Carbons – From Porous Networks to Nanotubes and Graphene. *Advanced Functional Materials* **2011**, *21* (5), 810–833. https://doi.org/10.1002/adfm.201002094.
(23) Gogotsi, Y.; Nikitin, A.; Ye, H.; Zhou, W.; Fischer, J. E.; Yi, B.; Foley, H. C.; Barsoum, M. W. Nanoporous Carbide-Derived Carbon with Tunable Pore Size. *Nat Mater* **2003**, *2* (9), 591–594. https://doi.org/10.1038/nmat957.
(24) Jänes, A.; Thomberg, T.; Kurig, H.; Lust, E. Nanoscale Fine-Tuning of Porosity of Carbide-Derived Carbon Prepared from Molybdenum Carbide. *Carbon* **2009**, *47* (1), 23–29. https://doi.org/10.1016/j.carbon.2008.07.010.
(25) Härmas, R.; Palm, R.; Härmas, M.; Pohl, M.; Kurig, H.; Tallo, I.; Tee, E.; Vaas, I.; Väli, R.; Romann, T.; Oll, O.; Kanarbik, R.; Liivand, K.; Eskusson, J.; Kruusma, J.; Thomberg, T.; Jänes, A.; Miidla, P.; Lust, E. Influence of Porosity Parameters and Electrolyte Chemical Composition on the Power Densities of Non-Aqueous and Ionic Liquid Based Supercapacitors. *Electrochim. Acta* **2018**, *283*, 931–948. https://doi.org/10/gd5nvj.
(26) Cui, Z.; Cong, Y.; Du, X.; Li, X.; Zhang, J.; Dong, Z.; Yuan, G.; Li, Y. Silicon Carbide-Derived Carbon Coated Graphitized Mesocarbon Microbead Composites for Anode of Lithium-Ion Battery. *Research & Reviews: Journal of Material Sciences* **2017**, *5* (3), 16–22. https://doi.org/10.4172/2321-6212.1000177.
(27) Gogotsi, Y. *Nanomaterials Handbook*; CRC Press: Boca Raton, 2006.
(28) Zhan, C.; Lian, C.; Zhang, Y.; Thompson, M. W.; Xie, Y.; Wu, J.; Kent, P. R. C.; Cummings, P. T.; Jiang, D.; Wesolowski, D. J. Computational Insights into Materials

and Interfaces for Capacitive Energy Storage. *Advanced Science* **2017**, *4* (7), 1700059. https://doi.org/10.1002/advs.201700059.
(29) Palm, R.; Härmas, R.; Härk, E.; Kent, B.; Kurig, H.; Koppel, M.; Russina, M.; Tallo, I.; Romann, T.; Mata, J.; Tuul, K.; Lust, E. Study of the Structural Curvature in Mo2C Derived Carbons with Contrast Matched Small-Angle Neutron Scattering. *Carbon* **2021**, *171*, 695–703. https://doi.org/10.1016/j.carbon.2020.09.070.
(30) Dou, X.; Hasa, I.; Saurel, D.; Vaalma, C.; Wu, L.; Buchholz, D.; Bresser, D.; Komaba, S.; Passerini, S. Hard Carbons for Sodium-Ion Batteries: Structure, Analysis, Sustainability, and Electrochemistry. *Materials Today* **2019**, No. 23, 87–104. https://doi.org/10.1016/j.mattod.2018.12.040.
(31) Härmas, R.; Palm, R.; Kurig, H.; Puusepp, L.; Pfaff, T.; Romann, T.; Aruväli, J.; Tallo, I.; Thomberg, T.; Jänes, A.; Lust, E. Carbide-Derived Carbons: WAXS and Raman Spectra for Detailed Structural Analysis. *C* **2021**, *7* (1), 29. https://doi.org/10.3390/c7010029.
(32) Jänes, A.; Thomberg, T.; Lust, E. Synthesis and Characterisation of Nanoporous Carbide-Derived Carbon by Chlorination of Vanadium Carbide. *Carbon* **2007**, *45* (14), 2717–2722. https://doi.org/10.1016/j.carbon.2007.09.041.
(33) Tallo, I.; Thomberg, T.; Kurig, H.; Kontturi, K.; Jänes, A.; Lust, E. Novel Micromesoporous Carbon Materials Synthesized from Tantalum Hafnium Carbide and Tungsten Titanium Carbide. *Carbon* **2014**, *67*, 607–616. https://doi.org/10.1016/j.carbon.2013.10.034.
(34) Thommes, M.; Kaneko, K.; Neimark, A. V.; Olivier, J. P.; Rodriguez-Reinoso, F.; Rouquerol, J.; Sing, K. S. W. Physisorption of Gases, with Special Reference to the Evaluation of Surface Area and Pore Size Distribution (IUPAC Technical Report). *Pure Appl. Chem.* **2015**, *87* (9–10), 1051–1069. https://doi.org/10.1515/pac-2014-1117.
(35) Thomberg, T.; Jänes, A.; Lust, E. Energy and Power Performance of Electrochemical Double-Layer Capacitors Based on Molybdenum Carbide Derived Carbon. *Electrochim. Acta* **2010**, *55* (9), 3138–3143. https://doi.org/10.1016/j.electacta.2010.01.075.
(36) Thomberg, T.; Jänes, A.; Lust, E. Energy and Power Performance of Vanadium Carbide Derived Carbon Electrode Materials for Supercapacitors. *J. Electroanal. Chem.* **2009**, *630* (1–2), 55–62. https://doi.org/10.1016/j.jelechem.2009.02.015.
(37) Härk, E.; Sepp, S.; Valk, P.; Vaarmets, K.; Nerut, J.; Jäger, R.; Lust, E. Impact of the Various Catalysts (Pt, Pt-Ru) Deposited onto Carbon Support to the Slow Oxygen Reduction Reaction Kinetics. *ECS Trans.* **2013**, *45* (21), 1–11. https://doi.org/10.1149/04521.0001ecst.
(38) Dyjak, S.; Kiciński, W.; Norek, M.; Dyjak, M.; Cudziło, S. Carbide-Derived Carbon Obtained *via* Bromination of Titanium Carbide: Comparative Analysis with Chlorination and Hydrogen Storage Studies. *Microporous and Mesoporous Materials* **2019**, *273*, 26–34. https://doi.org/10.1016/j.micromeso.2018.06.037.
(39) Masika, E.; Mokaya, R. Hydrogen Storage in High Surface Area Carbons with Identical Surface Areas but Different Pore Sizes: Direct Demonstration of the Effects of Pore Size. *J. Phys. Chem. C* **2012**, *116* (49), 25734–25740. https://doi.org/10.1021/jp3100365.
(40) Konstantakou, M.; Gotzias, A.; Kainourgiakis, M.; Stubos, A.; Steriotis, T. GCMC Simulations of Gas Adsorption in Carbon Pore Structures; 2011. https://doi.org/10.5772/15988.
(41) Gogotsi, Y.; Dash, R. K.; Yushin, G.; Yildirim, T.; Laudisio, G.; Fischer, J. E. Tailoring of Nanoscale Porosity in Carbide-Derived Carbons for Hydrogen Storage. *Journal of the American Chemical Society* **2005**, *127* (46), 16006–16007.

(42) Gogotsi, Y.; Portet, C.; Osswald, S.; Simmons, J. M.; Yildirim, T.; Laudisio, G.; Fischer, J. E. Importance of Pore Size in High-Pressure Hydrogen Storage by Porous Carbons. *Int. J. Hydrogen Energy* **2009**, *34* (15), 6314–6319. https://doi.org/10.1016/j.ijhydene.2009.05.073.
(43) Laudisio, G.; Dash, R. K.; Singer, J. P.; Yushin, G.; Gogotsi, Y.; Fischer, J. E. Carbide-Derived Carbons: A Comparative Study of Porosity Based on Small-Angle Scattering and Adsorption Isotherms. *Langmuir* **2006**, *22* (21), 8945–8950. https://doi.org/10.1021/la060860e.
(44) Tallo, I.; Thomberg, T.; Kontturi, K.; Jänes, A.; Lust, E. Nanostructured Carbide-Derived Carbon Synthesized by Chlorination of Tungsten Carbide. *Carbon* **2011**, *49* (13), 4427–4433. https://doi.org/10.1016/j.carbon.2011.06.033.
(45) Pohl, M.; Kurig, H.; Tallo, I.; Jänes, A.; Lust, E. Novel Sol-Gel Synthesis Route of Carbide-Derived Carbon Composites for Very High Power Density Supercapacitors. *Chem. Eng. J.* **2017**, *320*, 576–587. https://doi.org/10.1016/j.cej.2017.03.081.
(46) Kurig, H.; Russina, M.; Tallo, I.; Siebenbürger, M.; Romann, T.; Lust, E. The Suitability of Infinite Slit-Shaped Pore Model to Describe the Pores in Highly Porous Carbon Materials. *Carbon* **2016**, *100*, 617–624. https://doi.org/10.1016/j.carbon.2016.01.061.
(47) Raman, V.; Bahl, O. P.; Dhawan, U. Synthesis of Silicon Carbide through the Sol-Gel Process from Different Precursors. *J Mater Sci* **1995**, *30* (10), 2686–2693. https://doi.org/10.1007/BF00362153.
(48) Tallo, I.; Thomberg, T.; Jänes, A.; Lust, E. Replacing Chlorine with Hydrogen Chloride as a Possible Reactant for Synthesis of Titanium Carbide Derived Carbon Powders for High-Technology Devices. *IOP Conf. Ser.: Mater. Sci. Eng.* **2013**, *49* (1), 012018. https://doi.org/10.1088/1757-899X/49/1/012018.
(49) Brinker, C. J.; Scherer, G. W. *Sol-Gel Science: The Physics and Chemistry of Sol-Gel Processing*, 1st ed.; 1990.
(50) Mhadhbi, M. Titanium Carbide: Synthesis, Properties and Applications. *BEN* **2020**, *2* (2), 1–11. https://doi.org/10.36937/ben.2021.002.001.
(51) Jagiello, J.; Thommes, M. Comparison of DFT Characterization Methods Based on N2, Ar, CO2, and H2 Adsorption Applied to Carbons with Various Pore Size Distributions. *Carbon* **2004**, *42* (7), 1227–1232. https://doi.org/10.1016/j.carbon.2004.01.022.
(52) Schlumberger, C.; Thommes, M. Characterization of Hierarchically Ordered Porous Materials by Physisorption and Mercury Porosimetry – A Tutorial Review. *Advanced Materials Interfaces* **2021**, *8* (4), 2002181. https://doi.org/10.1002/admi.202002181.
(53) Jagiello, J.; Kenvin, J.; Celzard, A.; Fierro, V. Enhanced Resolution of Ultra Micropore Size Determination of Biochars and Activated Carbons by Dual Gas Analysis Using N2 and CO2 with 2D-NLDFT Adsorption Models. *Carbon* **2019**, *144*, 206–215. https://doi.org/10.1016/j.carbon.2018.12.028.
(54) Jagiello, J.; Betz, W. Characterization of Pore Structure of Carbon Molecular Sieves Using DFT Analysis of Ar and H2 Adsorption Data. *Microporous and Mesoporous Materials* **2008**, *108* (1), 117–122. https://doi.org/10.1016/j.micromeso.2007.03.035.
(55) Brunauer, S.; Emmett, P. H.; Teller, E. Adsorption of Gases in Multimolecular Layers. *J Am Chem Soc* **1938**, *60* (2), 309–319. https://doi.org/10.1021/ja01269a023.
(56) Lowell, S.; Shields, J. E.; Thomas, M. A.; Thommes, M. *Characterization of Porous Solids and Powders: Surface Area, Pore Size and Density*; Particle Technology Series; Kluwer Academic Publishers: Dordrecht, the Netherlands, 2004.

(57) Cychosz, K. A.; Thommes, M. Progress in the Physisorption Characterization of Nanoporous Gas Storage Materials. *Engineering* **2018**, *4* (4), 559–566. https://doi.org/10.1016/j.eng.2018.06.001.
(58) Landers, J.; Gor, G. Y.; Neimark, A. V. Density Functional Theory Methods for Characterization of Porous Materials. *Colloids and Surfaces A: Physicochemical and Engineering Aspects* **2013**, *437*, 3–32. https://doi.org/10.1016/j.colsurfa.2013.01.007.
(59) Shi, K.; Santiso, E. E.; Gubbins, K. E. Current Advances in Characterization of Nano-Porous Materials: Pore Size Distribution and Surface Area. In *Porous Materials: Theory and Its Application for Environmental Remediation*; Moreno-Piraján, J. C., Giraldo-Gutierrez, L., Gómez-Granados, F., Eds.; Springer International Publishing: Cham, 2021; pp 315–340. https://doi.org/10.1007/978-3-030-65991-2_12.
(60) Jagiello, J.; Olivier, J. P. A Simple Two-Dimensional NLDFT Model of Gas Adsorption in Finite Carbon Pores. Application to Pore Structure Analysis. *J. Phys. Chem. C* **2009**, *113* (45), 19382–19385. https://doi.org/10.1021/jp9082147.
(61) Jagiello, J.; Olivier, J. P. Carbon Slit Pore Model Incorporating Surface Energetical Heterogeneity and Geometrical Corrugation. *Adsorption* **2013**, *19* (2–4), 777–783. https://doi.org/10.1007/s10450-013-9517-4.
(62) Jagiello, J. Stable Numerical Solution of the Adsorption Integral Equation Using Splines. *Langmuir* **1994**, *10* (8), 2778–2785. https://doi.org/10.1021/la00020a045.
(63) Bragg, W. H.; Bragg, W. L. The Reflection of X-Rays by Crystals. *Proc. R. Soc. Lond. A* **1913**, *88* (605), 428–438. https://doi.org/10.1098/rspa.1913.0040.
(64) Pfaff, T.; Simmermacher, M.; Smarsly, B. M. CarbX : A Program for the Evaluation of Wide-Angle X-Ray Scattering Data of Non-Graphitic Carbons. *J Appl Crystallogr* **2018**, *51* (1), 219–229. https://doi.org/10.1107/S1600576718000195.
(65) Faber, K.; Badaczewski, F.; Ruland, W.; Smarsly, B. M. Investigation of the Microstructure of Disordered, Non-Graphitic Carbons by an Advanced Analysis Method for Wide-Angle X-Ray Scattering. *Zeitschrift für anorganische und allgemeine Chemie* **2014**, *640* (15), 3107–3117. https://doi.org/10.1002/zaac.201400210.
(66) Ruland, W.; Smarsly, B. X-Ray Scattering of Non-Graphitic Carbon: An Improved Method of Evaluation. *J Appl Cryst, J Appl Crystallogr* **2002**, *35* (5), 624–633. https://doi.org/10.1107/S0021889802011007.
(67) Vonk, C. G. The Small-Angle Scattering of Distorted Lamellar Structures. *J Appl Cryst* **1978**, *11* (5), 541–546. https://doi.org/10.1107/S0021889878013837.
(68) Atkins, P.; De Paula, J. *Atkins' Physical Chemistry*, 8th ed.; W. H. Freeman and Company: New York, NY, USA, 2006.
(69) Kunowsky, M.; Marco-Lózar, J. P.; Linares-Solano, A. Material Demands for Storage Technologies in a Hydrogen Economy. *Journal of Renewable Energy* **2013**, *2013* (1), 878329. https://doi.org/10.1155/2013/878329.
(70) Darkrim Lamari, F.; Weinberger, B.; Kunowsky, M.; Levesque, D. Material Design Using Molecular Modeling for Hydrogen Storage. *AIChE Journal* **2009**, *55* (2), 538–547. https://doi.org/10.1002/aic.11670.
(71) Beenakker, J. J. M.; Borman, V. D.; Krylov, S. Yu. Molecular Transport in Subnanometer Pores: Zero-Point Energy, Reduced Dimensionality and Quantum Sieving. *Chemical Physics Letters* **1995**, *232* (4), 379–382. https://doi.org/10.1016/0009-2614(94)01372-3.
(72) Cabria, I. Comparison of Theoretical Methods of the Hydrogen Storage Capacities of Nanoporous Carbons. *International Journal of Hydrogen Energy* **2020**, *46*. https://doi.org/10.1016/j.ijhydene.2020.04.212.

(73) Karki, S.; Chakraborty, S. N. A Monte Carlo Simulation Study of Hydrogen Adsorption in Slit-Shaped Pores. *Microporous and Mesoporous Materials* **2021**, *317*, 110970. https://doi.org/10.1016/j.micromeso.2021.110970.
(74) Rogacka, J.; Firlej, L.; Kuchta, B. Modeling of Low Temperature Adsorption of Hydrogen in Carbon Nanopores. *J Mol Model* **2017**, *23* (1), 20. https://doi.org/10.1007/s00894-016-3202-y.
(75) Peng, L.; Morris, J. R. Prediction of Hydrogen Adsorption Properties in Expanded Graphite Model and in Nanoporous Carbon. *J. Phys. Chem. C* **2010**, *114* (36), 15522–15529. https://doi.org/10.1021/jp104595m.
(76) Tian, M.; Lennox, M. J.; O'Malley, A. J.; Porter, A. J.; Krüner, B.; Rudić, S.; Mays, T. J.; Düren, T.; Presser, V.; Terry, L. R.; Rols, S.; Fang, Y.; Dong, Z.; Rochat, S.; Ting, V. P. Effect of Pore Geometry on Ultra-Densified Hydrogen in Microporous Carbons. *Carbon* **2021**, *173*, 968–979. https://doi.org/10.1016/j.carbon.2020.11.063.
(77) Härmas, R.; Palm, R.; Russina, M.; Kurig, H.; Grzimek, V.; Härk, E.; Koppel, M.; Tallo, I.; Paalo, M.; Oll, O.; Embs, J.; Lust, E. Transport Properties of H2 Confined in Carbide-Derived Carbons with Different Pore Shapes and Sizes. *Carbon* **2019**, *155*, 122–128. https://doi.org/10.1016/j.carbon.2019.08.041.
(78) Jagiello, J.; Olivier, J. P. 2D-NLDFT Adsorption Models for Carbon Slit-Shaped Pores with Surface Energetical Heterogeneity and Geometrical Corrugation. *Carbon* **2013**, *55*, 70–80. https://doi.org/10.1016/j.carbon.2012.12.011.
(79) Yang, Y.; Brown, C. M.; Zhao, C.; Chaffee, A. L.; Nick, B.; Zhao, D.; Webley, P. A.; Schalch, J.; Simmons, J. M.; Liu, Y.; Her, J.-H.; Buckley, C. E.; Sheppard, D. A. Micro-Channel Development and Hydrogen Adsorption Properties in Templated Microporous Carbons Containing Platinum Nanoparticles. *Carbon* **2011**, *49* (4), 1305–1317. https://doi.org/10.1016/j.carbon.2010.11.050.
(80) Baruchel, J., Hodeau, J.-L., Lehmann, M. S., Regnard, J.-R., Schlenker, C. *Neutron and Synchrotron Radiation for Condensed Matter Studies*; Springer: Berlin, Heidelberg, 1994.
(81) Pynn, R. *Neutron Scattering – a Primer*; Los Alamos Science, 1990.
(82) Bee, M. *Quasielastic Neutron Scattering*; Adam Hilger: United Kingdom, 1988.
(83) Georgiev, P. A.; Ross, D. K.; De Monte, A.; Montaretto-Marullo, U.; Edwards, R. A. H.; Ramirez-Cuesta, A. J.; Adams, M. A.; Colognesi, D. In Situ Inelastic Neutron Scattering Studies of the Rotational and Translational Dynamics of Molecular Hydrogen Adsorbed in Single-Wall Carbon Nanotubes (SWNTs). *Carbon* **2005**, *43* (5), 895–906. https://doi.org/10.1016/j.carbon.2004.11.006.
(84) Olsen, R. J.; Firlej, L.; Kuchta, B.; Taub, H.; Pfeifer, P.; Wexler, C. Sub-Nanometer Characterization of Activated Carbon by Inelastic Neutron Scattering. *Carbon* **2011**, *49* (5), 1663–1671. https://doi.org/10.1016/j.carbon.2010.12.051.
(85) Bahadur, J.; Contescu, C. I.; Ramirez-Cuesta, A. J.; Mamontov, E.; Gallego, N. C.; Cheng, Y.; Daemen, L. L.; Melnichenko, Y. B. Properties of Immobile Hydrogen Confined in Microporous Carbon. *Carbon* **2017**, *117*, 383–392. https://doi.org/10.1016/j.carbon.2017.03.007.
(86) Sears, V. F. Neutron Scattering Lengths and Cross Sections. *Neutron News* **1992**, *3* (3), 26–37. https://doi.org/10.1080/10448639208218770.
(87) Billings, B.; Gray, D. *American Institute of Physics Handbook*; McGraw-Hill, 1972.
(88) Hall, P. L.; Ross, D. K. Incoherent Neutron Scattering Functions for Random Jump Diffusion in Bounded and Infinite Media. *Molecular Physics* **1981**, *42* (3), 673–682. https://doi.org/10.1080/00268978100100521.

(89) Singwi, K. S.; Sjölander, A. Diffusive Motions in Water and Cold Neutron Scattering. *Phys. Rev.* **1960**, *119* (3), 863–871. https://doi.org/10.1103/PhysRev.119.863.
(90) Atkins, P. W.; De Paula, J. *Physical Chemistry*, 9th ed.; Oxford University Press: Oxford, 2010.
(91) Russina, M.; Guenther, G.; Grzimek, V.; Gainov, R.; Schlegel, M.-C.; Drescher, L.; Kaulich, T.; Graf, W.; Urban, B.; Daske, A.; Grotjahn, K.; Hellhammer, R.; Buchert, G.; Kutz, H.; Rossa, L.; Sauer, O.-P.; Fromme, M.; Wallacher, D.; Kiefer, K.; Klemke, B.; Grimm, N.; Gerischer, S.; Tsapatsaris, N.; Rolfs, K. Upgrade Project NEAT′2016 at Helmholtz Zentrum Berlin – What Can Be Done on the Medium Power Neutron Source. *Physica B: Condensed Matter* **2018**, *551*, 506–511. https://doi.org/10.1016/j.physb.2017.12.026.
(92) Palm, R.; Kurig, H.; Koppel, M.; Oll, O.; Grzimek, V.; Lust, E.; Russina, M. The Diffusion of H2 Adsorbed in Three Porous Carbons Investigated with in Situ Quasi-Elastic Neutron Scattering Method, 2022. https://doi.org/10.23673/re-324.
(93) Carlile, C. J.; Adams, M. A. The Design of the IRIS Inelastic Neutron Spectrometer and Improvements to Its Analysers. *Physica B: Condensed Matter* **1992**, *182* (4), 431–440. https://doi.org/10.1016/0921-4526(92)90047-V.
(94) Le, M. D.; Guidi, T.; Bewley, R.; Stewart, J. R.; Schooneveld, E. M.; Raspino, D.; Pooley, D. E.; Boxall, J.; Gascoyne, K. F.; Rhodes, N. J.; Moorby, S. R.; Templeman, D. J.; Afford, L. C.; Waller, S. P.; Zacek, D.; Shaw, R. C. R. Upgrade of the MARI Spectrometer at ISIS. *Nuclear Instruments and Methods in Physics Research Section A: Accelerators, Spectrometers, Detectors and Associated Equipment* **2023**, *1056*, 168646. https://doi.org/10.1016/j.nima.2023.168646.
(95) Palm, R.; Strandson, A. L.; Mansson, M.; Koppel, M.; Telling, M.; Silverwood, I.; Härmas, R. Mobility of H2 Adsorbed in Multilayers in Sol-Gel Method TiC Derived Carbon, 2021. https://doi.org/10.5286/ISIS.E.RB2010339.
(96) Palm, R.; Strandson, A. L.; Le, M. D.; Koppel, M.; Härmas, R. Presence of Multilayer H2 Adsorption in Micro- and Mesoporous Carbon, 2020. https://doi.org/10.5286/ISIS.E.RB2010603.
(97) Arnold, O.; Bilheux, J. C.; Borreguero, J. M.; Buts, A.; Campbell, S. I.; Chapon, L.; Doucet, M.; Draper, N.; Ferraz Leal, R.; Gigg, M. A.; Lynch, V. E.; Markvardsen, A.; Mikkelson, D. J.; Mikkelson, R. L.; Miller, R.; Palmen, K.; Parker, P.; Passos, G.; Perring, T. G.; Peterson, P. F.; Ren, S.; Reuter, M. A.; Savici, A. T.; Taylor, J. W.; Taylor, R. J.; Tolchenov, R.; Zhou, W.; Zikovsky, J. Mantid—Data Analysis and Visualization Package for Neutron Scattering and μ SR Experiments. *Nuclear Instruments and Methods in Physics Research. Section A, Accelerators, Spectrometers, Detectors and Associated Equipment* **2014**, *764* (C). https://doi.org/10.1016/j.nima.2014.07.029.
(98) Koppel, M.; Palm, R.; Härmas, R.; Russina, M.; Grzimek, V.; Jagiello, J.; Paalo, M.; Kurig, H.; Månsson, M.; Oll, O.; Lust, E. Pore Wall Corrugation Effect on the Dynamics of Adsorbed H2 Studied by in Situ Quasi-Elastic Neutron Scattering: Observation of Two Timescaled Diffusion. *Carbon* **2022**, *197*, 359–367. https://doi. org/10.1016/j.carbon.2022.06.061.
(99) Koppel, M.; Palm, R.; Härmas, R.; Telling, M.; Le, M. D.; Guidi, T.; Tuul, K.; Paalo, M.; Kalder, L.; Jagiello, J.; Romann, T.; Aruväli, J.; Månsson, M.; Lust, E. Disentangling the Self-Diffusional Dynamics of H2 Adsorbed in Micro- and Mesoporous Carbide-Derived Carbon by Wide Temporal Range Quasi-Elastic Neutron Scattering. *Carbon* **2024**, *219*, 118799. https://doi.org/10.1016/j.carbon.2024.118799.

(100) O'Reilly, D. E.; Peterson, E. M. Self-diffusion of Liquid Hydrogen and Deuterium. *J. Chem. Phys.* **1977**, *66* (3), 934–937. https://doi.org/10.1063/1.434001.
(101) Koppel, M.; Palm, R.; Härmas, R.; Russina, M.; Matsubara, N.; Månsson, M.; Grzimek, V.; Paalo, M.; Aruväli, J.; Romann, T.; Oll, O.; Lust, E. In Situ Observation of Pressure Modulated Reversible Structural Changes in the Graphitic Domains of Carbide-Derived Carbons. *Carbon* **2021**, *174*, 190–200. https://doi.org/10.1016/j.carbon.2020.12.025.
(102) Arellano, J. S.; Molina, L. M.; Rubio, A.; Alonso, J. A. Density Functional Study of Adsorption of Molecular Hydrogen on Graphene Layers. *J. Chem. Phys.* **2000**, *112* (18), 8114–8119. https://doi.org/10.1063/1.481411.
(103) Balderas-Xicohténcatl, R.; Lin, H.-H.; Lurz, C.; Daemen, L.; Cheng, Y.; Cychosz Struckhoff, K.; Guillet-Nicolas, R.; Schütz, G.; Heine, T.; Ramirez-Cuesta, A. J.; Thommes, M.; Hirscher, M. Formation of a Super-Dense Hydrogen Monolayer on Mesoporous Silica. *Nat. Chem.* **2022**, *14* (11), 1319–1324. https://doi.org/10.1038/s41557-022-01019-7.
(104) Kowalczyk, P.; Tanaka, H.; Hołyst, R.; Kaneko, K.; Ohmori, T.; Miyamoto, J. Storage of Hydrogen at 303 K in Graphite Slitlike Pores from Grand Canonical Monte Carlo Simulation. *J. Phys. Chem. B* **2005**, *109* (36), 17174–17183. https://doi.org/10.1021/jp0529063.
(105) Gallego, N. C.; He, L.; Saha, D.; Contescu, C. I.; Melnichenko, Y. B. Hydrogen Confinement in Carbon Nanopores: Extreme Densification at Ambient Temperature. *J. Am. Chem. Soc.* **2011**, *133* (35), 13794–13797. https://doi.org/10.1021/ja202432x.
(106) Cabria, I.; López, M. J.; Alonso, J. A. Density Functional Study of Molecular Hydrogen Coverage on Carbon Nanotubes. *Computational Materials Science* **2006**, *35* (3), 238–242. https://doi.org/10.1016/j.commatsci.2004.10.008.
(107) Jagiello, J.; Kenvin, J.; Ania, C. O.; Parra, J. B.; Celzard, A.; Fierro, V. Exploiting the Adsorption of Simple Gases O2 and H2 with Minimal Quadrupole Moments for the Dual Gas Characterization of Nanoporous Carbons Using 2D-NLDFT Models. *Carbon* **2020**, *160*, 164–175. https://doi.org/10.1016/j.carbon.2020.01.013.
(108) Mouarrawis, V.; Plessius, R.; van der Vlugt, J. I.; Reek, J. N. H. Confinement Effects in Catalysis Using Well-Defined Materials and Cages. *Front. Chem.* **2018**, *6*. https://doi.org/10.3389/fchem.2018.00623.

9. SUMMARY IN ESTONIAN

Karbiididest sünteesitud süsinikes adsorbeerunud H_2 difusiooni uurimine kvaasielastse neutronhajumise meetodiga

Selles töös uuriti karbiididest sünteesitud süsinikes (CDC) adsorbeerunud H_2 difusiooni kvaasielastse neutronhajumise (QENS) meetodiga erinevatel H_2 laadimisrõhkudel ja temperatuuridel 30–100 K. CDC-de poorne struktuur määrati N_2, CO_2, H_2 (ja Ar) adsorptsiooni meetodiga ja grafeeniline struktuur määrati laianurgalise röntgenhajumise meetodiga. CDC-d sünteesiti Mo_2C-st kloreerimistemperatuuridel 700 °C, 800 °C ja 900 °C (vastavalt Mo_2C-CDC 700, Mo_2C-CDC 800 ja Mo_2C-CDC 900) ja nendel materjalidel oli võrdlemisi suur mikropooride (poori laius < 20 Å) ruumala ja osakaal. Mikropooride ruumala (pooriseina karedus) väheneb kui materjali kloreerimistemperatuuri tõsta 700 °C-lt 900 °C-ni. CDC-l, mis oli saadud sool-geel meetodiga sünteesitud TiC-st (sol-gel TiC-CDC), oli võrreldes teiste CDC-dega suur mesopooride (poori laius 20–500 Å) ruumala ja võrdlemisi palju grafeeni-laadseid kihte ühes virnas (umbes 2–3 grafeeni-laadset kihti).

Selleks et uurida mikro- ja mesopooride mõju adsorbeerunud H_2 difusioonile, viidi läbi QENS mõõtmine erinevatel H_2 laadimisrõhkudel ja erinevatel temperatuuridel, st erinevatel pooride täitumismääradel. Kõige madalamal laadimisrõhul täitis H_2 ~1% sol-gel TiC-CDC pooridest, st H_2 oli adsorbeerunud kõige väiksemates ultramikropoorides (poori laius < 7 Å). Mo_2C-CDC materjalides oli H_2 adsorbeerunud ~6% pooridest, seega kõikides ultramikropoorides ja väiksemates supermikropoorides (poori laius 7–20 Å). H_2, mis oli adsorbeerunud sol-gel TiC-CDC väikseimates ultramikropoorides, difundeerus rotatsiooniliselt, aga H_2, mis oli adsorbeerunud Mo_2C-CDC-de ultra- ja supermikropoorides, difundeerus translatoorselt. Karedamate seintega poorid (suurem ultramikropooride ruumala) materjalis Mo_2C-CDC 700 hoidsid adsorbeerunud H_2 tugevamalt kinni kui siledamate seintega poorid materjalis Mo_2C-CDC 900.

Sol-gel TiC-CDC materjali kõige väiksemates ultramikropoorides adsorbeerunud H_2 difusioon oli väga takistatud ning kaks H_2 rotatsioonilise difusiooni mehhanismi olid võimalikud: H_2 molekulid „hüppasid“ poori seinte vahel ja/või pikki poori seina. H_2 molekulide nii piiratud liikumine nendes poorides näitab, et ultramikropoorid hoiavad H_2 nii tugevalt kinni, et H_2 saab adsorbeeruda väga suure tihedusega. See on vajalik näiteks H_2 salvestamiseks ning H_2 ja D_2 (H_2 isotoobi) eraldamiseks. Seevastu Mo_2C-CDC materjalides, kus H_2 oli adsorbeerunud kõikides ultra- ja supermikropoorides, oli H_2 liikuvam.

Keskmisel laadimisrõhul oli H_2 adsorbeerunud valdavalt CDC-de mikropoorides ja H_2 difusioon toimus mitmes erinevas kiiruspiirkonnas. Näitkes, üks H_2 komponent oli tugevamalt adsorbeerunud poori seinale kõige lähemal esimesestes kihtides ja teine H_2 komponent oli liikuvam ja adsorbeerunud järgmistes H_2 kihtides poori keskel. Selge erinevus adsorbeerunud H_2 komponentide difusiooni kiirustes võib olla kahjulik näiteks katalüsaatormaterjalides, kus on oluline, et H_2 difusioon aktiivtsentritesse ja nendest ära oleks võimalikult kiire ning poorides

oleva H_2 tihedus võimalikult ühtlane. Erinevused adsorbeerunud H_2 komponentide difusioonis olid tingitud CDC-de poorsest ja grafeenilisest struktuurist. Mo_2C-CDC materjalid hoidsid adsobeerunud H_2 tugevamalt kinni kui sol-gel TiC-CDC. See võis olla põhjustatud sellest, et sol-gel TiC-CDCs oli rohkem grafeeni-laadseid kihte ühes virnas ja suurem mesopooride ruumala kui teistes CDC materjalides.

Mo_2C-CDC materjalides uuriti H_2 difusiooni ka kõige kõrgemal H_2 laadimisrõhul, kus H_2 oli adsorbeerunud kõikides mikro- ja mesopoorides. Kuigi H_2 oli adsorbeerunud kõikides poorides, oli siiski ühe H_2 komponendi liikumine väga piiratud. See H_2 komponent oli adsorbeerunud mikropoorides. Samas oli ka suur hulk adsorbeerunud H_2, mille difusioon toimus peaaegu piiramatult. See H_2 komponent oli adsorbeerunud juba mesopoorides.

10. ACKNOWLEDGEMENTS

Firstly, I would like to thank my supervisors Dr. Rasmus Palm, Dr. Riinu Härmas, and prof. Enn Lust for their support, trust and guidance throughout my studies. I greatly admire Dr. Rasmus Palm's efficiency and ability to approach every scientific problem open-mindedly, Dr. Riinu Härmas' attention to detail and diligence, and prof. Enn Lust's vast knowledge base and the ability to always see the bigger picture.

Secondly, I would like to thank the co-authors of the publications in this thesis for synthesizing the materials (Dr. Maarja Paalo, M.Sc. Kenneth Tuul), conducting the experiments (Dr. Veronika Grzimek, Dr. Margarita Russina, Dr. Heisi Kurig, Dr. Ove Oll, Dr. Mark Telling, Dr. Manh Duc Le, Dr. Tatiana Guidi, M.Sc. Jaan Aruväli, Dr. Tavo Romann), and analyzing and/or interpreting the data (Dr. Nami Matsubara, Dr. Jacek Jagiello, M.Sc. Laura Kalder, Dr. Martin Månsson). I am very grateful to Dr. Mark Telling from ISIS neutron and muon source, who measured the neutron scattering data on IRIS and who guided me through the data analysis with extreme patience. I would also like to express my gratitude to prof. Jörg Pieper and Dr. Maksym Golub from the Institute of Physics of the University of Tartu, whose feedback and valuable insights helped me understand the neutron scattering data in greater detail.

Thirdly, I would like to thank my colleagues from room 5034 and from the chair of physical chemistry for making the work environment not only productive, but also overall enjoyable. A special thanks goes to Dr. Ove Oll, prof. Jaak Nerut, and Dr. Thomas Thomberg for the valuable discussions. Their questions during the seminars helped me understand my work better and guided me to think about it from a different angle. In addition, I would like to thank Marta, Laura, Heigo, Karl Ander, Kenneth, and Egert for all the help and support as well as for their interesting insights – scientific and not-so-scientific ones.

Finally, I am very grateful to my family and friends for their unconditional support – I feel very lucky to have you all in my life. I especially want to thank Patrick, whose constant encouragement helped me through some of the most challenging moments of my studies.

This research was financially supported by the Estonian Research Council grants PSG935 and PRG676, by the EU through the European Regional Development Fund under project TK141 (2014-2020.4.01.15-0011), by Graduate School of Functional materials and technologies receiving funding from the European Regional Development Fund, by the Estonian Ministry of Education and Research (TK210), by the Estonian Ministry of Education and Research through funding from SLTKT16432T "Estonian participation in designing, construction and application of the ESS 1.09.2015–31.08.2023)", by the projects ÕÜF1 "Increasing the knowledge intensity of Ida-Viru entrepreneurship" cofunded by the European Union, by the project 101159716 "Increasing Excellence in Utilizing X-ray Research and Neutron Scattering Techniques at the University of Tartu",

and through the Estonian Research Agency TEM-TA81 project “Development and Testing of Novel Green Energy Technology Complex Systems and Innovative Vital Devices”.

11. PUBLICATIONS

CURRICULUM VITAE

Name: Miriam Koppel
Date of birth: January 19, 1997
Citizenship: Estonian
Contact: Institute of Chemistry, University of Tartu, Ravila 14a, 50411, Tartu, Estonia
E-mail: miriam.koppel@ut.ee

Education:

2021–...	University of Tartu, Chemistry, PhD student
2019–2021	University of Tartu, Materials Science and Technology, MSc, *cum laude*
2016–2019	University of Tartu, Physics, Chemistry and Materials Science, BSc

Professional Employment:

2024–2025	Baltic Innovation Agency, consultant
2023–...	AS BIT, editor of chemistry text- and workbooks
2021–...	University of Tartu, junior research fellow of Physical Chemistry
2018–2021	University of Tartu, chemist

Scientific publications:

1. **M. Koppel**, R. Palm, R. Härmas, M. T. F. Telling, M. D. Le, T. Guidi, K. Tuul, M. Paalo, E. Lust, Restricted dynamics and para-ortho conversion of H_2 adsorbed in micro- and mesoporous carbide-derived carbon: a quasi- and inelastic neutron scattering study, Journal of Physical Chemistry C, 2025, 129, 4789−4799. DOI: 10.1021/acs.jpcc.4c08582
2. M. Härmas, A. Olgo, A. Adamson, **M. Koppel**, A. Jänes (2024). Optimizing Synthesis Temperature for Lignin-Derived Hard Carbon Anode for High Cycling Capacity in Sodium-Ion Batteries. Journal of The Electrochemical Society, 171, 2, 020539. DOI: 10.1149/1945-7111/ad28d7.
3. P. Teppor, R. Jäger, **M. Koppel**, O. Volobujeva, R. Palm, M. Månsson, E. Härk, Z. Kochovski, J. Aruväli, K. Kooser, S. Granroth, T. Käämbre, J. Nerut, E. Lust, (2024). Unlocking the porosity of Fe–N–C catalysts using hydroxyapatite as a hard template en route to eco-friendly high-performance AEMFCs. Journal of Power Sources, 591, 233816. DOI: 10.1016/j.jpowsour.2023.233816.
4. **M. Koppel**, R. Palm, R. Härmas, M. Telling, M. D. Le, T. Guidi, K. Tuul, M. Paalo, L. Kalder, J. Jagiello, T. Romann, J. Aruväli, M. Månsson, E. Lust (2024). Disentangling the self-diffusional dynamics of H_2 adsorbed in micro- and mesoporous carbide-derived carbon by wide temporal range quasi-elastic neutron scattering. Carbon, 219, ARTN 118799. DOI: 10.1016/j.carbon.2024.118799.

5. H. Bulgarin, T. Thomberg, A. Lust, J. Nerut, **M. Koppel**, T. Romann, R. Palm, M. Mansson, M. Vana, H. Junninen, M. Külaviir, P. Paiste, K. Kirsimäe, M. Punapart, L. Viru, A. Merits, E. Lust (2024). Enhanced and copper concentration dependent virucidal effect against SARS-CoV-2 of electrospun poly(vinylidene difluoride) filter materials. iScience, 27 (6), ARTN 109835. DOI: 10.1016/j.isci.2024.109835.
6. H. Q. V. Nguyen, J. Nerut, H. Kasuk, M. Härmas, P. Valk, T. Romann, **M. Koppel**, P. Teppor, J. Aruväli, O. Korjus, O. Volobujeva, E. Lust (2023). Optimisation of the ethylene glycol reduction method for the synthesis of platinum-ceria-carbon materials as catalysts for the methanol oxidation reaction. Journal of Solid State Electrochemistry. DOI: 10.1007/s10008-022-05326-4.
7. T. Thomberg, H. Bulgarin, A. Lust, J. Nerut, **M. Koppel**, T. Romann, R. Palm, M. Månsson, N. M. Flores March, H. Junninen, M. Külaviir, P. Paiste, K. Kirsimäe, M. Punapart, L. Viru, A. Merits, E. Lust (2023). The anti SARS-CoV-2 activity of nanofibrous filter materials activated with metal clusters. Atmospheric Environment: X, 17, 100212. DOI: 10.1016/j.aeaoa.2023.100212.
8. M. Golub, **M. Koppel**, P. Pikma, B. Frick, J. Pieper (2023). Dynamics–Function Correlation in Photosystem II: Molecular Dynamics in Solution. Crystals, 13, 10, 1441. DOI: 10.3390/cryst13101441.
9. E. Möller, R. Palm, K. Tuul, M. Härmas, **M. Koppel**, J. Aruväli, M. Külaviir, E. Lust (2023). Peat-Derived $ZnCl_2$-Activated Ultramicroporous Carbon Materials for Hydrogen Adsorption. Nanomaterials, 13, 21, 2883. DOI: 10.3390/nano13212883.
10. T. Thomberg, P. Ramah, A. Lust, J. Nerut, **M. Koppel**, T. Romann, R. Palm, M. Månsson, N. M. Flores March, H. Junninen, M. Külaviir, P. Paiste, K. Kirsimäe, M. Punapart, L. Viru, A. Merits, E. Lust (2022). Preparation of nanofibrous materials activated with metal clusters for active and long-lasting air filters. Separation and Purification Technology, 288, ARTN 120697. DOI: 10.1016/j.seppur.2022.120697.
11. H. Q. V. Nguyen, J. Nerut, H. Kasuk, V. Grozovski, T. Thomberg, I. Tallo, R. Palm, **M. Koppel**, T. Romann, R. Härmas, J. Aruväli, M. Külaviir, E. Lust (2022). Oxygen Reduction Reaction on Chromium Carbide-Derived Carbons. Russian Journal of Electrochemistry, 58, 9, 781−797. DOI: 10.1134/S1023193522090130.
12. **M. Koppel**, R. Palm, R. Härmas, M. Russina, V. Grzimek, J. Jagiello, M. Paalo, H. Kurig, M. Månsson, O. Oll, E. Lust (2022). Pore wall corrugation effect on the dynamics of adsorbed H2 studied by in situ quasi-elastic neutron scattering: Observation of two timescaled diffusion. Carbon, 197, 359−367. DOI: 10.1016/j.carbon.2022.06.061.
13. R. Palm, R. Härmas, E. Härk, B. Kent, H. Kurig, **M. Koppel**, M. Russina, I. Tallo, T. Romann, J. Mata, K. Tuul, E. Lust (2021). Study of the structural curvature in Mo2C derived carbons with contrast matched small-angle neutron scattering. Carbon, 171, 695−703. DOI: 10.1016/j.carbon.2020.09.070.
14. **M. Koppel**, R. Palm, R. Härmas, M. Russina, N. Matsubara, M. Månsson, V. Grzimek, M. Paalo, J. Aruväli, T. Romann, O. Oll, E. Lust (2021). In Situ

Observation of Pressure Modulated Reversible Structural Changes in the Graphitic Domains of Carbide-Derived Carbons. Carbon. 174, 190−200. DOI: 10.1016/j.carbon.2020.12.025.
15. L. Naheed, **M. Koppel**, M. Paalo, K. Alsabawi, K. E. Lamb, E. MacA. Gray, A. Jänes, C. J. Webb (2021). Hydrogen adsorption properties of carbide-derived carbons at ambient temperature and high pressure. International Journal of Hydrogen Energy, 46, 29, 15761−15772. DOI: 10.1016/j.ijhydene.2021.02.109.
16. A. Adamson, R. Väli, M. Paalo, J. Aruväli, **M. Koppel**, R. Palm, E. Härk, J. Nerut, T. Romann, E. Lust, A. Jänes (2020). Peat-derived hard carbon electrodes with superior capacity for sodium-ion batteries. RSC Advances, 10, 34, 20145−20154. DOI: 10.1039/d0ra03212c.
17. M. Härmas, R. Palm, T. Thomberg, R. Härmas, **M. Koppel**, M. Paalo, I. Tallo, T. Romann, A. Jänes, E. Lust (2020). Hydrothermal and peat-derived carbons as electrode materials for high-efficient electrical double-layer capacitors. Journal of Applied Electrochemistry, 50, 15−32. DOI: 10.1007/s10800-019-01364-5.
18. R. Härmas, R. Palm, M. Russina, H. Kurig, V. Grzimek, E. Härk, **M. Koppel**, I. Tallo, M. Paalo, O. Oll, J. P. Embs, E. Lust (2019). Transport properties of H_2 confined in carbide-derived carbons with different pore shapes and sizes. Carbon, 155, 122−128. DOI: 10.1016/j.carbon.2019.08.041.

ELULOOKIRJELDUS

Nimi: Miriam Koppel
Sünniaeg: 19. jaanuar 1997
Kodakondsus: Eesti
Kontakt: Tartu Ülikooli keemia instituut, Ravila 14a, 50411, Tartu, Eesti
E-post: miriam.koppel@ut.ee

Haridus:

2021–...	Tartu Ülikool, Keemia, doktoriõpe
2019–2021	Tartu Ülikool, Materjaliteadus ja tehnoloogia, MSc, *cum laude*
2016–2019	Tartu Ülikool, Füüsika, keemia ja materjaliteadus, BSc

Töökogemus:

2024–2025	Balti Innovatsiooni Agentuur, konsultant
2023–...	AS BIT, keemia õppematerjalide toimetaja
2021–...	Tartu Ülikool, füüsikalise keemia nooremteadur
2018–2021	Tartu Ülikool, keemik

Teaduspublikatsioonid:

1. **M. Koppel**, R. Palm, R. Härmas, M. T. F. Telling, M. D. Le, T. Guidi, K. Tuul, M. Paalo, E. Lust, Restricted dynamics and para-ortho conversion of H_2 adsorbed in micro- and mesoporous carbide-derived carbon: a quasi- and inelastic neutron scattering study, Journal of Physical Chemistry C, 2025, 129, 4789−4799. DOI: 10.1021/acs.jpcc.4c08582
2. M. Härmas, A. Olgo, A. Adamson, **M. Koppel**, A. Jänes (2024). Optimizing Synthesis Temperature for Lignin-Derived Hard Carbon Anode for High Cycling Capacity in Sodium-Ion Batteries. Journal of The Electrochemical Society, 171, 2, 020539. DOI: 10.1149/1945-7111/ad28d7.
3. P. Teppor, R. Jäger, **M. Koppel**, O. Volobujeva, R. Palm, M. Månsson, E. Härk, Z. Kochovski, J. Aruväli, K. Kooser, S. Granroth, T. Käämbre, J. Nerut, E. Lust, (2024). Unlocking the porosity of Fe–N–C catalysts using hydroxyapatite as a hard template en route to eco-friendly high-performance AEMFCs. Journal of Power Sources, 591, 233816. DOI: 10.1016/j.jpowsour.2023.233816.
4. **M. Koppel**, R. Palm, R. Härmas, M. Telling, M. D. Le, T. Guidi, K. Tuul, M. Paalo, L. Kalder, J. Jagiello, T. Romann, J. Aruväli, M. Månsson, E. Lust (2024). Disentangling the self-diffusional dynamics of H_2 adsorbed in micro- and mesoporous carbide-derived carbon by wide temporal range quasi-elastic neutron scattering. Carbon, 219, ARTN 118799. DOI: 10.1016/j.carbon.2024.118799.
5. H. Bulgarin, T. Thomberg, A. Lust, J. Nerut, **M. Koppel**, T. Romann, R. Palm, M. Mansson, M. Vana, H. Junninen, M. Külaviir, P. Paiste, K. Kirsimäe, M. Punapart, L. Viru, A. Merits, E. Lust (2024). Enhanced and copper concentration dependent virucidal effect against SARS-CoV-2 of electrospun

poly(vinylidene difluoride) filter materials. iScience, 27 (6), ARTN 109835. DOI: 10.1016/j.isci.2024.109835.

6. H. Q. V. Nguyen, J. Nerut, H. Kasuk, M. Härmas, P. Valk, T. Romann, **M. Koppel**, P. Teppor, J. Aruväli, O. Korjus, O. Volobujeva, E. Lust (2023). Optimisation of the ethylene glycol reduction method for the synthesis of platinum-ceria-carbon materials as catalysts for the methanol oxidation reaction. Journal of Solid State Electrochemistry. DOI: 10.1007/s10008-022-05326-4.
7. T. Thomberg, H. Bulgarin, A. Lust, J. Nerut, **M. Koppel**, T. Romann, R. Palm, M. Månsson, N. M. Flores March, H. Junninen, M. Külaviir, P. Paiste, K. Kirsimäe, M. Punapart, L. Viru, A. Merits, E. Lust (2023). The anti SARS-CoV-2 activity of nanofibrous filter materials activated with metal clusters. Atmospheric Environment: X, 17, 100212. DOI: 10.1016/j.aeaoa.2023.100212.
8. M. Golub, **M. Koppel**, P. Pikma, B. Frick, J. Pieper (2023). Dynamics–Function Correlation in Photosystem II: Molecular Dynamics in Solution. Crystals, 13, 10, 1441. DOI: 10.3390/cryst13101441.
9. E. Möller, R. Palm, K. Tuul, M. Härmas, **M. Koppel**, J. Aruväli, M. Külaviir, E. Lust (2023). Peat-Derived $ZnCl_2$-Activated Ultramicroporous Carbon Materials for Hydrogen Adsorption. Nanomaterials, 13, 21, 2883. DOI: 10.3390/nano13212883.
10. T. Thomberg, P. Ramah, A. Lust, J. Nerut, **M. Koppel**, T. Romann, R. Palm, M. Månsson, N. M. Flores March, H. Junninen, M. Külaviir, P. Paiste, K. Kirsimäe, M. Punapart, L. Viru, A. Merits, E. Lust (2022). Preparation of nanofibrous materials activated with metal clusters for active and long-lasting air filters. Separation and Purification Technology, 288, ARTN 120697. DOI: 10.1016/j.seppur.2022.120697.
11. H. Q. V. Nguyen, J. Nerut, H. Kasuk, V. Grozovski, T. Thomberg, I. Tallo, R. Palm, **M. Koppel**, T. Romann, R. Härmas, J. Aruväli, M. Külaviir, E. Lust (2022). Oxygen Reduction Reaction on Chromium Carbide-Derived Carbons. Russian Journal of Electrochemistry, 58, 9, 781−797. DOI: 10.1134/S1023193522090130.
12. **M. Koppel**, R. Palm, R. Härmas, M. Russina, V. Grzimek, J. Jagiello, M. Paalo, H. Kurig, M. Månsson, O. Oll, E. Lust (2022). Pore wall corrugation effect on the dynamics of adsorbed H2 studied by in situ quasi-elastic neutron scattering: Observation of two timescaled diffusion. Carbon, 197, 359−367. DOI: 10.1016/j.carbon.2022.06.061.
13. R. Palm, R. Härmas, E. Härk, B. Kent, H. Kurig, **M. Koppel**, M. Russina, I. Tallo, T. Romann, J. Mata, K. Tuul, E. Lust (2021). Study of the structural curvature in Mo2C derived carbons with contrast matched small-angle neutron scattering. Carbon, 171, 695−703. DOI: 10.1016/j.carbon.2020.09.070.
14. **M. Koppel**, R. Palm, R. Härmas, M. Russina, N. Matsubara, M. Månsson, V. Grzimek, M. Paalo, J. Aruväli, T. Romann, O. Oll, E. Lust (2021). In Situ Observation of Pressure Modulated Reversible Structural Changes in the Graphitic Domains of Carbide-Derived Carbons. Carbon. 174, 190−200. DOI: 10.1016/j.carbon.2020.12.025.

15. L. Naheed, **M. Koppel**, M. Paalo, K. Alsabawi, K. E. Lamb, E. MacA. Gray, A. Jänes, C. J. Webb (2021). Hydrogen adsorption properties of carbide-derived carbons at ambient temperature and high pressure. International Journal of Hydrogen Energy, 46, 29, 15761−15772. DOI: 10.1016/j.ijhydene.2021.02.109.
16. A. Adamson, R. Väli, M. Paalo, J. Aruväli, **M. Koppel**, R. Palm, E. Härk, J. Nerut, T. Romann, E. Lust, A. Jänes (2020). Peat-derived hard carbon electrodes with superior capacity for sodium-ion batteries. RSC Advances, 10, 34, 20145−20154. DOI: 10.1039/d0ra03212c.
17. M. Härmas, R. Palm, T. Thomberg, R. Härmas, **M. Koppel**, M. Paalo, I. Tallo, T. Romann, A. Jänes, E. Lust (2020). Hydrothermal and peat-derived carbons as electrode materials for high-efficient electrical double-layer capacitors. Journal of Applied Electrochemistry, 50, 15−32. DOI: 10.1007/s10800-019-01364-5.
18. R. Härmas, R. Palm, M. Russina, H. Kurig, V. Grzimek, E. Härk, **M. Koppel**, I. Tallo, M. Paalo, O. Oll, J. P. Embs, E. Lust (2019). Transport properties of H_2 confined in carbide-derived carbons with different pore shapes and sizes. Carbon, 155, 122−128. DOI: 10.1016/j.carbon.2019.08.041.

DISSERTATIONES CHIMICAE UNIVERSITATIS TARTUENSIS

1. **Toomas Tamm.** Quantum-chemical simulation of solvent effects. Tartu, 1993, 110 p.
2. **Peeter Burk.** Theoretical study of gas-phase acid-base equilibria. Tartu, 1994, 96 p.
3. **Victor Lobanov.** Quantitative structure-property relationships in large descriptor spaces. Tartu, 1995, 135 p.
4. **Vahur Mäemets.** The ^{17}O and ^{1}H nuclear magnetic resonance study of H_2O in individual solvents and its charged clusters in aqueous solutions of electrolytes. Tartu, 1997, 140 p.
5. **Andrus Metsala.** Microcanonical rate constant in nonequilibrium distribution of vibrational energy and in restricted intramolecular vibrational energy redistribution on the basis of slater's theory of unimolecular reactions. Tartu, 1997, 150 p.
6. **Uko Maran.** Quantum-mechanical study of potential energy surfaces in different environments. Tartu, 1997, 137 p.
7. **Alar Jänes.** Adsorption of organic compounds on antimony, bismuth and cadmium electrodes. Tartu, 1998, 219 p.
8. **Kaido Tammeveski.** Oxygen electroreduction on thin platinum films and the electrochemical detection of superoxide anion. Tartu, 1998, 139 p.
9. **Ivo Leito.** Studies of Brønsted acid-base equilibria in water and non-aqueous media. Tartu, 1998, 101 p.
10. **Jaan Leis.** Conformational dynamics and equilibria in amides. Tartu, 1998, 131 p.
11. **Toonika Rinken.** The modelling of amperometric biosensors based on oxidoreductases. Tartu, 2000, 108 p.
12. **Dmitri Panov.** Partially solvated Grignard reagents. Tartu, 2000, 64 p.
13. **Kaja Orupõld.** Treatment and analysis of phenolic wastewater with microorganisms. Tartu, 2000, 123 p.
14. **Jüri Ivask.** Ion Chromatographic determination of major anions and cations in polar ice core. Tartu, 2000, 85 p.
15. **Lauri Vares.** Stereoselective Synthesis of Tetrahydrofuran and Tetrahydropyran Derivatives by Use of Asymmetric Horner-Wadsworth-Emmons and Ring Closure Reactions. Tartu, 2000, 184 p.
16. **Martin Lepiku.** Kinetic aspects of dopamine D_2 receptor interactions with specific ligands. Tartu, 2000, 81 p.
17. **Katrin Sak.** Some aspects of ligand specificity of P2Y receptors. Tartu, 2000, 106 p.
18. **Vello Pällin.** The role of solvation in the formation of iotsitch complexes. Tartu, 2001, 95 p.
19. **Katrin Kollist.** Interactions between polycyclic aromatic compounds and humic substances. Tartu, 2001, 93 p.

20. **Ivar Koppel.** Quantum chemical study of acidity of strong and superstrong Brønsted acids. Tartu, 2001, 104 p.
21. **Viljar Pihl.** The study of the substituent and solvent effects on the acidity of OH and CH acids. Tartu, 2001, 132 p.
22. **Natalia Palm.** Specification of the minimum, sufficient and significant set of descriptors for general description of solvent effects. Tartu, 2001, 134 p.
23. **Sulev Sild.** QSPR/QSAR approaches for complex molecular systems. Tartu, 2001, 134 p.
24. **Ruslan Petrukhin.** Industrial applications of the quantitative structure-property relationships. Tartu, 2001, 162 p.
25. **Boris V. Rogovoy.** Synthesis of (benzotriazolyl)carboximidamides and their application in relations with *N*- and *S*-nucleophyles. Tartu, 2002, 84 p.
26. **Koit Herodes.** Solvent effects on UV-vis absorption spectra of some solvatochromic substances in binary solvent mixtures: the preferential solvation model. Tartu, 2002, 102 p.
27. **Anti Perkson.** Synthesis and characterisation of nanostructured carbon. Tartu, 2002, 152 p.
28. **Ivari Kaljurand.** Self-consistent acidity scales of neutral and cationic Brønsted acids in acetonitrile and tetrahydrofuran. Tartu, 2003, 108 p.
29. **Karmen Lust.** Adsorption of anions on bismuth single crystal electrodes. Tartu, 2003, 128 p.
30. **Mare Piirsalu.** Substituent, temperature and solvent effects on the alkaline hydrolysis of substituted phenyl and alkyl esters of benzoic acid. Tartu, 2003, 156 p.
31. **Meeri Sassian.** Reactions of partially solvated Grignard reagents. Tartu, 2003, 78 p.
32. **Tarmo Tamm.** Quantum chemical modelling of polypyrrole. Tartu, 2003. 100 p.
33. **Erik Teinemaa.** The environmental fate of the particulate matter and organic pollutants from an oil shale power plant. Tartu, 2003. 102 p.
34. **Jaana Tammiku-Taul.** Quantum chemical study of the properties of Grignard reagents. Tartu, 2003. 120 p.
35. **Andre Lomaka.** Biomedical applications of predictive computational chemistry. Tartu, 2003. 132 p.
36. **Kostyantyn Kirichenko.** Benzotriazole – Mediated Carbon–Carbon Bond Formation. Tartu, 2003. 132 p.
37. **Gunnar Nurk.** Adsorption kinetics of some organic compounds on bismuth single crystal electrodes. Tartu, 2003, 170 p.
38. **Mati Arulepp.** Electrochemical characteristics of porous carbon materials and electrical double layer capacitors. Tartu, 2003, 196 p.
39. **Dan Cornel Fara.** QSPR modeling of complexation and distribution of organic compounds. Tartu, 2004, 126 p.
40. **Riina Mahlapuu.** Signalling of galanin and amyloid precursor protein through adenylate cyclase. Tartu, 2004, 124 p.

41. **Mihkel Kerikmäe.** Some luminescent materials for dosimetric applications and physical research. Tartu, 2004, 143 p.
42. **Jaanus Kruusma.** Determination of some important trace metal ions in human blood. Tartu, 2004, 115 p.
43. **Urmas Johanson.** Investigations of the electrochemical properties of polypyrrole modified electrodes. Tartu, 2004, 91 p.
44. **Kaido Sillar.** Computational study of the acid sites in zeolite ZSM-5. Tartu, 2004, 80 p.
45. **Aldo Oras.** Kinetic aspects of dATPαS interaction with $P2Y_1$ receptor. Tartu, 2004, 75 p.
46. **Erik Mölder.** Measurement of the oxygen mass transfer through the air-water interface. Tartu, 2005, 73 p.
47. **Thomas Thomberg.** The kinetics of electroreduction of peroxodisulfate anion on cadmium (0001) single crystal electrode. Tartu, 2005, 95 p.
48. **Olavi Loog.** Aspects of condensations of carbonyl compounds and their imine analogues. Tartu, 2005, 83 p.
49. **Siim Salmar.** Effect of ultrasound on ester hydrolysis in aqueous ethanol. Tartu, 2006, 73 p.
50. **Ain Uustare.** Modulation of signal transduction of heptahelical receptors by other receptors and G proteins. Tartu, 2006, 121 p.
51. **Sergei Yurchenko.** Determination of some carcinogenic contaminants in food. Tartu, 2006, 143 p.
52. **Kaido Tämm.** QSPR modeling of some properties of organic compounds. Tartu, 2006, 67 p.
53. **Olga Tšubrik.** New methods in the synthesis of multisubstituted hydrazines. Tartu. 2006, 183 p.
54. **Lilli Sooväli.** Spectrophotometric measurements and their uncertainty in chemical analysis and dissociation constant measurements. Tartu, 2006, 125 p.
55. **Eve Koort.** Uncertainty estimation of potentiometrically measured ph and pK_a values. Tartu, 2006, 139 p.
56. **Sergei Kopanchuk.** Regulation of ligand binding to melanocortin receptor subtypes. Tartu, 2006, 119 p.
57. **Silvar Kallip.** Surface structure of some bismuth and antimony single crystal electrodes. Tartu, 2006, 107 p.
58. **Kristjan Saal.** Surface silanization and its application in biomolecule coupling. Tartu, 2006, 77 p.
59. **Tanel Tätte.** High viscosity $Sn(OBu)_4$ oligomeric concentrates and their applications in technology. Tartu, 2006, 91 p.
60. **Dimitar Atanasov Dobchev**. Robust QSAR methods for the prediction of properties from molecular structure. Tartu, 2006, 118 p.
61. **Hannes Hagu**. Impact of ultrasound on hydrophobic interactions in solutions. Tartu, 2007, 81 p.
62. **Rutha Jäger.** Electroreduction of peroxodisulfate anion on bismuth electrodes. Tartu, 2007, 142 p.

63. **Kaido Viht.** Immobilizable bisubstrate-analogue inhibitors of basophilic protein kinases: development and application in biosensors. Tartu, 2007, 88 p.
64. **Eva-Ingrid Rõõm.** Acid-base equilibria in nonpolar media. Tartu, 2007, 156 p.
65. **Sven Tamp.** DFT study of the cesium cation containing complexes relevant to the cesium cation binding by the humic acids. Tartu, 2007, 102 p.
66. **Jaak Nerut.** Electroreduction of hexacyanoferrate(III) anion on Cadmium (0001) single crystal electrode. Tartu, 2007, 180 p.
67. **Lauri Jalukse.** Measurement uncertainty estimation in amperometric dissolved oxygen concentration measurement. Tartu, 2007, 112 p.
68. **Aime Lust.** Charge state of dopants and ordered clusters formation in CaF_2:Mn and CaF_2:Eu luminophors. Tartu, 2007, 100 p.
69. **Iiris Kahn**. Quantitative Structure-Activity Relationships of environmentally relevant properties. Tartu, 2007, 98 p.
70. **Mari Reinik.** Nitrates, nitrites, N-nitrosamines and polycyclic aromatic hydrocarbons in food: analytical methods, occurrence and dietary intake. Tartu, 2007, 172 p.
71. **Heili Kasuk.** Thermodynamic parameters and adsorption kinetics of organic compounds forming the compact adsorption layer at Bi single crystal electrodes. Tartu, 2007, 212 p.
72. **Erki Enkvist.** Synthesis of adenosine-peptide conjugates for biological applications. Tartu, 2007, 114 p.
73. **Svetoslav Hristov Slavov**. Biomedical applications of the QSAR approach. Tartu, 2007, 146 p.
74. **Eneli Härk.** Electroreduction of complex cations on electrochemically polished Bi(*hkl*) single crystal electrodes. Tartu, 2008, 158 p.
75. **Priit Möller.** Electrochemical characteristics of some cathodes for medium temperature solid oxide fuel cells, synthesized by solid state reaction technique. Tartu, 2008, 90 p.
76. **Signe Viggor.** Impact of biochemical parameters of genetically different pseudomonads at the degradation of phenolic compounds. Tartu, 2008, 122 p.
77. **Ave Sarapuu.** Electrochemical reduction of oxygen on quinone-modified carbon electrodes and on thin films of platinum and gold. Tartu, 2008, 134 p.
78. **Agnes Kütt.** Studies of acid-base equilibria in non-aqueous media. Tartu, 2008, 198 p.
79. **Rouvim Kadis.** Evaluation of measurement uncertainty in analytical chemistry: related concepts and some points of misinterpretation. Tartu, 2008, 118 p.
80. **Valter Reedo.** Elaboration of IVB group metal oxide structures and their possible applications. Tartu, 2008, 98 p.
81. **Aleksei Kuznetsov.** Allosteric effects in reactions catalyzed by the cAMP-dependent protein kinase catalytic subunit. Tartu, 2009, 133 p.

82. **Aleksei Bredihhin.** Use of mono- and polyanions in the synthesis of multisubstituted hydrazine derivatives. Tartu, 2009, 105 p.
83. **Anu Ploom.** Quantitative structure-reactivity analysis in organosilicon chemistry. Tartu, 2009, 99 p.
84. **Argo Vonk.** Determination of adenosine A_{2A}- and dopamine D_1 receptor-specific modulation of adenylate cyclase activity in rat striatum. Tartu, 2009, 129 p.
85. **Indrek Kivi.** Synthesis and electrochemical characterization of porous cathode materials for intermediate temperature solid oxide fuel cells. Tartu, 2009, 177 p.
86. **Jaanus Eskusson.** Synthesis and characterisation of diamond-like carbon thin films prepared by pulsed laser deposition method. Tartu, 2009, 117 p.
87. **Marko Lätt.** Carbide derived microporous carbon and electrical double layer capacitors. Tartu, 2009, 107 p.
88. **Vladimir Stepanov.** Slow conformational changes in dopamine transporter interaction with its ligands. Tartu, 2009, 103 p.
89. **Aleksander Trummal.** Computational Study of Structural and Solvent Effects on Acidities of Some Brønsted Acids. Tartu, 2009, 103 p.
90. **Eerold Vellemäe.** Applications of mischmetal in organic synthesis. Tartu, 2009, 93 p.
91. **Sven Parkel.** Ligand binding to 5-HT_{1A} receptors and its regulation by Mg^{2+} and Mn^{2+}. Tartu, 2010, 99 p.
92. **Signe Vahur.** Expanding the possibilities of ATR-FT-IR spectroscopy in determination of inorganic pigments. Tartu, 2010, 184 p.
93. **Tavo Romann**. Preparation and surface modification of bismuth thin film, porous, and microelectrodes. Tartu, 2010, 155 p.
94. **Nadežda Aleksejeva.** Electrocatalytic reduction of oxygen on carbon nanotube-based nanocomposite materials. Tartu, 2010, 147 p.
95. **Marko Kullapere.** Electrochemical properties of glassy carbon, nickel and gold electrodes modified with aryl groups. Tartu, 2010, 233 p.
96. **Liis Siinor.** Adsorption kinetics of ions at Bi single crystal planes from aqueous electrolyte solutions and room-temperature ionic liquids. Tartu, 2010, 101 p.
97. **Angela Vaasa.** Development of fluorescence-based kinetic and binding assays for characterization of protein kinases and their inhibitors. Tartu 2010, 101 p.
98. **Indrek Tulp.** Multivariate analysis of chemical and biological properties. Tartu 2010, 105 p.
99. **Aare Selberg.** Evaluation of environmental quality in Northern Estonia by the analysis of leachate. Tartu 2010, 117 p.
100. **Darja Lavõgina.** Development of protein kinase inhibitors based on adenosine analogue-oligoarginine conjugates. Tartu 2010, 248 p.
101. **Laura Herm.** Biochemistry of dopamine D_2 receptors and its association with motivated behaviour. Tartu 2010, 156 p.

102. **Terje Raudsepp.** Influence of dopant anions on the electrochemical properties of polypyrrole films. Tartu 2010, 112 p.
103. **Margus Marandi.** Electroformation of Polypyrrole Films: *In-situ* AFM and STM Study. Tartu 2011, 116 p.
104. **Kairi Kivirand.** Diamine oxidase-based biosensors: construction and working principles. Tartu, 2011, 140 p.
105. **Anneli Kruve.** Matrix effects in liquid-chromatography electrospray mass-spectrometry. Tartu, 2011, 156 p.
106. **Gary Urb.** Assessment of environmental impact of oil shale fly ash from PF and CFB combustion. Tartu, 2011, 108 p.
107. **Nikita Oskolkov.** A novel strategy for peptide-mediated cellular delivery and induction of endosomal escape. Tartu, 2011, 106 p.
108. **Dana Martin.** The QSPR/QSAR approach for the prediction of properties of fullerene derivatives. Tartu, 2011, 98 p.
109. **Säde Viirlaid.** Novel glutathione analogues and their antioxidant activity. Tartu, 2011, 106 p.
110. **Ülis Sõukand.** Simultaneous adsorption of Cd^{2+}, Ni^{2+}, and Pb^{2+} on peat. Tartu, 2011, 124 p.
111. **Lauri Lipping.** The acidity of strong and superstrong Brønsted acids, an outreach for the "limits of growth": a quantum chemical study. Tartu, 2011, 124 p.
112. **Heisi Kurig.** Electrical double-layer capacitors based on ionic liquids as electrolytes. Tartu, 2011, 146 p.
113. **Marje Kasari.** Bisubstrate luminescent probes, optical sensors and affinity adsorbents for measurement of active protein kinases in biological samples. Tartu, 2012, 126 p.
114. **Kalev Takkis.** Virtual screening of chemical databases for bioactive molecules. Tartu, 2012, 122 p.
115. **Ksenija Kisseljova**. Synthesis of aza-β^3-amino acid containing peptides and kinetic study of their phosphorylation by protein kinase A. Tartu, 2012, 104 p.
116. **Riin Rebane.** Advanced method development strategy for derivatization LC/ESI/MS. Tartu, 2012, 184 p.
117. **Vladislav Ivaništšev.** Double layer structure and adsorption kinetics of ions at metal electrodes in room temperature ionic liquids. Tartu, 2012, 128 p.
118. **Irja Helm.** High accuracy gravimetric Winkler method for determination of dissolved oxygen. Tartu, 2012, 139 p.
119. **Karin Kipper.** Fluoroalcohols as Components of LC-ESI-MS Eluents: Usage and Applications. Tartu, 2012, 164 p.
120. **Arno Ratas.** Energy storage and transfer in dosimetric luminescent materials. Tartu, 2012, 163 p.
121. **Reet Reinart-Okugbeni**. Assay systems for characterisation of subtype-selective binding and functional activity of ligands on dopamine receptors. Tartu, 2012, 159 p.

122. **Lauri Sikk.** Computational study of the Sonogashira cross-coupling reaction. Tartu, 2012, 81 p.
123. **Karita Raudkivi.** Neurochemical studies on inter-individual differences in affect-related behaviour of the laboratory rat. Tartu, 2012, 161 p.
124. **Indrek Saar.** Design of GalR2 subtype specific ligands: their role in depression-like behavior and feeding regulation. Tartu, 2013, 126 p.
125. **Ann Laheäär.** Electrochemical characterization of alkali metal salt based non-aqueous electrolytes for supercapacitors. Tartu, 2013, 127 p.
126. **Kerli Tõnurist.** Influence of electrospun separator materials properties on electrochemical performance of electrical double-layer capacitors. Tartu, 2013, 147 p.
127. **Kaija Põhako-Esko.** Novel organic and inorganic ionogels: preparation and characterization. Tartu, 2013, 124 p.
128. **Ivar Kruusenberg.** Electroreduction of oxygen on carbon nanomaterial-based catalysts. Tartu, 2013, 191 p.
129. **Sander Piiskop.** Kinetic effects of ultrasound in aqueous acetonitrile solutions. Tartu, 2013, 95 p.
130. **Ilona Faustova**. Regulatory role of L-type pyruvate kinase N-terminal domain. Tartu, 2013, 109 p.
131. **Kadi Tamm.** Synthesis and characterization of the micro-mesoporous anode materials and testing of the medium temperature solid oxide fuel cell single cells. Tartu, 2013, 138 p.
132. **Iva Bozhidarova Stoyanova-Slavova.** Validation of QSAR/QSPR for regulatory purposes. Tartu, 2013, 109 p.
133. **Vitali Grozovski**. Adsorption of organic molecules at single crystal electrodes studied by *in situ* STM method. Tartu, 2014, 146 p.
134. **Santa Veikšina**. Development of assay systems for characterisation of ligand binding properties to melanocortin 4 receptors. Tartu, 2014, 151 p.
135. **Jüri Liiv.** PVDF (polyvinylidene difluoride) as material for active element of twisting-ball displays. Tartu, 2014, 111 p.
136. **Kersti Vaarmets.** Electrochemical and physical characterization of pristine and activated molybdenum carbide-derived carbon electrodes for the oxygen electroreduction reaction. Tartu, 2014, 131 p.
137. **Lauri Tõntson**. Regulation of G-protein subtypes by receptors, guanine nucleotides and Mn^{2+}. Tartu, 2014, 105 p.
138. **Aiko Adamson.** Properties of amine-boranes and phosphorus analogues in the gas phase. Tartu, 2014, 78 p.
139. **Elo Kibena**. Electrochemical grafting of glassy carbon, gold, highly oriented pyrolytic graphite and chemical vapour deposition-grown graphene electrodes by diazonium reduction method. Tartu, 2014, 184 p.
140. **Teemu Näykki.** Novel Tools for Water Quality Monitoring – From Field to Laboratory. Tartu, 2014, 202 p.
141. **Karl Kaupmees.** Acidity and basicity in non-aqueous media: importance of solvent properties and purity. Tartu, 2014, 128 p.

142. **Oleg Lebedev**. Hydrazine polyanions: different strategies in the synthesis of heterocycles. Tartu, 2015, 118 p.
143. **Geven Piir.** Environmental risk assessment of chemicals using QSAR methods. Tartu, 2015, 123 p.
144. **Olga Mazina.** Development and application of the biosensor assay for measurements of cyclic adenosine monophosphate in studies of G protein-coupled receptor signalinga. Tartu, 2015, 116 p.
145. **Sandip Ashokrao Kadam.** Anion receptors: synthesis and accurate binding measurements. Tartu, 2015, 116 p.
146. **Indrek Tallo.** Synthesis and characterization of new micro-mesoporous carbide derived carbon materials for high energy and power density electrical double layer capacitors. Tartu, 2015, 148 p.
147. **Heiki Erikson.** Electrochemical reduction of oxygen on nanostructured palladium and gold catalysts. Tartu, 2015, 204 p.
148. **Erik Anderson.** *In situ* Scanning Tunnelling Microscopy studies of the interfacial structure between Bi(111) electrode and a room temperature ionic liquid. Tartu, 2015, 118 p.
149. **Girinath G. Pillai.** Computational Modelling of Diverse Chemical, Biochemical and Biomedical Properties. Tartu, 2015, 140 p.
150. **Piret Pikma.** Interfacial structure and adsorption of organic compounds at Cd(0001) and Sb(111) electrodes from ionic liquid and aqueous electrolytes: an *in situ* STM study. Tartu, 2015, 126 p.
151. **Ganesh babu Manoharan.** Combining chemical and genetic approaches for photoluminescence assays of protein kinases. Tartu, 2016, 126 p.
152. **Carolin Siimenson**. Electrochemical characterization of halide ion adsorption from liquid mixtures at Bi(111) and pyrolytic graphite electrode surface. Tartu, 2016, 110 p.
153. **Asko Laaniste.** Comparison and optimisation of novel mass spectrometry ionisation sources. Tartu, 2016, 156 p.
154. **Hanno Evard.** Estimating limit of detection for mass spectrometric analysis methods. Tartu, 2016, 224 p.
155. **Kadri Ligi.** Characterization and application of protein kinase-responsive organic probes with triplet-singlet energy transfer. Tartu, 2016, 122 p.
156. **Margarita Kagan.** Biosensing penicillins' residues in milk flows. Tartu, 2016, 130 p.
157. **Marie Kriisa.** Development of protein kinase-responsive photoluminescent probes and cellular regulators of protein phosphorylation. Tartu, 2016, 106 p.
158. **Mihkel Vestli.** Ultrasonic spray pyrolysis deposited electrolyte layers for intermediate temperature solid oxide fuel cells. Tartu, 2016, 156 p.
159. **Silver Sepp**. Influence of porosity of the carbide-derived carbon on the properties of the composite electrocatalysts and characteristics of polymer electrolyte fuel cells. Tartu, 2016, 137 p.
160. **Kristjan Haav**. Quantitative relative equilibrium constant measurements in supramolecular chemistry. Tartu, 2017, 158 p.

161. **Anu Teearu**. Development of MALDI-FT-ICR-MS methodology for the analysis of resinous materials. Tartu, 2017, 205 p.
162. **Taavi Ivan**. Bifunctional inhibitors and photoluminescent probes for studies on protein complexes. Tartu, 2017, 140 p.
163. **Maarja-Liisa Oldekop**. Characterization of amino acid derivatization reagents for LC-MS analysis. Tartu, 2017, 147 p.
164. **Kristel Jukk**. Electrochemical reduction of oxygen on platinum- and palladium-based nanocatalysts. Tartu, 2017, 250 p.
165. **Siim Kukk**. Kinetic aspects of interaction between dopamine transporter and *N*-substituted nortropane derivatives. Tartu, 2017, 107 p.
166. **Birgit Viira**. Design and modelling in early drug development in targeting HIV-1 reverse transcriptase and Malaria. Tartu, 2017, 172 p.
167. **Rait Kivi**. Allostery in cAMP dependent protein kinase catalytic subunit. Tartu, 2017, 115 p.
168. **Agnes Heering**. Experimental realization and applications of the unified acidity scale. Tartu, 2017, 123 p.
169. **Delia Juronen**. Biosensing system for the rapid multiplex detection of mastitis-causing pathogens in milk. Tartu, 2018, 85 p.
170. **Hedi Rahnel.** ARC-inhibitors: from reliable biochemical assays to regulators of physiology of cells. Tartu, 2018, 176 p.
171. **Anton Ruzanov.** Computational investigation of the electrical double layer at metal–aqueous solution and metal–ionic liquid interfaces. Tartu, 2018, 129 p.
172. **Katrin Kestav.** Crystal Structure-Guided Development of Bisubstrate-Analogue Inhibitors of Mitotic Protein Kinase Haspin. Tartu, 2018, 166 p.
173. **Mihkel Ilisson.** Synthesis of novel heterocyclic hydrazine derivatives and their conjugates. Tartu, 2018, 101 p.
174. **Anni Allikalt.** Development of assay systems for studying ligand binding to dopamine receptors. Tartu, 2018, 160 p.
175. **Ove Oll.** Electrical double layer structure and energy storage characteristics of ionic liquid based capacitors. Tartu, 2018, 187 p.
176. **Rasmus Palm.** Carbon materials for energy storage applications. Tartu, 2018, 114 p.
177. **Jörgen Metsik.** Preparation and stability of poly(3,4-ethylenedioxythiophene) thin films for transparent electrode applications. Tartu, 2018, 111 p.
178. **Sofja Tšepelevitš.** Experimental studies and modeling of solute-solvent interactions. Tartu, 2018, 109 p.
179. **Märt Lõkov.** Basicity of some nitrogen, phosphorus and carbon bases in acetonitrile. Tartu, 2018, 104 p.
180. **Anton Mastitski**. Preparation of α-aza-amino acid precursors and related compounds by novel methods of reductive one-pot alkylation and direct alkylation. Tartu, 2018, 155 p.
181. **Jürgen Vahter**. Development of bisubstrate inhibitors for protein kinase CK2. Tartu, 2019, 186 p.

182. **Piia Liigand.** Expanding and improving methodology and applications of ionization efficiency measurements. Tartu, 2019, 189 p.
183. **Sigrid Selberg.** Synthesis and properties of lipophilic phosphazene-based indicator molecules. Tartu, 2019, 74 p.
184. **Jaanus Liigand.** Standard substance free quantification for LC/ESI/MS analysis based on the predicted ionization efficiencies. Tartu, 2019, 254 p.
185. **Marek Mooste.** Surface and electrochemical characterisation of aryl film and nanocomposite material modified carbon and metal-based electrodes. Tartu, 2019, 304 p.
186. **Mare Oja.** Experimental investigation and modelling of pH profiles for effective membrane permeability of drug substances. Tartu, 2019, 306 p.
187. **Sajid Hussain.** Electrochemical reduction of oxygen on supported Pt catalysts. Tartu, 2019, 220 p.
188. **Ronald Väli.** Glucose-derived hard carbon electrode materials for sodium-ion batteries. Tartu, 2019, 180 p.
189. **Ester Tee.** Analysis and development of selective synthesis methods of hierarchical micro- and mesoporous carbons. Tartu, 2019, 210 p.
190. **Martin Maide.** Influence of the microstructure and chemical composition of the fuel electrode on the electrochemical performance of reversible solid oxide fuel cell. Tartu, 2020, 144 p.
191. **Edith Viirlaid.** Biosensing Pesticides in Water Samples. Tartu, 2020, 102 p.
192. **Maike Käärik.** Nanoporous carbon: the controlled nanostructure, and structure-property relationships. Tartu, 2020, 162 p.
193. **Artur Gornischeff.** Study of ionization efficiencies for derivatized compounds in LC/ESI/MS and their application for targeted analysis. Tartu, 2020, 124 p.
194. **Reet Link.** Ligand binding, allosteric modulation and constitutive activity of melanocortin-4 receptors. Tartu, 2020, 108 p.
195. **Pilleriin Peets.** Development of instrumental methods for the analysis of textile fibres and dyes. Tartu, 2020, 150 p.
196. **Larisa Ivanova.** Design of active compounds against neurodegenerative diseases. Tartu, 2020, 152 p.
197. **Meelis Härmas.** Impact of activated carbon microstructure and porosity on electrochemical performance of electrical double-layer capacitors. Tartu, 2020, 122 p.
198. **Ruta Hecht.** Novel Eluent Additives for LC-MS Based Bioanalytical Methods. Tartu, 2020, 202 p.
199. **Max Hecht.** Advances in the Development of a Point-of-Care Mass Spectrometer Test. Tartu, 2020, 168 p.
200. **Ida Rahu.** Bromine formation in inorganic bromide/nitrate mixtures and its application for oxidative aromatic bromination. Tartu, 2020, 116 p.
201. **Sander Ratso**. Electrocatalysis of oxygen reduction on non-precious metal catalysts. Tartu, 2020, 371 p.
202. **Astrid Darnell.** Computational design of anion receptors and evaluation of host-guest binding. Tartu, 2021, 150 p.

203. **Ove Korjus.** The development of ceramic fuel electrode for solid oxide cells. Tartu, 2021, 150 p.
204. **Merit Oss.** Ionization efficiency in electrospray ionization source and its relations to compounds' physico-chemical properties. Tartu, 2021, 124 p.
205. **Madis Lüsi**. Electroreduction of oxygen on nanostructured palladium catalysts. Tartu, 2021, 180 p.
206. **Eliise Tammekivi.** Derivatization and quantitative gas-chromatographic analysis of oils. Tartu, 2021, 122 p.
207. **Simona Selberg.** Development of Small-Molecule Regulators of Epi-transcriptomic Processes. Tartu, 2021, 122 p.
208. **Olivier Etebe Nonga.** Inhibitors and photoluminescent probes for in vitro studies on protein kinases PKA and PIM. Tartu, 2021, 189 p.
209. **Riinu Härmas.** The structure and H2 diffusion in porous carbide-derived carbon particles. Tartu, 2022, 123 p.
210. **Maarja Paalo.** Synthesis and characterization of novel carbon electrodes for high power density electrochemical capacitors. Tartu, 2022, 144 p.
211. **Jinfeng Zhao.** Electrochemical characteristics of Bi(hkl) and micro-meso-porous carbon electrodes in ionic liquid based electrolytes. Tartu, 2022, 134 p.
212. **Alar Heinsaar.** Investigation of oxygen electrode materials for high-temperature solid oxide cells in natural conditions. Tartu, 2022, 120 p.
213. **Jaana Lilloja.** Transition metal and nitrogen doped nanocarbon cathode catalysts for anion exchange membrane fuel cells. Tartu, 2022, 202 p.
214. **Maris-Johanna Tahk.** Novel fluorescence-based methods for illuminating transmembrane signal transduction by G-protein coupled receptors. Tartu, 2022, 200 p.
215. **Eerik Jõgi.** Development and Applications of E. coli Immunosensor. Tartu, 2022, 103 p.
216. **Alo Rüütel.** Design principles of synthetic molecular receptors for anion-selective electrodes. Tartu, 2022, 109 p.
217. **Tanel Sõrmus.** Development of stimuli-responsive and covalent bisubstrate inhibitors of protein kinases. Tartu, 2022, 148 p.
218. **Oleg Artemchuk.** Autotrophic nitrogen removal processes for nutrient removal from sidestream and mainstream wastewater. Tartu, 2022, 115 p.
219. **Andre Leesment.** Quantitative studies of Brønsted acidity in biphasic systems and gas-phase. Tartu, 2023, 83 p.
220. **Meeli Arujõe-Sado.** Structural effects in aza-peptide bond formation reaction. Tartu, 2023, 83 p.
221. **Jonas Mart Linge.** Electrochemical reduction of oxygen on silver-based catalysts. Tartu, 2023, 269 p.
222. **Tõnis Laasfeld.** Integrating Image Analysis and Quantitative Modeling for a Holistic View of GPCR Ligand Binding Dynamics. Tartu, 2023, 226 p.
223. **Ernesto de Jesus Zapata Flores.** Derivatization Reagents used in negative mode electrospray LC-MS. Tartu, 2023, 107 p.

224. **Patrick Teppor.** Obtaining platinum-free oxygen reduction catalysts through biomass valorization: a case study of peat. Tartu, 2023, 161 p.
225. **Peeter Valk.** Methanol Oxidation on Platinum-Rare-Earth Metal Oxide Activated Catalysts. Tartu, 2023, 162 p.
226. **Shidong Chen.** Unravelling prehistoric plant exploitation in eastern Baltic: organic residue analysis of plant-based materials by multi-method approach. Tartu, 2023, 245 p.
227. **Yogesh Kumar.** M-N_4 macrocycle-based catalysts for electrocatalysis of oxygen reduction and oxygen evolution. Tartu, 2023, 224 p.
228. **Kerli Martin.** Recognition of carboxylates by synthetic receptors – from structure-affinity studies to solid-contact anion-selective electrode prototyping. Tartu, 2024, 130 p.
229. **Huy Quí Vinh Nguyen.** Development of Carbon Supported Pt–CeO_2 Catalysts for Proton Exchange Membrane Fuel Cells. Tartu, 2024, 198 p.
230. **Heigo Ers**. Adsorption and Structuring Processes at Single Crystal Electrode – Ionic Liquid Interface – Insights from Simulations and *in situ* Studies. Tartu, 2024, 137 p.
231. **Ritums Cepitis.** Modelling Structural and Geometrical Effects in Carbon Dioxide and Oxygen Electrocatalysis. Tartu, 2024, 99 p.
232. **Kaarel Kisand.** Resorcinol-derived carbon-based catalysts for polymer electrolyte fuel cell cathodes. Tartu, 2024, 205 p.
233. **Akmal Kosimov**. Template-assisted Mechanosynthesis (TAMS) for the production of bifunctional transition metal-based catalysts. Tartu, 2024, 123 p.
234. **Larissa Silva Macieli.** Derivatization-targeted LC-MS analysis of compounds containing amino group. Tartu, 2024, 157 p.
235. **Silvester Jürjo.** Separation of rare earth elements from Estonian phosphorite ore using liquid extraction followed by electrochemical reduction. Tartu, 2024, 99 p.
236. **Jan-Michael C. Cayme.** Organic-inorganic interactions in experimental and archaeological ceramics. Tartu, 2025, 156 p.